PONTIFICIA UNIVERSIDAD CATÓLICA DE CHILE
ESCUELA DE INGENIERÍA

DEVELOPMENT OF TECHNOLOGIES AND TECHNIQUES FOR WIDE-FIELD ASTRONOMICAL OBSERVATIONS

EDUARDO HUMBERTO GARCÉS SANTIBAÑEZ

Thesis submitted to the Office of Research and Graduate Studies
in partial fulfillment of the requirements for the degree of
Master of Science in Engineering

Advisors:
CHRISTIAN D. GUZMÁN

Santiago de Chile, March, 2018

PONTIFICIA UNIVERSIDAD CATÓLICA DE CHILE
ESCUELA DE INGENIERÍA

DEVELOPMENT OF TECHNOLOGIES AND TECHNIQUES FOR WIDE-FIELD ASTRONOMICAL OBSERVATIONS

EDUARDO HUMBERTO GARCÉS SANTIBAÑEZ

Members of the Committee:
CHRISTIAN D. GUZMÁN
FELIPE NUÑEZ
JAIME ANGUITA
ALFONSO CRUZ

Thesis submitted to the Office of Research and Graduate Studies
in partial fulfillment of the requirements for the degree of
Master of Science in Engineering

Santiago de Chile, March, 2018

A mis padres. Es sobre sus hombros que puedo mirar hacia las estrellas.

ACKNOWLEDGEMENTS

If I have come to write these words its only because the rush has come to an end (I know... finally!). And it is here, in this small place, where I cannot be grateful enough for those who have supported me during this period.

First, I would like to thank my advisor, Dani. Many years have passed since I started to work within your research group as an undergraduate student, where I had a chance to follow the barely taken path of the “Astro-engineer”. The only rules you had for us were to never be afraid of making mistakes, to consider all the available resources as our own and to always work in what we liked the most. This entire work is a result of these premises. Thank you for the encouragement, for the academic guidance and for the mentoring.

To my former research companions: Amokrane, Nicolás, Nicole and Norman. Many of the things I learned and much of the experience I gained were a result of the numerous times I was around you. Even with all the work you had ahead, you took the time to guide me through what you were doing until I was able to explain it or do it by myself.

Special thanks to my closest friends Constanza, Gonzalo, Rodrigo and Javier. Your listening, support, advice and encouragement were certainly essential these years. Your friendship is a unique gift, worth more than anything I can write here.

Finally, I would like to show my deepest and most profound gratitude to my family. For these next words I have taken the liberty of switching to my mother-tongue: Durante todos estos años ha sido a través de su incansable apoyo, infinita paciencia y amor incondicional que he llegado a ser la persona que soy, y ha sido a través de ustedes que he encontrado la fuerza y el coraje de trazar mi propio destino. A través de este camino de victorias y derrotas, han sido ustedes quienes han hecho que todo haya sido llevadero. Por esto y mucho más, infinitas gracias.

TABLE OF CONTENTS

LIST OF FIGURES

LIST OF TABLES

ABSTRACT

Observational astronomy requires instruments capable of delivering wide-field of view and high resolution, ideally in the same observation. This work contributes in both directions. First, for the BOMBOLO instrument (Guzmán et al., 2014), which was conceived and proposed in 2014 as a visitor instrument for 4-meter SOAR telescope, as a wide-field multi-channel imager, capable of observations in three different bands of the spectrum simultaneously and independently. As part of its development, a mechanical structure is proposed here in detail as well as a finite element analysis to evaluate its performance. The performance evaluation took the worst operation conditions that the instrument would experience (Garcés et al., 2016) in terms of gravity vector orientation. With certain considerations, the designed structure is suitable to minimize the loss of quality due to the variable orientation of the instrument and the consequent mechanical deformation. Second, when Extremely Large Telescopes use Adaptive Optics systems based on Shack-Hartmann wave-front sensors (WFS) observing Laser Guide Stars, the spots observed in the WFS image plane appear elongated. A new technique based on Artificial Neural Networks (Mello et al., 2014) was evaluated in the laboratory to compute the centroid of these elongated spots. Two experiments were built with different emulation capabilities, with one of them devised to produce ANN training data. Two ANNs were trained, each with different architecture. Pearson product-moment correlation coefficients were used to measure their performance and relevant conclusions were obtained for future work in this area.

Keywords: Astronomical Instrumentation, Adaptive Optics, Wide field of view, Imager, Multi-band, Fast Photometry, Artificial Neural Networks, Shack-Hartmann, Elongated Spots, Laser Guide Star.

RESUMEN

Las observaciones astronómicas requieren instrumentos con capacidad de observar un campo amplio con alta resolución, idealmente de forma simultánea. Este trabajo contribuye en ambos sentidos. Primero, para el instrumento BOMBOLO (Guzmán et al., 2014), concebido y propuesto como instrumento visitante para el telescopio SOAR de 4 metros, como *imager* de campo amplio de múltiples canales, capaz de observar en tres bandas del espectro de forma simultánea e independiente. Como parte de su desarrollo, una estructura mecánica es requerida, la cual se presenta aquí en detalle junto a un análisis de elementos finitos para evaluar su desempeño. La evaluación de desempeño considera las peores condiciones de operación que el instrumento podría experimentar (Garcés et al., 2016) en términos de la orientación del vector de gravedad. Con ciertas consideraciones, el diseño de la estructura es capaz de minimizar la pérdida en calidad de imagen que produce la deformación de la estructura como consecuencia de la orientación variable del instrumento. Segundo, una técnica basada en Redes Neuronales Artificiales (ANN) fue evaluada en laboratorio, para calcular el centroide en *spots* elongados en sensores de frente de onda Shack-Hartmann (Mello et al., 2014), para el caso de Óptica Adaptativa en instrumentos de amplio campo de vista para Telescopios Extremadamente Grandes. Dos experimentos fueron elaborados con diferentes capacidades de emulación, con uno de ellos ideado para producir datos de entrenamiento para la ANN. Dos ANN fueron entrenadas, con diferentes arquitecturas. Coefficientes de correlación de Pearson fueron calculados para medir el desempeño, y conclusiones relevantes fueron obtenidas para el trabajo futuro en esta área.

Palabras Claves: Instrumentación Astronómica, Óptica Adaptativa, Campo Amplio, Imager, Multi-banda, Fotometría de alta velocidad, Redes Neuronales Artificiales, Shack-Hartmann, Estrellas Elongadas, Estrellas Guía Láser.

1. INTRODUCTION

In the last decades, astronomy has become a science that has required more complex, sophisticated and versatile technologies and techniques. These key aspects aspire to complete tasks, each time more complex and more precise, with the main requirement of providing resources for scientific progress.

The main mechanism used in astronomy to gather the necessary information is the collection of electromagnetic radiation emitted by the source of study. These measurements are achieved through the use of different technologies, such as telescopes and sophisticated instruments. Through the analysis of the object's gathered light one can learn its main chemical components, its distance from Earth, its relative velocity, its shape, as well as numerous other crucial measurements.

Ground-based and space telescopes observe different fields of view in different parts of the spectrum. A fair amount of these observations contain light composed of multiple wavelengths ranging from near-UV to infrared. Due to its size, elongation and shape, observing in a wide field of view is also required. In fact, this is the case with galaxies, clusters, constellations, and other celestial entities. The two contributions presented in this document attempt to make improvements in respect to these kinds of observations.

The first contribution presented is part of the design process of BOMBOLO, an instrument that is able to perform high speed photometry –simultaneously in multiple bands of the spectrum ranging from near-ultraviolet (near-UV) to near-infrared (near-IR). The instrument emerges as an important tool for the observation of a series of vaguely studied scientific cases due to its time-scale nature ranging from tens of seconds to minutes.

The second contribution is an extension of a previous work regarding the use of Artificial Neural Networks in Adaptive Optics (AO) –implemented in the centroid calculation of elongated spots formed by Laser Guide Stars in Shack-Hartmann Wave-front Sensors. These centroid positions can later be used for the wave-front sensor reconstruction and correction by utilizing an AO control loop.

1.1. Astronomical Instrumentation

To observe and study all the phenomena and events occurring in space, there is a vast diversity of technologies able to acquire and measure the information inside the received light. Each one of these technologies is designed to complete specific tasks, such as forming images of the objects, measuring the flux of photons from a source, unraveling the spectrum of wavelengths or acquiring the shape of distant planetary systems. These are a few of the main objectives that define the principal characteristics of the telescopes and instruments used, as well as how they operate and the information they seek to retrieve. Some of these instruments are described in the following list:

Imagers: The purpose of an Imager, as its name might suggest, is to form an image of the objects observed. Placing a detector in the focal plane of the telescope would be enough to achieve this. However, in order to obtain a different field of view, factor of angular magnification, or other characteristics, an optical system is used. Optical systems change how the light propagates, usually refocusing the image of the preview focal plane in a new one that possesses the desired characteristics. Other optical elements can be added to the optical train. For example, density filters and dichroics are utilized to provide an image with a different intensity and wavelengths composition.

Spectrographs: Slightly different from imagers, spectrographs do not intend to retrieve an image of the object itself, but rather its wavelength spectrum. By using a dispersive element, spectrographs are able to unravel the wavelength composition of the light received, in turn, retrieving the object's spectrum instead of an image of said object. By analyzing the spectrum, characteristics such as the object's chemical composition and radial velocity, among others, can be measured.

Other Instruments: There are other types of instruments, such as Interferometers, Photometers, Coronagraphs, AO modules, and more. These instruments represent a significant part of what is currently available within the astronomical community, but what they do is beyond the scope of this work. The only exception deals with the AO modules, which are covered in Section 1.2.2.

1.1.1. BOMBOLO: A 3-arm imager for SOAR Observatory

BOMBOLO (Guzmán et al., 2014) is an instrument conceived to perform fast and simultaneous multi-passband photometry and is intended to be installed as a visitor instrument at the SOAR observatory, located in Cerro Pachón, La Serena, Chile. The instrument concept arose as an answer to a series of scientific cases (Bruch, 1992; Phelan et al., 2007; Parsons et al., 2010) that cannot be studied in depth due to their time-scale nature and the current instruments available, specifically within the Chilean community of astronomers.

Currently, throughout the world there are a few instruments capable of observing fast events simultaneously in different bands of the spectrum within the near-UV to near-IR wavelengths (Dhillon et al., 2007), but they are not available in Chile or have very different characteristics. In this sense, BOMBOLO emerges as a unique solution for an unresolved necessity within the astronomical Chilean community as well as a way to strengthen the emerging capabilities of instrument design and development in Chile.

1.1.2. BOMBOLO's Scientific Cases

The instrument is envisioned as a tool to explore a wide range of space events occuring within the time scale of seconds to minutes (Angeloni et al., 2014). A few of the mentioned cases are:

- Gravitational Microlensing Events
- Exoplanetary Transits
- Accretion Processes at all Spatial Scales
- Stellar Population Diagnostics
- Solar System Objects Nature and Formation

These scientific cases share a few characteristics, some of them more obvious than others given the general idea of the instrument, such as a wide field of view, and others not necessarily given by the nature of the event but by how it is measured. For example, Accretion Processes occur at all scales, with spacial and temporal components. To study these events, a near star with a certain brightness as a flux reference is required in order to analyze the rate at which the Accretion Process evolves. Figure 1.1 shows the probability of finding a star with the required characteristics for certain fields of view. It can be observed that a higher field of view increases the success rate of observing these events with a good performance. Other events, such as gravitational microlensing, occur in very small windows of time. In turn, the observable period is limited, forcing the type of observations and information gathered to be limited as well. The capability of observing in simultaneous bands is useful in order to obtain a gross approximation of the chemical composition of the star's surface or the atmosphere of an orbiting planet, while acquiring images of the transit.

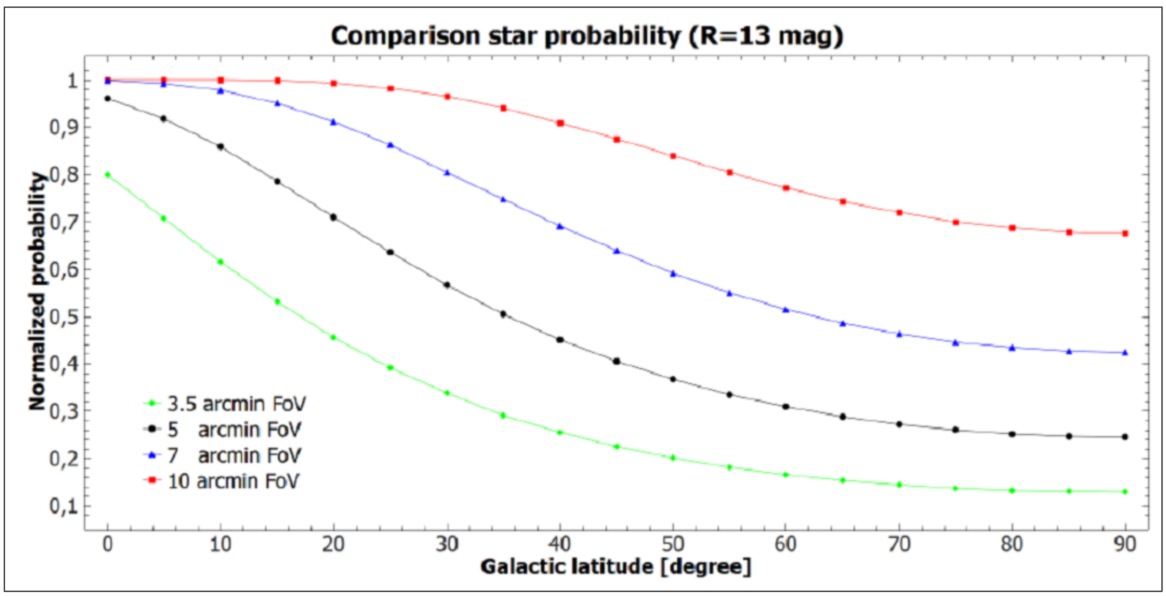

Figure 1.1. Probability of finding a R=13 mag comparison star in the instrumental Field of View (FoV), as a function of galactic latitude and increasing FoVs, up to 10 arcminutes. A 7 x 7 arcmin^2 FoV is the best compromise between an optimal pixel scale and a relatively large FoV. Image taken from (Guzmán, 2014).

1.1.3. BOMBOLO's General Concept

The scientific cases mentioned require, in general, a wide field of view and a broad range of wavelengths for the observation. Because of the time-scales, it is desirable to

Table 1.1. BOMBOLO Instrument Requirements

Requeriment	**Value**
Field of View	7×7 arcmin^2
Pixel Scale	0.3 arcsec/pix
Wavelength Coverage	320 – 900 nm
Dichroic Cutoff	390–400 nm and 550–560 nm
Readout Time	$\geq$10 seconds
Readout Noise	$\geq$5 electrons
Exposure	In-sync and independent

minimize the light loss as well as obtain the highest possible signal to noise ratio. After the iteration of these characteristics and a technical feasibility study, the next course of action involves the engineering requirements for the instrument, as listed in Table 1.1.

Initially conceived as a visitor instrument for the SOAR Observatory, BOMBOLO will be placed at the bent-cassegrain port of the 4-meter telescope. Light gathered by the telescope will be fed to the instrument at this port and then separated into three channels by dichroic filters, as shown in Figure 1.2. Dichroic filters can separate light by wavelength bands. For a certain "cutoff" wavelength, light with wavelengths under that value will be reflected and over that cutoff will be transmitted. As described in Table 1.1, the first dichroic has a cutoff wavelength within 390 and 400 nm, whereas the second one has it between 550 and 600 nm. The separated beams are sent into the three channels [1], forming the same image but each one with different wavelength content. These images will be acquired by three detectors able to work simultaneously and independently, which is ensured through the coordination and control of all the modules within the instrument by a common control system.

[1] Just as an internal convention, these three channels have been defined as blue channel/arm, green channel/arm and red channel/arm, depending on its wavelength composition (even though these names do not correlate directly with the real color wavelengths).

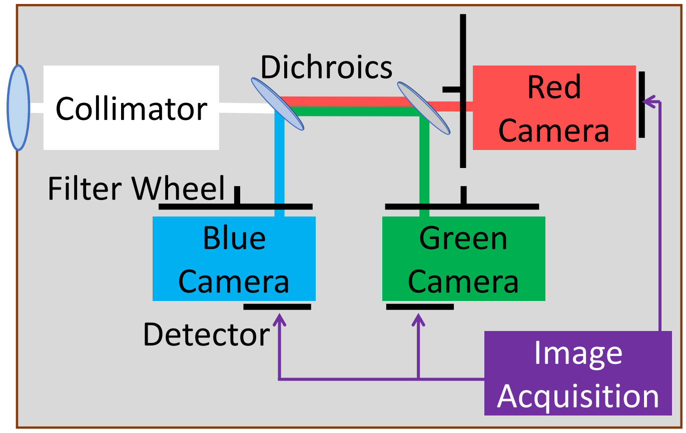

Figure 1.2. BOMBOLO General Concept. Light gathered by the telescope is sent into the instrument. The beam is collimated and then separated by two dichroics, sending 3 different beams containing different wavelength bands. Then, for each beam, a band filter is applied to narrow the passband if required, and then focused on a detector.

Each one of BOMBOLO's technical specifications satisfies a consensus between the scientific requirements, the vision of its general concept, and a cost-efficiency goal according to the available budget for its total development. Some of these technical specifications are explained below:

Field of View (FoV): As shown in Figure 1.1, a wide field of view increases the probability of finding a reference star, as well as the amount of objects that can be observed by the detector. A 10×10 arcmin^2 FoV would be the best choice, but such large FoV require an excessively large collimator system, which is very expensive. This would considerably reduce the available budget for other areas. Also, focusing such a big FoV on a single detector would make the *Point Spread Function* (PSF) smaller on the focal plane, and thus put a risk upon attaining good sampling (this will be covered with more depth in Section 2.2). 7×7 arcmin^2 has been chosen as a point of balance between the scientific and technical requirements as well as with the considered budget.

Pixel Scale: A good sampling of the PSF is highly required because it defines the limit of resolution of the instrument. In this case, the instrument resolution is limited by the atmospheric turbulence, which leads to a "seeing limited" outcome. After a site testing analysis, explained with more details in Section 2.2, the average seeing limited PSF has a relative size of $\sim$0.6 arcsec for the best atmospheric conditions, measured at 700nm. The pixel scale is set at 0.3 arcsec/pix, matching with the sampling required.

Wavelength Coverage: The study of fast photometry events requires simultaneous observations in multiple bands. To fulfill this requirement, BOMBOLO has three arms able to observe in wide bands, followed by filter wheels able to narrow them if necessary.

Given BOMBOLO's capability of observation in three different bands, a rough wavelength composition of a complete area in three bands of the spectrum can be obtained simultaneously. This characteristic situates BOMBOLO as a very low spectral resolution spectrograph, with the advantage of not losing the imaging capabilities as regular spectrographs tend to do.

1.2. Atmospheric Turbulence in Astronomical Observations

For a long time, scintillation has been considered as an effect produced by the stars and planets themselves. However, this explanation is actually inaccurate due to the atmosphere's role in producing this phenomenon. Fluctuations in the air's temperature at different air layers derive in fluctuations in the air's refractive index. Wind shears mix these layers, in turn, producing spacial and temporal temperature inhomogeneities (Roddier, 1999, p.9-13). The difference in temperatures between layers is tiny, but added up through the atmosphere generates optical path differences between parallel rays that are far from negligible. The wave-front that was plane before entering to earth's atmosphere is distorted after traversing the atmosphere. The statistical behavior of the refractive index inhomogeneities, derived from temperature inhomogeneities, is governed by Kolmogorov-Obukhov laws of turbulence.

Since the appeal behind knowing the phase distortion of a wave-front is local and not absolute, it is not required to know the absolute value of refractive index, but rather the difference between its value and a nearby point.

Following the theoretical work presented in (Roddier, 1999, p.9-13), consider a point $\vec{r}$ and a point nearby at distance $\rho = |\vec{\rho}|$, where $\vec{r}$ and $\vec{\rho}$ represent a position in a three-dimensional space. The variance between the two refractive indexes can be defined by equation 1.1, where the brackets $\langle\rangle$ represent an ensemble average.

$$D_N(\rho) = \langle |n(\vec{r}) - n(\vec{r} + \vec{\rho})|^2 \rangle = C_N^2 \rho^{2/3} \tag{1.1}$$

$D_N(\rho)$ is called the refractive index structure function, which, as a first order approximation, depends only on $|\rho|$ independently of its direction, thus making this process isotropic (as long as ρ is within the inertial range, where the kinetic energy is not dissipated as heat but as a transfer of "scales", and where the turbulence of higher scales breaks into turbulence of lower scales). The quantity C_N^2 is the index structure coefficient, which is a measure of the local amount of inhomogeneities, and the integral of this quantity along the light propagation path gives a measure of the total amount of wave-front degradation.

The deformation of the wave-front surface is related to the phase fluctuation given by

$$\varphi = k \int n(z)dz \tag{1.2}$$

where k is the wave number $k = 2\pi/\lambda$. By considering again that there is no interest in knowing the absolute wave-front phase but, rather, the difference in phase between two points on the telescope aperture, $\varphi(\vec{x})$ and $\varphi(\vec{x}+\vec{\xi})$, with $\xi = |\vec{\xi}|$, the structure function of the phase is given by Equation 1.3, with the consideration that $\vec{x}$ and $\vec{\xi}$ are two-dimensional vectors.

$$D_\varphi(\xi) = \langle |\varphi(\vec{x}) - \varphi(\vec{x} + \vec{\xi})|^2 \rangle \tag{1.3}$$

It is of utmost importance to note that the difference in the optical path is considered achromatic as a good approximation, and only the phase of the wave-front is chromatic given Equation 1.2. Because it is proportionally inverse with the wavelength, the phase compensation is less difficult for infrared wavelengths and more severe for the visible ones.

Working Equation 1.2 into Equation 1.3, and then Equation 1.1 to perform the integration, Equation 1.4 can be obtained.

$$D_\varphi(\xi) = 2.91k^2\xi^{5/3}\int C_N^2(z)dz \tag{1.4}$$

By considering that the integration can be done in terms of altitude instead of line of sight, and that C_N^2 only depends on the height above ground, it can be rewritten as

$$D_\varphi(\xi) = 2.91k^2\xi^{5/3}\cos(\gamma)^{-1}\int C_N^2(h)dh \tag{1.5}$$

where γ is the angular distance between zenith and the axis of the line of sight, and $\cos(\gamma)^{-1}$ is referred as *air mass*. Historically, this Equation has been displayed in a more compressed form, as in Equations 1.6 and 1.7.

$$D_\varphi(\xi) = 6.88\left(\frac{\xi}{r_0}\right)^{5/3} \tag{1.6}$$

$$r_0 = \left[0.423k^2\cos(\gamma)^{-1}\int C_N^2(h)dh\right]^{-3/5} \tag{1.7}$$

Parameter r_0 is referred to as "Fried's Parameter" and it characterizes the effect of the atmospheric turbulence. Considering k, r_0 depends on the wavelength, increasing at a $6/5$ power of it.

Many Equations and quantities can be derived from the Equations presented above, one of them being the "Square wave-front phase distortion" over any aperture. For a circular aperture of diameter d, according to (Fried, 1965; Noll, 1976), the square wave-front phase distortion averaged over the area is given by Equation 1.8,

$$\sigma_1^2 = 1.03\left(\frac{d}{r_0}\right)^2 \tag{1.8}$$

which shows, that because of its construction, the root mean square of the phase distortion over a circular area of diameter r_0 is almost 1 radian.

The corrugations induced in the wave-front decrease the image quality once it is formed by the telescope, thus limiting the resolution capability it possesses. In this sense, the most powerful technique to overcome the negative effects of the atmospheric turbulence in real time is the use of Adaptive Optics.

1.2.1. Classical Adaptive Optics

When observed from Earth, most of the stellar objects can be considered as punctual light sources. Due to the great distance between Earth and the object, the emitted light travels with a spherical shape. As light travels further from the source, the curvature of this sphere decreases with distance. Therefore, when the wave-front finally reaches Earth its shape is almost perfectly flat. This wave-front has, in most cases, no distortions considering that traveled only through space. Nonetheless, as soon as it reaches Earth and traverses through the atmosphere, the wave-front is distorted.

In the classic AO case observed in Figure 1.3, light gathered by the telescope is sent into the AO module, interacting first with a *deformable mirror* (DM). DMs are relatively small devices made of a thin aluminum sheet placed over a matrix of actuators. The shape of the sheet changes as the actuators are pushed or pulled under it. The mentioned wave-front keeps traveling until it is split into two beams, usually by a dichroic or a beam splitter. One of these beams is sent into the scientific camera or scientific instrument, while the other is sent into a device called *"Wave-front Sensor"* (WFS). The WFS is able to characterize the phase aberrations of the wave-front, and retrieve an approximation of its shape (details of this mechanism are explained in 1.2.2). Then, this information is reduced by a Real Time Computer (RTC) that commands the shape that the DM must reproduce in order to cancel out the phase differences in the wave-front. Once the DM starts to compensate the deformation continuously, the WFS characterizes the residual error between the DM and the wave-front and uses this information to keep the loop closed.

The most relevant components on the AO loop are the DM, the WFS and the RTC. Considering that the objective of this work is the characterization and not reconstruction of a wave-front, the attention will be placed on the WFS.

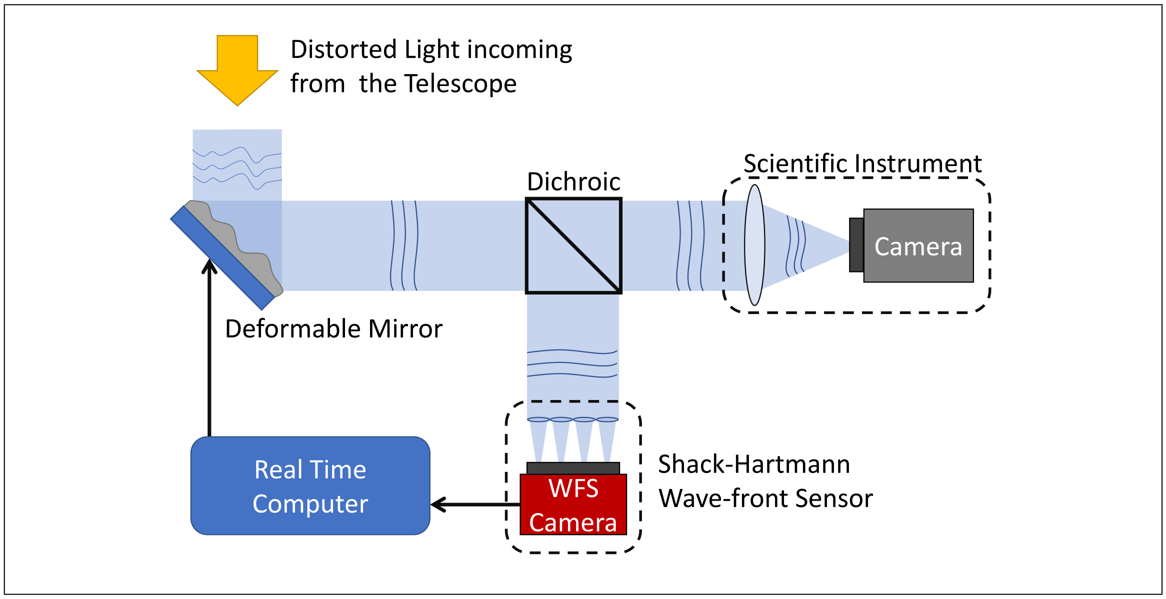

Figure 1.3. Basic diagram of an Adaptive Optics closed loop. Incoming light from the telescope, distorted by the atmosphere, is reshaped by a deformable mirror that receives information continuously from a Real Time Computer (RTC). This RTC computes the residual error between the shape of the deformable mirror and the wave-front itself. This error is characterized by a wave-front sensor (in this case, a Shack-Hartmann wave-front sensor).

1.2.2. Shack-Hartmann Wave-front Sensors

One of the most common and widely used WFS is the Shack-Hartmann. To understand how it retrieves the phase distortions, a few definitions need to be made.

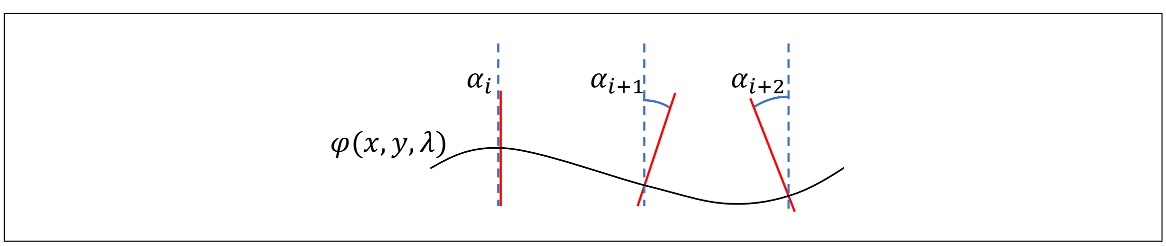

Figure 1.4. Wave-front diagram showing the angle of arrival α for multiple points.

Consider a cross section of a distorted wave-front $\varphi(x, y, \lambda)$ arbitrarily in the x direction, as shown in Figure 1.4. The slope of the wave-front can be defined as

$$-\frac{\partial \varphi}{\partial x}(x, y, \lambda) = \tan\left(\alpha(x, y, \lambda)\right) \tag{1.9}$$

where the minus sign is just for convention. Considering the small angle approximation for the $\tan$ function, Equation 1.9 can be rewritten as

$$-\frac{\partial \varphi}{\partial x}(x, y, \lambda) = \alpha\left(x, y, \lambda\right) \tag{1.10}$$

This Equation relates the wave-front slope with the angle α, which is also called the "angle of arrival".

A Shack-Hartmann (SH) Wave-front sensor consists of a *lenslet array* [2] placed on a conjugated plane of the system's pupil. Each lenslet forms an image of the observed star (called spot), but only with the portion of wave-front that traverses through it.

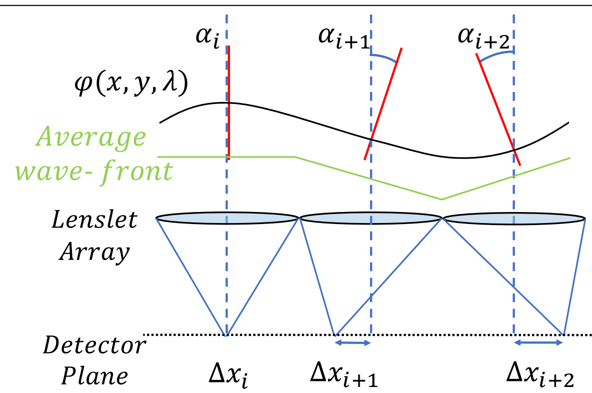

Figure 1.5. Shack-Hartmann wave-front sensor diagram.

The spot formed by each lenslet has a displacement Δx_i on the focal plane proportional to the angle of arrival of the observed portion of wave-front. Because the angle of arrival

[2] A lenslet is literally a small lens. A lenslet array is a set of lenslets placed in some array in the same plane, usually with the same focal length.

is generally small, the displacement can be written as

$$\Delta x_i = \tan(\alpha_i) f \approx \alpha_i f \tag{1.11}$$

where f is the focal distance of the lenslet array.

Each lenslet receives a portion of wave-front, and through it the associated angles of arrival in the x and y directions can be calculated using Equation 1.11. If the lenslet array is able to cover the entire pupil and each lenslet has the correct size to observe a portion of wave-front that is almost flat, it is said that the lenslet array "samples" the wave-front.

According to Equation 1.10 the angle of arrival is the gradient of the wave-front slope. Therefore, through an integration process (or other methods), a similar shape of the wave-front can be "reconstructed"[3]. The reconstructed wave-front is all that is needed for the DM to compensate wave-front distortion, resulting in an increase of the image quality.

1.2.3. Wide Field AO and Laser Guide Stars

The scientific object cannot always be used simultaneously by the SH-WFS to measure the wave-front, in large part due to a lack of required characteristics to do it. Therefore, a reference star near the scientific object is used. The improvement of the image quality after the AO module is conditioned by the distance between the scientific object and the WFS reference star. Even though the long-exposure Point Spread Function (PSF) is independent of the observing direction, because the turbulence and its structure function are statistically the same over the entire field, the atmospheric turbulence and the instantaneous induced aberrations depend on the direction of observation. As the distance between the reference star and the scientific object increases (given by the angle ϑ), the portion of atmospheric turbulence that is common for both beams decreases, as observed in Figure 1.6a. Therefore, the corrections implemented, which were obtained with the reference star, will not correct all the distortions present in the scientific object wave-front. The angle for which

[3]Wave-front reconstruction using SH-WFS will not be covered in this work because of the vast coverage given by the literature.

the correction is still valid is called the isoplanatic angle, θ_0, and is defined as

$$\theta_0 = 0.31\frac{r_0}{\overline{h}} \tag{1.12}$$

where r_0 is the Fried parameter and $\overline{h}$ is the characteristic average turbulence altitude (Sarazin & Tokovinin, 2002). This value can be interpreted as the maximum angle between the scientific object and the reference star for the correction to remain valid. The opposite effect is called "Angular Anisoplanatism".

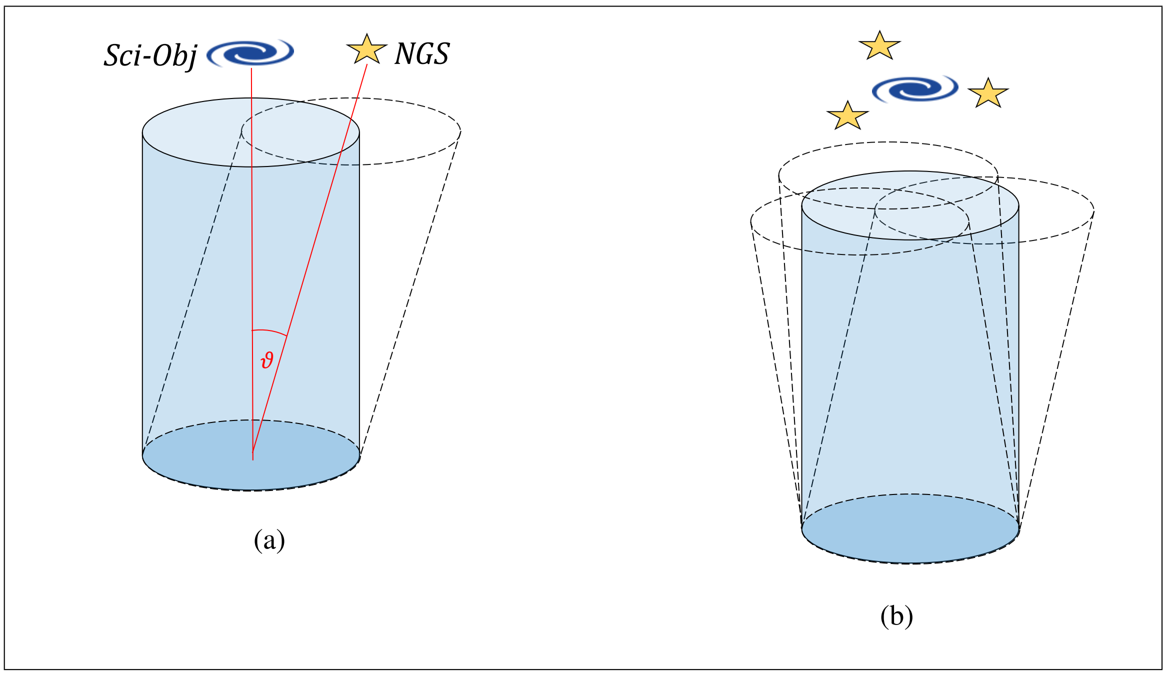

Figure 1.6. (a) Difference of atmospheric turbulence traversed between the light of the NGS and the light of the scientific object. Because of this, all the distortion in the scientific object wave-front produced by the atmospheric turbulence will not be corrected since the turbulence the NGS doesn't "see it". (b) MOAO simplification diagram, showing a three-star asterism allowing it to obtain the information of the distorted wave-front of the scientific object.

Anisoplanatism can be partially overcome using multiple WFS observing multiple objects surrounding the scientific object. The wave-front shape for the scientific object can be approximated using the information obtained with the other WFS observations surrounding the reference stars, as shown in Figure 1.6b. This technique is called “Multiple Objects Adaptive Optics” or MOAO (Assémat et al., 2007), with the advantage of providing correction for a much wider field of view, but with lower quality than a single on-axis object.

So far, both the classical AO and MOAO cases require the NGS to be available within the isoplanatic angle to perform the centroiding process of a SH-WFS. Nonetheless, all regions in the sky do not possess available stars with the required characteristics to perform the wave-front characterization for the scientific object. To overcome this setback, “Laser Guide Stars” (LGS) (Wizinowich et al., 2006) are used.

Inside Earth’s mesosphere, located at an approximate altitude between 80 and 105 kilometers (depending on the place), there is a layer of neutral sodium atoms with a width of $\sim$10 kilometers. The atoms of this layer can be excited with a laser beacon, as is the case with Adaptive Optics, making the sodium atoms radiate light very efficiently at a wavelength of 589nm. This is what is called Artificial or Laser Guide Star.

Because the sodium layer is not thin, the Laser Guide Star generated has a cylinder shape (roughly about 50 cm wide and 10 km long), with an intensity profile that depends on the sodium concentration throughout the layer. When observed from the ground, its intensity and its shape also depends on the atmospheric turbulence.

This technique has setbacks as well. Even though the LGS overcomes the absence of NGS, it also has a series of disadvantages such as a stronger angular anisoplanatism and what is called the “Cone Effect”. The LGS can’t be placed at infinity, but only Due to this drawback, the beam of light observed by the telescope (and therefore the WFS) does not have a cylinder shape, but rather a cone shape.

As shown in Figure 1.7, the cone shape of a LGS does not traverse through the entire atmosphere as does the light of a NGS or the scientific object. Through the reconstruction and correction process there is a significant portion of atmosphere that is not being compensated, because it is in fact not observed by the WFS.

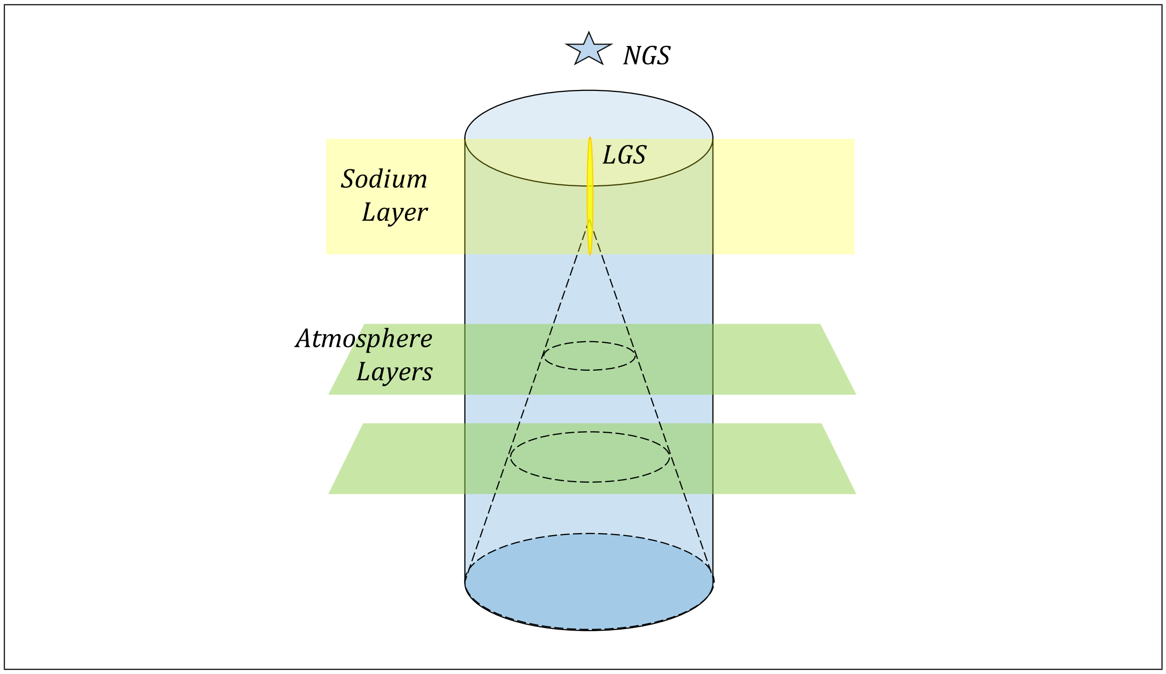

Figure 1.7. A LGS (yellow ellipse) is formed exciting the sodium layer. Because it is placed at a finite altitude, the beam observed by the telescope does not have a cylinder shape but a cone shape, which result in less turbulence observed.

1.2.4. LGS and the centroiding problem

LGS are formed by exciting the sodium layer on the mesosphere, which has a finite thickness of $\sim$10km. When observed from the WFS, the LGS will present a degree of elongation due to the perspective of observation. The perceived elongation by each sub-aperture varies with the distance between the laser launching location and the sub-aperture (r) and by the characteristics of the sodium layer, such as depth (σ_{Na}) and altitude (h). Equation 1.13 and Figure 1.8 describe the elongation in terms of these parameters.

$$\tan(\theta) = \frac{\sigma_{Na} r}{h_0^2 + h_0 r + r^2} \tag{1.13}$$

This last Equation describes the angle of elongation that the LGS has on the wave-front detector. The angle varies with the square of the altitude, which cancels out the variation of intensity due to the distance with the detector, thus determining that the intensity profile

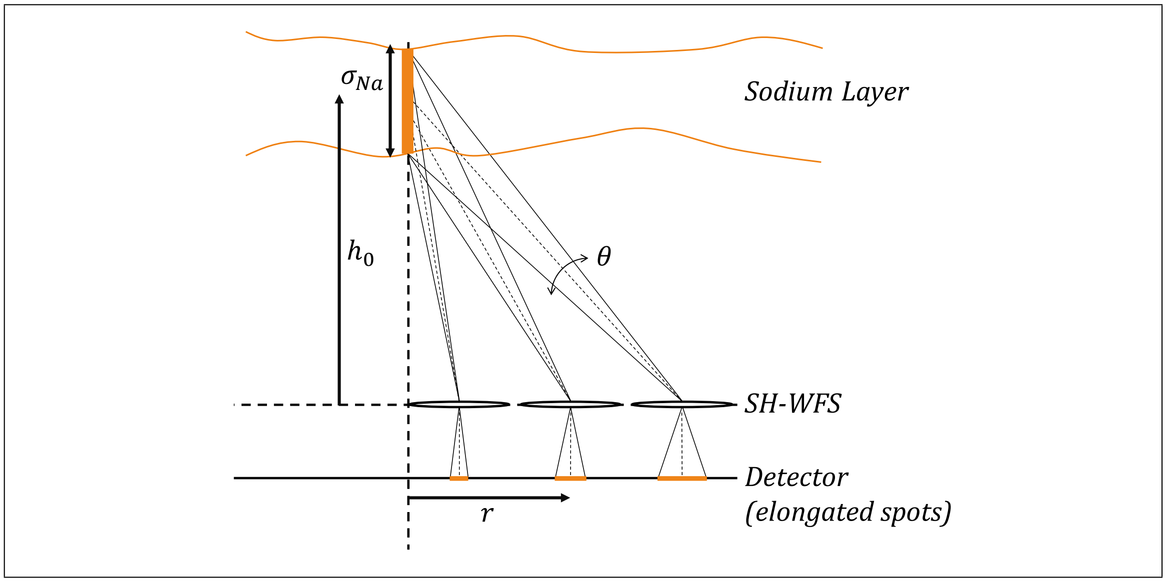

Figure 1.8. LGS elongation on each subaperture. The elongation changes as a function of the distance between the sub-aperture and the laser launching location, the average altitude of the sodium layer and its density profile.

of the LGS has the same structure as the density profile of the sodium layer. This is a key feature of said phenomena later used for the laboratory emulation (van Dam et al., 2011). Figure 1.9 is an image obtained with the WFS of the AO system of the Keck Observatory while observing an LGS. The spot elongation can be observed in all the SH apertures (the right side saturation corresponds to the laser launching location, which leaks light into the WFS and saturates the region).

Atmospheric turbulence distorts the LGS wave-front, resulting in a distorted LGS image. When the centroid calculation is performed, the measure obtained is affected by the variations produced by the atmospheric turbulence as well as by the dynamics of the sodium layer profile. Because of LGS nature, the cone effect and angular anisoplanatism can be observed by each sub-aperture as well.

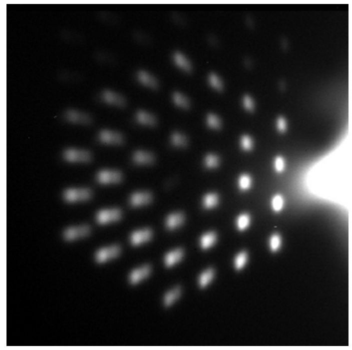

Figure 1.9. Image obtained with the WFS of the AO system of Keck Observatory, located in Hawaii, observing a LGS. The spots formed by each lenslet display the characteristic elongation given its distance from the laser launching location. The right side saturated area is produced by the laser light leaked into the WFS.

1.2.5. Artificial Neural Networks (ANN)

Artificial Neural Networks (ANN) are computing systems where a network of processing nodes self-organizes in order to perform a given numerical task. This system self-organization is considered as a learning process, in which its performance is progressively improved.

An ANN is based on a collection of units or nodes (usually called neurons) connected to each other. Analogous to a biological brain, these connections act as axons, sending signals from one node to another. Some of the nodes have a single external connection, receiving input or sending output signals. When the different nodes are arranged depending on how they are connected between each other, they can be organized in layers. The standard architecture of ANN has three different types of layers: An input layer, one or more hidden layers, and an output layer.

Figure 1.10 presents an example of the standard topology of an ANN. For this case the input layer has 3 nodes (represented by the letter i), the hidden layer 4 nodes (represented by the letter j) and the output layer 2 nodes (represented by the letter k).

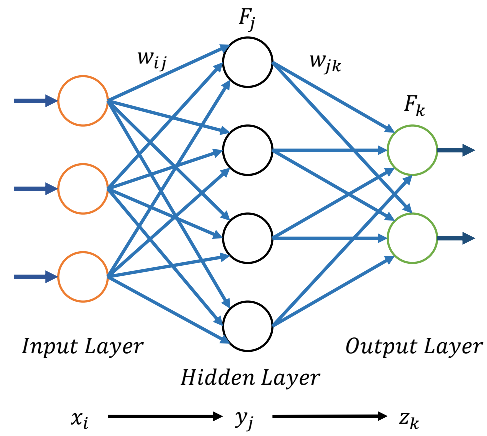

Figure 1.10. Artificial Neural Network general topology.

Each node represents some sort of non-linear transfer function (F_j or F_k). In general, a function similar to hyperbolic arc-tangent is used because of its "threshold" shape, with the exception of the input layer. Usually, this layer is transparent so that each value x_i is directly propagated to the first hidden layer.

Each axon propagates a scalar value between nodes, multiplying it by a characteristic scalar weight w_{ij} or w_{jk}. Then, subsequent nodes receives a series of weighted scalar values adding them as a weighted sum, which is the argument for its non-linear transfer function. The resulting value is the output of the node, that is also multiplied by another characteristic weight as it is sent into another node in the next layer. This propagation is represented by Equations 1.14 and 1.15.

Once the architecture of the ANN is defined, the network "learning process" begins. One of the most widely used methods is known as "Back-propagation", utilized in this work and covered in Section 3.2.

$$y_j = F_j \left\{ \sum_i x_i w_{ij} \right\} \tag{1.14}$$

$$z_k = F_k \left\{ \sum_j y_j w_{jk} \right\} = F_k \left\{ \sum_j F_j \left\{ \sum_i x_i w_{ij} \right\} w_{jk} \right\} \tag{1.15}$$

1.2.5.1. Application of ANN in Adaptive Optics

Artificial Neural Networks have been implemented in many applications such as pattern recognition, data clustering, open-loop automatic control, among many other tasks. In Adaptive Optics, ANN has been used for the control of Deformable Mirrors (Guzmán et al., 2010), Open Loop Tomographic Reconstructors (Osborn et al., 2012), as well as in other processes. A new implementation of ANN in AO was proposed for the centroid calculation of elongated LGS (Mello et al., 2014). Through simulation, this novel technique has proven a superior performance compared to the current techniques (Gilles & Ellerbroek, 2008) in the presence of turbulence and high noise, due in large part to its advantage of coping well with the variable conditions of the atmosphere, the sodium layer and the detector. To fully prove this technique, a series of steps are required. First, it is necessary to elaborate a more complete simulation considering real atmospheric phenomena, such as the cone effect and anisoplanatism. The next step will involve testing the technique with data acquired in an experimental setup in a controlled environment. The final step will require a test of the technique with on-sky data (real data acquired by a ground-based telescope).

1.3. Hypothesis

This work has two hypotheses, both of which are related to wide field of view astronomical observations. The first pertains to how the loss of quality in the images acquired by BOMBOLO, produced by the mechanical deformations due to a changing gravity vector, can be minimized with a truss-based structure. The second seeks to validate the use of ANN in the centroiding of elongated laser guide star's images obtained by a Shack-Hartmann wave-front sensor with experimental data gathered on an optical bench in a laboratory.

1.4. Objectives

According to the proposed hypothesis, the main objective for BOMBOLO is to design and characterize a mechanical structure for the instrument as well as for its main components and systems. The specific goals are:

- Design of the opto-mechanical components such as the barrels.
- Design and characterize a mechanical structure able to hold the different systems and components of the instrument, ensuring a minimal deformation produced by a changing gravity vector during the exposure.

For the AO part of this work, the main objective is to validate the use of ANN in the centroids calculation of elongated laser guide stars in a Shack-Hartmann WFS with experimental data obtained in an optical bench. The specific goals are:

- Design an optical bench in a laboratory representing a single sub-aperture of a Shack-Hartmann WFS of a new-generation telescope (diameter of 20 meters or more).
- Elaborate the control system for the acquisition of elongated spots over the sub-aperture in the optical bench.
- Characterize the designed system.
- Obtain the necessary data for training the ANN with help from an ANN expert.

1.5. Methodologies

The methodology applied to BOMBOLO is an exhaustive study and analysis of the actual optical design of the instrument. Depending on the physical distribution of the optics, electronics, cryogenics, and other components and systems, a mechanical structure will be designed. Its design will be based on steel beams, similar to other truss-based structures used in astronomical instrumentation. This design will be analyzed and reviewed using finite element analysis based on a Monte-Carlo simulation of the telescope observations.

In the case of the contribution to AO part of this work, which has been called *Smart Centroids*, the methodology applied is the design and implementation of an optical bench with the characteristics needed to replicate the observation of elongated laser guide stars observed by a Shack-Hartmann WFS. This bench will require a module able to reproduce a laser guide star, a module of emulation and control of the atmospheric turbulence, and a module for the data acquisition. These modules will interact and be controlled through MATLAB. Calibration data will be acquired in a first stage to characterize the optical bench and its capabilities. After this, experimental data will be collected for the ANN training and validation process. Then, the data will be sorted and separated into two categories: one for training the ANN and the second for validating the ANN.

1.6. Thesis Structure

The organization of this thesis considers two chapters, one for each contribution developed. Chapter 2 presents BOMBOLO, which starts with the description and analysis of the optical design. In the subsequent section, an analysis of the resolution limit of the instrument is presented, considering a comparison between the limit of diffraction, optical aberrations and the seeing or atmospheric turbulence limitations. After that, there is a section including a study of the telescope motion and its effects during the observation, which contributes to the changes in the gravity vector. This leads to a Monte-Carlo simulation that identifies the critical observing cases, later used on the finite element analysis. The last section presents the mechanical design of the barrels and its structure as well as a Finite Element Analysis of them using the results of the Monte-Carlo simulation.

Chapter 3 covers all the work related to Smart Centroids. The work related to the Laboratory Bench implementation is presented at the beginning: Optical Design and Characterization, LGS Generation, Phase-Screen control system, Control Cycle and Data Acquisition Processes. Then, a brief description of the ANN is presented, which includes its training and validation process as well as an analysis of its performance.

Chapter 3 also includes a second stage of this work, which was implemented with the objective of obtaining more "real" data, and therefore, a more realistic performance of the ANN. A new optical design was elaborated and characterized, and modifications were made to the control system of the Phase-Screen. This stage possessed greater challenges that were more difficult to solve; therefore, this part was inconclusive at the delivery point of this thesis. The limitations, possible solutions, and future efforts for this second design are also presented.

At the end of each chapter there is a detailed summary of the work achieved and the obtained results. After the second chapter, the global conclusions of these works are presented as well.

2. BOMBOLO

BOMBOLO is an imager able to perform fast photometry observations in three different bands of the spectrum, simultaneously and independently. It is proposed as a visitor instrument for the 4-meter telescope in the SOAR Observatory.

2.1. Optical Design

BOMBOLO's optical design was elaborated by Damien Jones, an experienced Optical Design Consultant and owner of PRIME OPTICS. BOMBOLO's optical design, in its more basic description, is a focal reducer. As shown in table 2.1, SOAR telescope forms an image at a focal ratio of f/16 on a surface with a minor curvature concave to the sky. After the light is focused by the telescope it is received by a Field Lens, which acts as the pupil of the system and significantly reduces the beam divergence. Then, it is sent to a collimator of 50mm diameter, followed by three optical systems, which form images at focal ratio f/2.5 over separated detectors. A detailed optical description of the instrument can be found in appendix A.

Table 2.1. SOAR Telescope main characteristics.

Characteristic	**Value**
M1 Diameter (Pupil)	4100mm
M1 Curvature Radius	-13.509m
M1 Conic Constant	-1.0026
M2 Diameter	980mm
M2 Curvature Radius	-2.0326m
Plate Scale	3.025 arcsec/mm
Effective Focal Length	68.175m
F-Ratio	16.63
FoV (angular diameter)	14.4 arcmin

2.1.1. Collimator

The collimator is a series of optical components that "collimates" light, meaning that the rays coming out of it are parallel to each other and the wave-front is nearly flat. The optical design of the field lens and collimator is shown in figure A.2. There are three components arranged after the field lens in a "reverse telephoto" configuration, where the central negative and relatively thick meniscus (CL2) reduces the field curvature of the system and controls its length. The last component (CL3) controls the generated "sphero-chromatism". This configuration forms an image of the pupil at 120mm from the last surface, for the placement of two folded dichroics. The optical specifications for each optical component in the collimator are shown in table A.1, in the appendices.

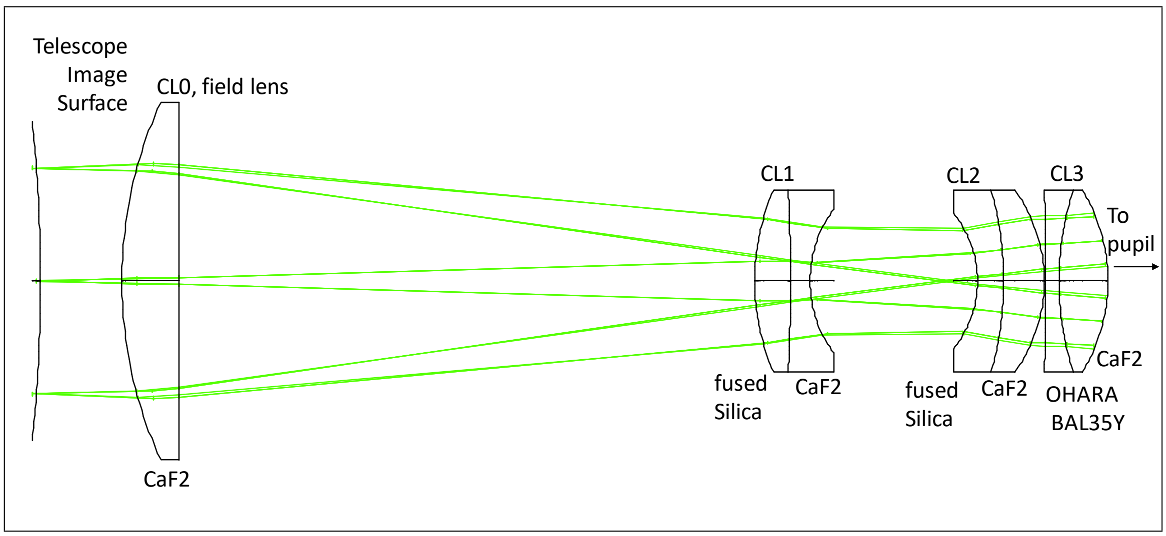

Figure 2.1. BOMBOLO's field lens and collimator optical design. Displayed in the figure are the internal names (CLX) and the material composition for all the lenses. Its total length is around 650mm.

2.1.2. Blue, Green and Red Camera Optical Systems

The three spectral bands are separated by dichroics, as shown in table 1.1, demonstrating that three optical channels are required. These three systems are very similar to one another in that they are based on a 4-component Petzval configuration with field “flatteners”. Each optical arm is optimized for each respective spectral band, resulting in a different composition of materials with different surface curvatures, thicknesses and distances. A general configuration layout of the optical system for the cameras is displayed in figure 2.2, and the optical design specifications for each camera is shown in tables A.2, A.3 and A.4 in the appendices.

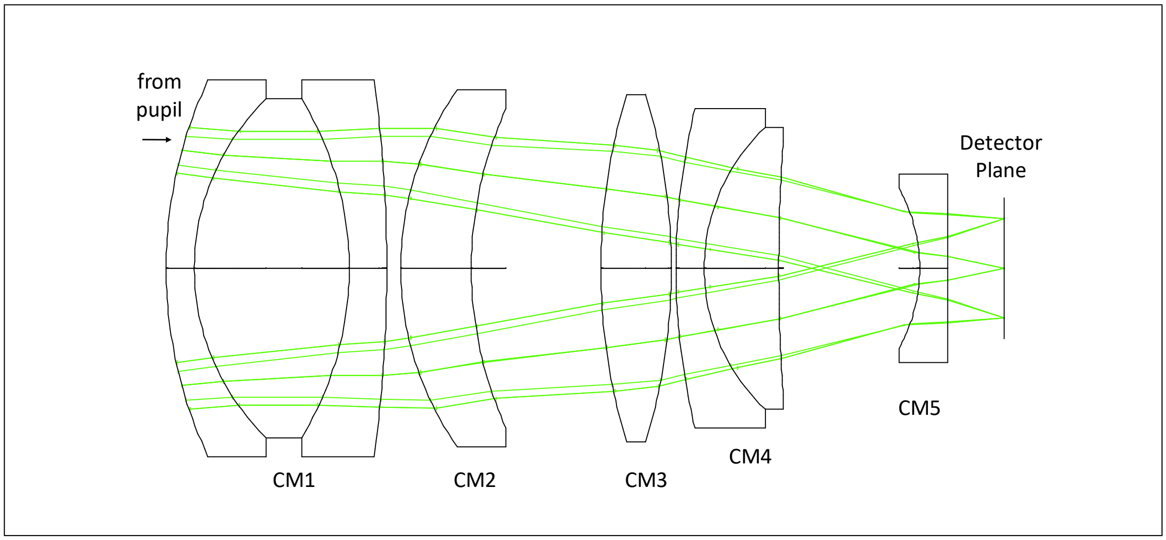

Figure 2.2. Optical Design of BOMBOLO’s camera system. The internal names (CMX) are displayed in the figure. Total length is around 180mm.

2.2. System Resolution Limit

BOMBOLO is conceived to be a seeing limited instrument, meaning that the quality of its images is not determined by diffraction (the ideal situation for most of the instruments), nor by its optical aberrations. To determine if this statement is correct, as well as the potential consequences if this is not the case, a comparison between all the respective limits of resolution is required.

2.2.1. Diffraction Limit

There is a fundamental maximum resolution that a system can achieve, determined by the intrinsic characteristics of the optical system and the phenomena of optical diffraction. Any optical system has two diaphragms or stops: Field Diaphragm and Aperture Diaphragm. The first one limits the angular field within which light can be gathered, while the second one limits the amount of light received from a particular direction in the field. The aperture diaphragm, usually referred to as aperture, defines the theoretical limit of resolution.

The irradiance pattern of a plane wave going through a circular aperture, considering Fresnel propagation for far field (Hecht, 1998, p.463), is given by equation 2.1

$$I(\theta) = I(0)\left(\frac{2J_1\left(ka\sin\theta\right)}{ka\sin\theta}\right)^2 \tag{2.1}$$

where $k = 2\pi/\lambda$ the wave number, and a is the radius of the aperture.

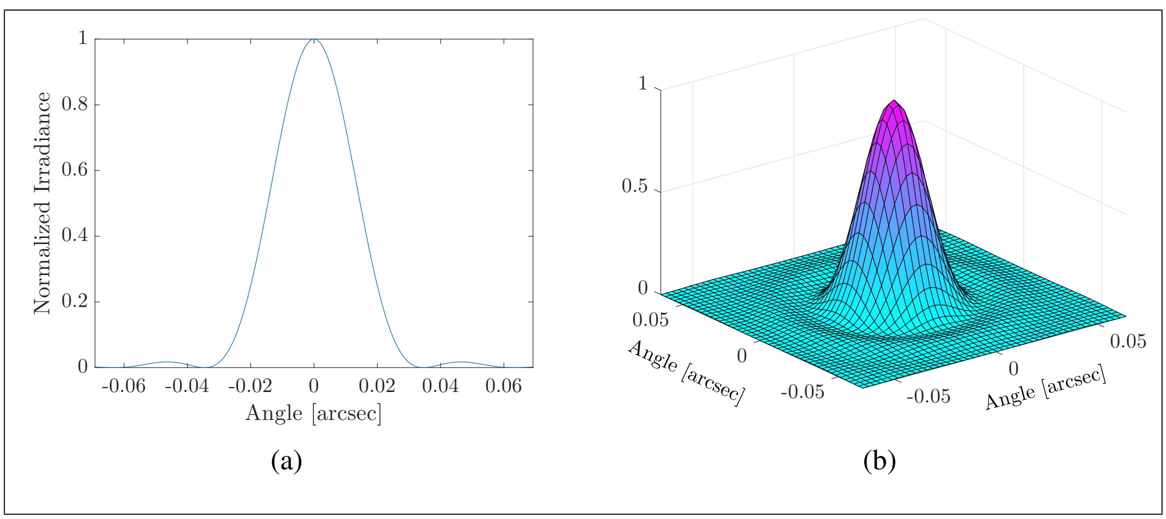

Figure 2.3. (a) Cross section of a normalized Irradiance pattern formed by a plane wave passing through a circular aperture. (b) 3-dimensional version of the same Irradiance pattern. In both diagrams the first minimum is visible, which corresponds to the Airy Disk (wavelength $\lambda = 550nm$ and aperture size of 4 meters diameter).

Looking at figures 2.3a and 2.3b, it is important to notice that the function is symmetrical around the Z axis, it has a maximum at $\theta = 0$, and has minimum wherever the argument of $2J_1(ka \sin\theta)$ is equal to zero. The first zero of the function is given at $ka \sin\theta_1 = 3.83$, which can be used to obtain the equation 2.2

$$\theta_1 \approx 1.22\frac{\lambda}{D} \tag{2.2}$$

where $D = 2a$. This equation is called the Airy Disk, and it defines the maximum limit of resolution that an optical system can achieve. This can be interpreted as the smallest angular distance that must be present between two objects in the sky in order to be differentiated between each other or "resolved". This same angular size can be measured approximately in the focal plane of the optical system by multiplying equation 2.2 with the effective focal length of the optical system ($r_1 = \theta_1\, efl$).

For the SOAR observatory, the diameter of the aperture is 4-meters, and BOMBOLO covers a range of wavelengths from 320nm to 900nm. The Irradiance patterns for the central wavelengths of each channel are shown in figure 2.4, considering paraxial propagation and perfect optics. In this case the PSFs are shown as projected in the focal plane of the system (telescope + instrument). The radius of the Airy Disk for each wavelength is shown as well.

Since optics are not perfect and light transmission is not ideal, the aperture is not perfectly circular. Also, due to other possible effects, the PSF is not always identical to the theoretical one. Figure 2.5 shows the PSF obtained with ZEMAX for the same wavelengths as before, that not only considers the diffraction effects on the aperture but ray propagation, material transmission and other effects as well.

For the blue and green channel, even though the PSF possesses differences in shape and energy distribution with the theoretical cases, the first minimums are very similar ($\sim$0.9 μm for 350nm and $\sim$1.1 μm for 440nm). In the case of 700nm, the PSF appears poorly in regards to its shape and energy distribution, but two things have to be considered.

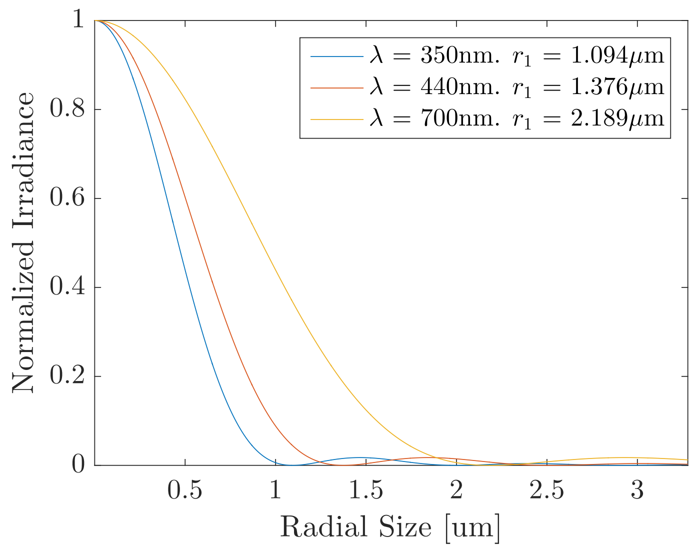

Figure 2.4. Theoretical Point Spread Function for multiple wavelengths covered by BOMBOLO. In the legend, the radius of the Airy Disk for each wavelength (r_1) is shown.

First, the system is optimized for the entire observed field, meaning that the location of the focal plane could potentially not be in the exact place where the on-axis beam reaches a PSF closer to the theoretical one. Therefore, this shift in location could be the reason as to why a destructive interference pattern forms the center of the focused beam. Second, it is important to notice that there is a predominant zero near $\sim 3\mu$m (theoretical PSF has a zero at $\sim$2.2μm) with most of the wave-front energy concentrated under a circumference of 30μm diameter. As a result of the 15μm pixel size the detector does not see the shapes of the PSF.

The pixel size is larger than the limit of resolution of all Airy Disk for all wavelengths in turn providing evidence that the system is not diffraction limited. In order to determine if the pixel size equals the limit of resolution, other effects are analyzed.

2.2.2. Optical Aberrations

Astronomical instruments are not perfect due to many factors that influence their final performance. A way to characterize the performance of an optical system is by the optical

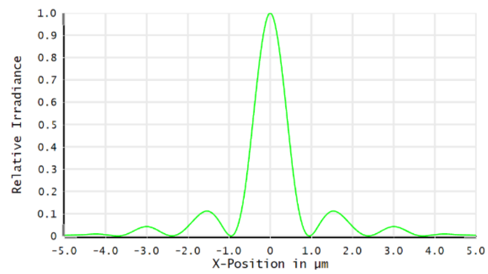

(a) $\lambda = 350$ nm

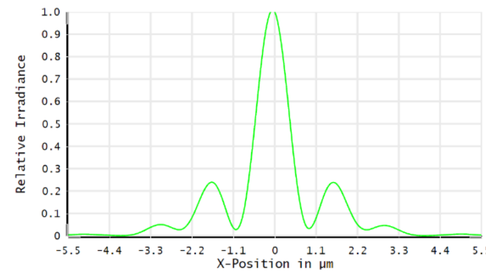

(b) $\lambda = 440$ nm

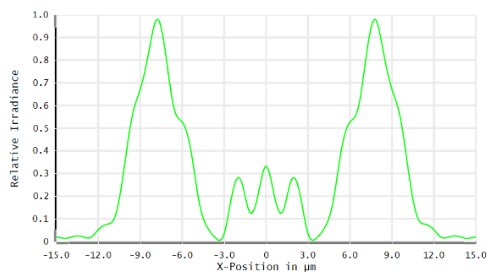

(c) $\lambda = 700$ nm

Figure 2.5. Cross section of a normalized Irradiance pattern formed by a plane wave traversing through the system, obtained with ZEMAX. These diagrams correspond to the wavelengths (a) 350nm, (b) 440nm and (c) 700nm.

aberrations. Even though the paraxial approximation and the simplifications in which it is based upon works fairly well, when it is analyzed at the scale of its limit of resolution the results are not as clear.

It can be considered that a well corrected optical system behaves according to the paraxial rules and forms an image according to the first-order approximation equations. Therefore, the aberrations within an optical system can be defined and measured by some quantity related to how far the rays are from the paraxial image. Because these aberrations affect how the image is finally formed, they affect the image quality of the system as well. The differences between the paraxial ray propagation and the real ray propagation can be classified by how they are produced and how they can be compensated. Many successful efforts have been made to codify the aberrations and try to derive analytic expressions, such as Seidel and Zernike among others. These analytic expressions usually refer to how the wave-front propagates, how the image is formed, and how to describe the aberrations in terms or orthogonal polynomials or power expressions, which match the classification of certain aberrations. The analytic expressions are not a key aspect in understanding how aberrations are formed and behave but instead in classifying them.

The first two main classifications for the aberrations correspond to the Chromatic and Monochromatic aberrations. Chromatic aberrations are dependent upon the wavelength, because they are produced by the dispersion of light. Monochromatic aberrations are produced by the geometry of the optical components, independent of the wavelength.

How light is dispersed depends almost entirely on the material, and the effects produced by this dispersion depend on the wavelength. Rays with different wavelengths will propagate differently, and therefore, the image obtained and its quality will not be the same for different wavelengths.

Monochromatic aberrations can be classified again depending on the "order" of the aberration, determined by the analytic expression mentioned before, as well as how they formed in the ray tracing. A few of these aberrations are Spherical Aberrations, Coma, Astigmatism, Field Curvature, and Image Distortion, among others.

With these classifications, the predominant aberrations in the system can be identified, and not only how they are produced but also how they can be avoided. Nonetheless, determining an approximation of the analytic expression is not necessary in order to study how the optical aberrations degrade the limit of resolution.

A practical way to understand the behavior of these aberrations is through ray tracing. Ray tracing is the analysis and study of how rays of light propagate through the system according to the materials and the geometrical characteristics of them. By propagating the rays of different point sources located in different parts of the field through the optical system using ray tracing techniques, it is possible to observe how different it is from the ideal propagation, which provides evidence of certain aberrations or a mix of them.

The images obtained using ray tracing propagation with point sources are called Spot Diagrams.

For each camera, the spot diagram is obtained through ZEMAX, which considers four different points in the field and three different wavelengths (the two side cut-off wavelengths and the central one). These diagrams are displayed in figures 2.6, 2.7 and 2.8. A small black circle is placed in the center of each spot diagram, representing the Airy Disk and the limit of resolution given by diffraction. The results suggest that because this circle is smaller than the area covered by the dispersion of the rays in the spot diagram, the optical aberrations generated a bigger point source in the detector plane than the airy disk; therefore, diffraction does not limit the resolution of the system compared to the optical aberrations. A common characteristic between the three spot diagram results suggest that nearly the entire point source image is formed within a square window of 30μm size per side, equivalent to the size of two pixels.

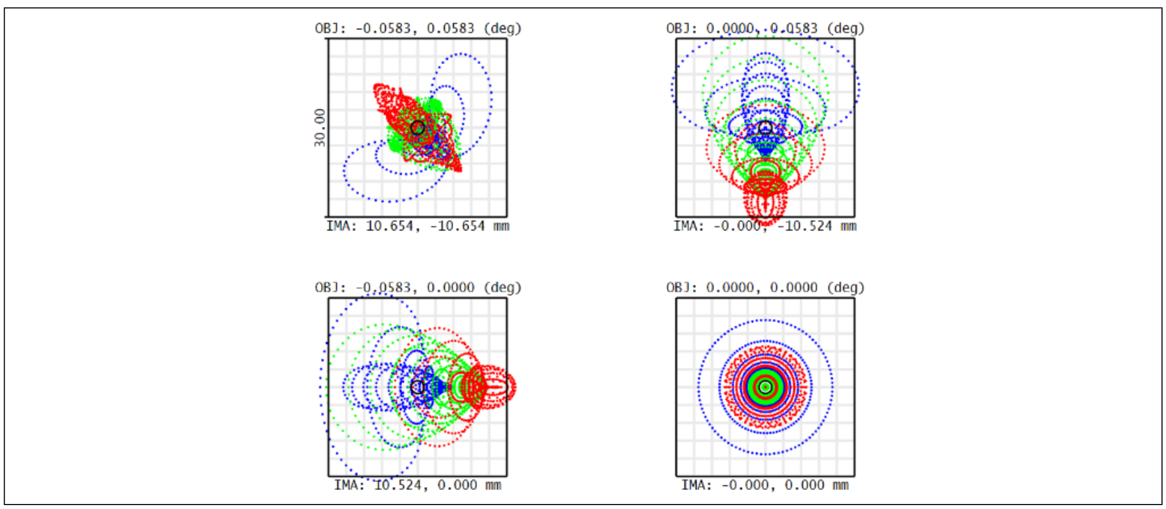

Figure 2.6. Spot diagram of the blue camera, for 4 different fields covering the whole FoV (by symmetry). The blue dots correspond to 320μm, green to 350μm and red to 400μm. The small black circle (barely noticeable) is the Airy Disk. The box scale is 30 μm per side, equivalent to two pixels.

Each figure has four different fields, one on-axis and three off axis located at the edges of the field, in order to study the aberrations throughout the field. Looking into the on-axis

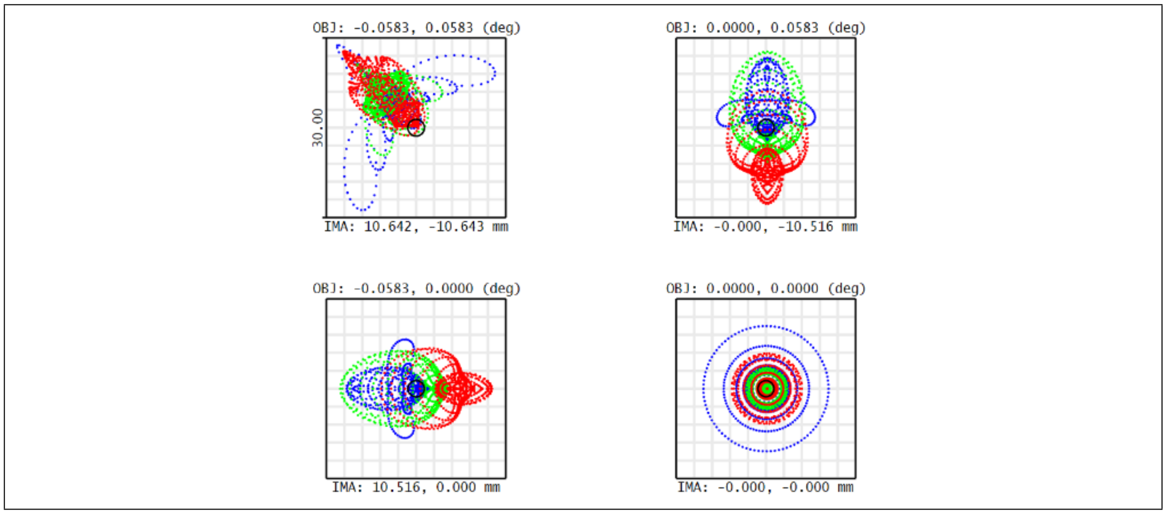

Figure 2.7. Spot diagram of the green camera, for 4 different fields covering the whole FoV (by symmetry). The blue dots correspond to 390μm, green to 440μm and red to 560μm. The small black circle (barely noticeable) is the Airy Disk. The box scale is 30 μm per side, equivalent to two pixels.

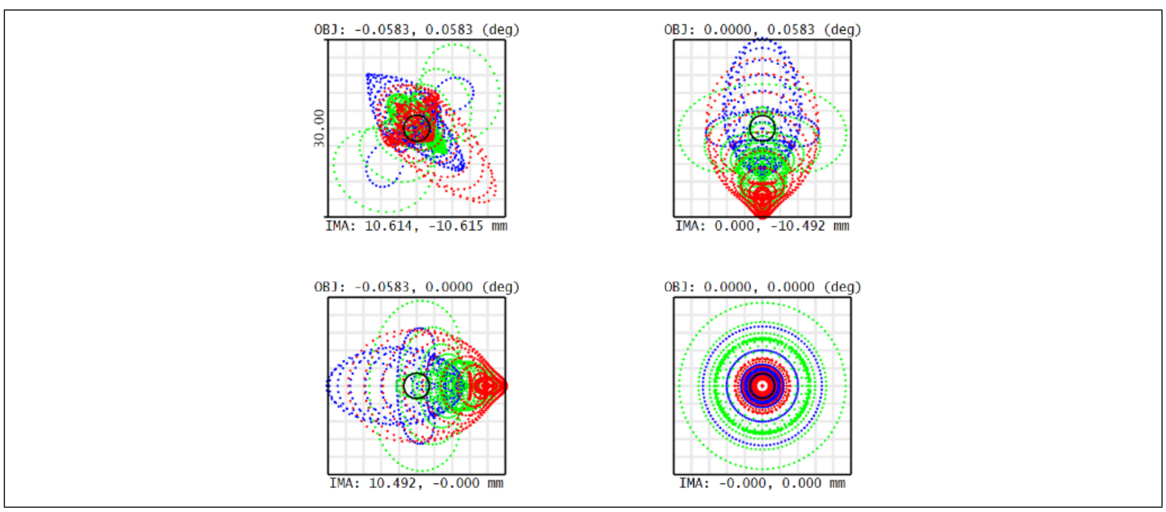

Figure 2.8. Spot diagram of the red camera, for 4 different fields covering the whole FoV (by symmetry). The blue dot correspond to 550μm, green to 700μm and red to 900μm. The small black circle (barely noticeable) is the Airy Disk. The box scale is 30 μm per side, equivalent to two pixels.

field (bottom right diagram) it is clear that for each wavelength the rays do not converge on a single point, rather they divert more or less depending on the wavelength. This effect is known as spherical aberration. When looking at the top and left fields, which are identical but simply rotated, the results show a sort of droplet shape as well as an axial elongation. These two shapes are related to coma and astigmatism aberrations. In the top left diagram, astigmatism can be observed as well as a strong diagonal elongation, and for the blue and green wavelengths there exists a degree of coma. Additionally, a small chromatic aberration is noticeable.

Nonetheless, as previously mentioned, the scale of the aberrations was similar to 2 pixels; hence, given the size of these aberrations and how the light is collected by the pixels, these aberrations are not perceptible in the images acquired. Thus, it can be stated that the limit of resolution of the system is not defined by optical aberrations either but, rather, for the size of the pixel.

2.2.3. Atmospheric Turbulence – Seeing Effect

The effects of atmospheric turbulence in regards to image quality were covered in section 1.2. If the aperture is bigger than r_0, the PSF of the system will not be defined by diffraction but by the Long Exposure PSF (LEPSF), and this will define a new limit of resolution according to the properties of turbulence. The LEPSF generally has a bell shape, similar to a Gauss function, where its FWHM is

$$\varepsilon = 0.98\frac{\lambda}{r_0} \tag{2.3}$$

which is called *Seeing*. Usually, the average seeing values are obtained when a site testing is performed. The seeing is wavelength dependent and for site testing it is usually obtained at λ of 500nm. In order to calculate the equivalent seeing for other wavelengths, equation 2.4 has to be used

$$\varepsilon_\lambda = \varepsilon_0 \left(\frac{\lambda_0}{\lambda}\right)^{1/5} \tag{2.4}$$

where ε_0 and λ_0 are the seeing and wavelength measured in the site testing.

Using site testing data from Cerro Pachón, (Tokovinin & Travouillon, 2006; Tokovinin et al., 2003) the seeing for the three central wavelengths is calculated for good, medium and bad atmospherical conditions, shown in table 2.2.

Table 2.2. Seeing Good (10%), Medium (50%) and Bad (90%) for the three main wavelengths of each channel, based on Cerro Pachón Site Testing.

	Seeing [arcsec]		
Wavelength λ	**Good**	**Medium**	**Bad**
350 nm	0.687	1.020	1.568
440 nm	0.657	0.957	1.498
700 nm	0.598	0.888	1.365

With the calculated values of the seeing, the LEPSF can be simulated. These values are displayed in figure 2.9 as a continuous line for the medium conditions. The left dotted lines are for the good conditions while the right dotted lines are for the bad conditions. The FWHM for the best conditions are $\sim$34μm for 350nm, $\sim$32μm for 440nm, and $\sim$30μm for 700nm.

2.2.4. Resolution Limit Results

The analysis performed shows that the limit of resolution is mainly determined by the atmospherical turbulence. In the best atmospherical conditions, the PSF has a size of $\sim$30μm, almost matching the size of the resolution limit given by the optical aberrations. Because the best atmospherical conditions only occur less than 10% of the time, the seeing will be larger than the optical aberrations in most of the cases.

Finally, the "rule of thumb" requires the FWHM of the resolution limit to be sampled at least twice (to make an experimental equivalent with Nyquist) in order to remain within a region of "good sampling". Considering the current optical design, given the pixel size of the detectors (15μm each), the resolution limit is correctly sampled.

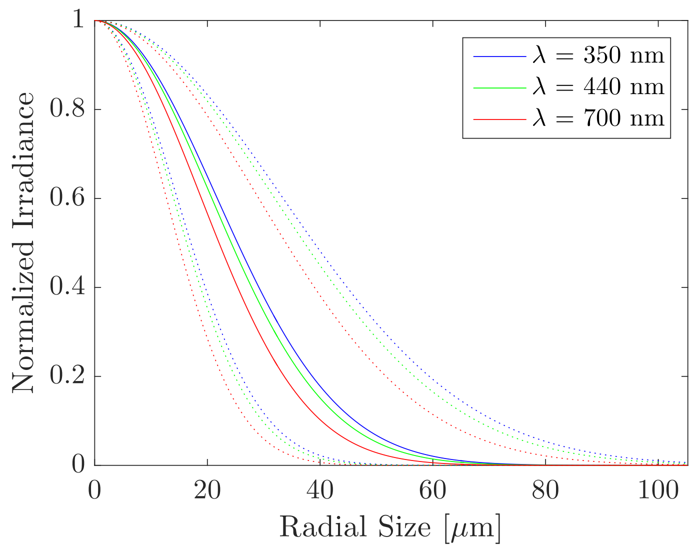

Figure 2.9. PSF derived from seeing on the focal plane for the three main wavelengths of each channel, based on Cerro Pachón Site Testing. Dotted line corresponds to the bad (right dotted line) and best (left dotted line) conditions. FWHM for the best cases conditions are $\sim 34\mu$m for 350nm, $\sim 32\mu$m for 440nm, and $\sim 30\mu$m for 700nm.

2.3. Tracking of Celestial Bodies and the Effects of Telescope Motion

From Earth's perspective, the location of the celestial bodies is almost static, and due to such large distances its motion is imperceptible. When it is perceived that the sky is "changing", the perception of motion is produced by Earth's rotation. Due to this phenomena, nearly any object in the sky follows a circular trajectory when observed from Earth, as shown in figure 2.10. Exceptions to this rule include objects that are closer to Earth, such as planets, asteroids or natural satellites. Two additional points in the sky that appear static from Earth's perspective are called the "celestial poles", which coincides with Earth's rotational axis. Any object located in the poles will appear static because it will not be affected by Earth's rotation[1].

To observe most of the objects in the sky, long exposure times are required. Due to the long window of time it takes for the objects to traverse across the sky, telescopes require

[1] As is the case of Polaris, the star located in the North celestial pole.

Figure 2.10. Star Trail in the Gemini South Observatory, where the circular path stars take is visible because of earth's rotation. Picture from Gemini Observatory web gallery.

specific systems in order to locate the object in the sky and then follow it while capturing its light. To perform this task, telescopes usually have at least two degrees of motion. This motion affects the entirety of the telescope, including all the instruments and systems attached to it, which produces a gravity vector that changes over time for all of them. Each mechanical structure, previously affected by structural deformation due to its own weight, now has added this dynamic gravity vector, resulting in a dynamic deformation.

The motion of the telescope is not random but previously calculated to follow the object's trajectory, and the instrument's location is also known. Therefore, the gravity vector dynamic can be characterized and used to determine the dynamic deformation of the instrument with a finite element analysis of the structure.

To implement this effect, a coordinate system is needed to simulate the tracking of the object. By utilizing the system, it is possible to relate the local position of the telescope on Earth to the positions of the objects in the sky. Two of the most well known coordinate systems used by telescopes for objects location are the Equatorial Coordinate System (also called Celestial Coordinates) and the Altitude-Azimuth (ALT-AZ) Coordinate System (Meeus, 1991; Vincent, 2003).

2.3.1. Equatorial Coordinate System

Stellar object positions are usually expressed as a coordinate pair of angles. In the case of equatorial coordinates, this pair is called *right ascension* and *declination*. A diagram for the equatorial coordinate system is show in figure 2.11. In general terms, the coordinate is almost the same as Earth's geographical coordinate system since it is coincident with Earth's rotational axis and the equator.

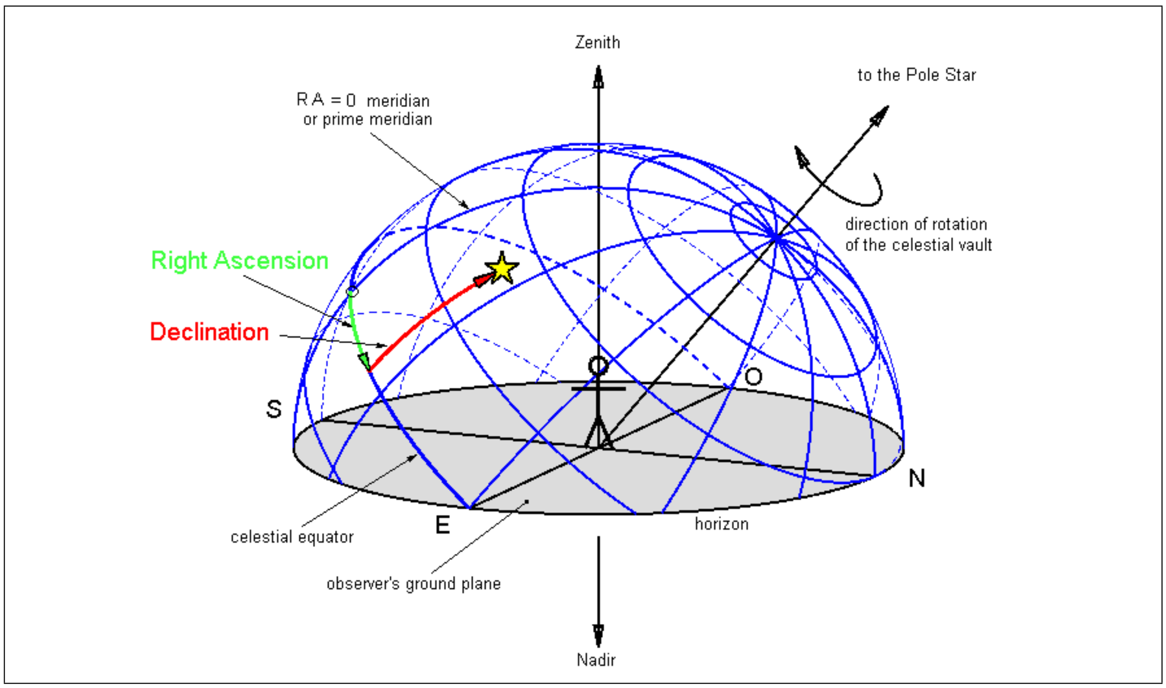

Figure 2.11. Equatorial Coordinate System Diagram. Figure taken from University of Michigan Astrophysics Department web page.

The system is defined as follows: the observer is located in the observer's ground plane, defining the origin of the system. This origin coincides with the center of the celestial sphere, over which the stellar objects appear to be moving. The projection of Earth's equator onto the sky is called the "Celestial Equator" (from now on just called equator), and it defines the angle 0° of the latitude coordinate in the sky called *Declination* (DEC). Similar to Earth's latitude, degrees positive from the equator to the north pole (located at +90°) and negative to the south pole (at -90°). The east-west celestial coordinate is called

Right Ascension (RA), measured conveniently in hours because objects complete a full circumference trajectory in approximately 24 hours, and is measured from an arbitrary zero-point meridian called "Prime Meridian" [2].

The Prime Meridian is parallel to the "Vernal Equinox", which is a fixed direction in space. Equivalently to stellar objects, because of Earth's rotation, the Prime Meridian is not fixed from a ground perspective. In order to identify the position of the prime meridian, or any object and its RA coordinates for that matter, the "Local Meridian" is defined as the meridian that contains the zenith at any time. The angular distance between the Prime Meridian and the Local Meridian changes according to the Local Mean Sideral Time (LMST). To determine the position of any object from a ground perspective, an equivalent coordinate to the RA is the Local Hour Angle (LHA or HA), defined as

$$HA = LMST - RA \tag{2.5}$$

a relationship that can be observed in figure 2.12.

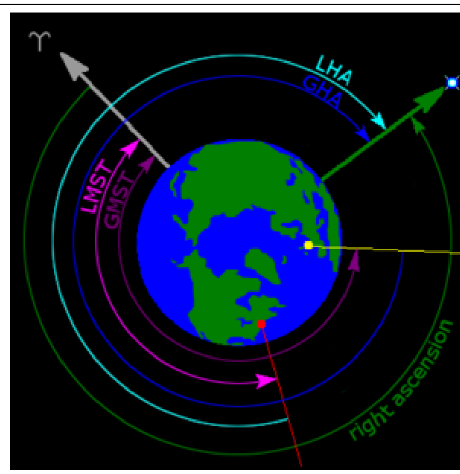

Figure 2.12. As seen from above the Earth's north pole, a star's local hour angle (LHA or HA) for an observer near the red dot. Also depicted are the star's right ascension and Greenwich hour angle (GHA), the local mean sidereal time (LMST) and Greenwich mean sidereal time (GMST). The symbol ϒ identifies the vernal equinox direction. Image obtained from WIKICOMMONS.

[2]This directions receives many names, such as Prime Vertical, Principal Meridian, or Vernal Point.

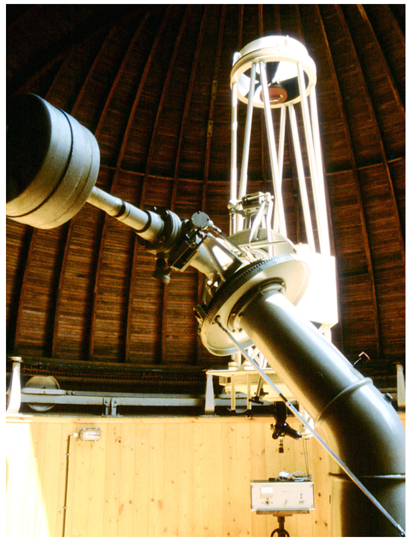

Figure 2.13. The 50 cm Forststernwarte Jena telescope is a good example of an equatorial mount. This picture shows the angle by which the first axis is tilted, parallel to Earth's rotational axis. Also the telescope's counterweight is visible on the left side of the frame.

The goal is to understand the relative motion of the telescope while tracking any object, and not just specific ones. For this work's purposes, the LMST can be defined as zero, and due to this reasoning in later sections RA will be considered equivalent to HA.

Each celestial object follows a circular path concentric to the circle of the equator; therefore, when the pair DEC-HA is observed while the Earth rotates, the DEC coordinate remains the same while the HA coordinate changes. This characteristic is the geometrical base for the Equatorial Mounts.

Equatorial mounts are composed by two axes. When used, one of these axis is parallel to Earth's rotational axis, pointing constantly to one of the celestial poles, meanwhile the other axis is pointing to the object. The first axis rotates at the same rate that Earth's axis revolves, but contrary in direction, all the while compensating the changes in the HA coordinate. Meanwhile, the second axis is fixed at the DEC coordinate of the observing object. This is similar to the motion of a compass in the drawing of a circle: the distance between the tips remain constant (DEC coordinate), at the same time the hand rotates around one of the tips drawing a portion of a circle (portion equivalent to the HA coordinate).

Equatorial Mounts were very convenient to track objects in the sky, as is the case with the telescope Forststernwarte Jena shown, in figure 2.13. Nevertheless, since they require a counterweight to balance the weight of the telescope when the HA coordinate changes, Equatorial Mounts eventually became more impractical to use when telescopes began to increase in size and weight.

2.3.2. Altitude-Azimuth Coordinate System

Altitude-Azimuth coordinate system, also known as Horizontal Coordinates, expresses the position of the stellar objects by utilizing both *Altitude* (ALT) and *Azimuth* (AZ). A diagram of this coordinate system is shown in figure 2.14. Similar to an artillery cannon, this system is based on the rotation of the observer around the vertical axis that goes to the zenith, and a second axis that controls the elevation of the cannon.

As well as the equatorial coordinate system, the observer is placed over the horizontal plane, defining the origin. From the observer's position, both the four cardinal points and the zenith can be located. The meridian traversing the sky from North to South and crossing the zenith is the Celestial Meridian (or Prime Vertical, equivalent to the Prime Meridian for the Equatorial Coordinate System). In the horizontal plane, the azimuth coordinate measures the angle around the zenith, starting at south as 0° and increasing westwards[3] (west is at +90°, east at -90° and north at $\pm$180°). By starting at 0° at the horizontal plane and continuing upwards to the zenith at 90°, it is possible to measure the altitude coordinate. With this system, the celestial pole visible in the sky has an altitude equivalent to the magnitude of the observer's geographical latitude.

The coordinate pair ALT-AZ can define the position of any object in the celestial sphere. Nevertheless, it differs from the equatorial system in that it does not possess a referential mechanism to track the objects, and as a result both coordinates constantly change over time.

[3]It is measured from south because hour angles are measured from the south as well, hence when a celestial body is at the southern meridian, the azimuth is identical to the hour angle

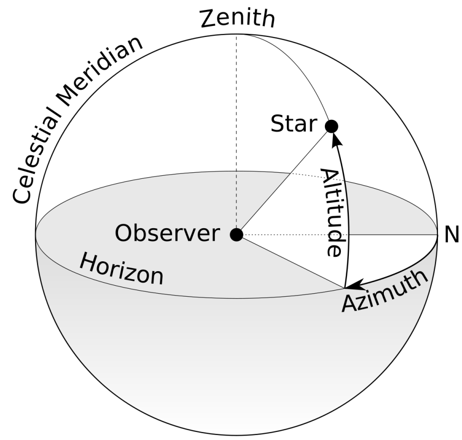

Figure 2.14. Altitude-Azimuth Coordinate System Diagram. Figure taken from Wikimedia Commons.

Figure 2.15. Telescope over an Alt-Az mount.

This coordinate system is used for the ALT-AZ telescope mounts and as mentioned before, works in a way similar to the functionality of an artillery cannon. Nowadays these mounts are the most used among the observatories because of their weight handling capacity. On the other hand, the main disadvantage of these mounts is that they cannot track objects crossing the zenith, in large part due to the 180° immediate turning limitation, for this would require an infinite rotational speed. The maximum zenith angle of observation depends on the maximum rotational velocity of the telescope.

2.3.3. Field Rotation

As previously explained, stars appear to move in circumferences around a point in the sky, called celestial pole, due to Earth's rotation. Angular velocity around the celestial pole is the same for all these objects, as a result the objects traveling over bigger circumferences will appear to move faster than those over smaller circumferences. In other words, when looking at an extended object such as a constellation or a galaxy, the parts further from the pole will move faster than the ones closer.

While using a telescope over an equatorial mount correctly aligned, the telescope focal plane will have the same rotation as the observed extended object, since in this type of mount the telescope itself is rotating around the pole. Therefore, when looking through the telescope, the image will be the same regardless of the time and the object's position.

If the telescope is over an ALT-AZ mount, preventing the telescope from rotating around the pole, then the motion of the focal plane will not match the rotation of the elongated object. Consequently, the image of the observed field will be rotated from the focal plane of the telescope. This phenomenon is called "Field Rotation", and is shown in figure 2.16. The field of view of each telescope is displayed as a colored frame (red for ALT-AZ mount, yellow for Equatorial), with the corner marked to define certain orientations while the object is observed. Both telescopes observe the Big Dipper Constellation, starting in the upper frame. As the constellation rotates counter-clockwise the equatorial frame rotates with the constellation, and as a result the orientation of the frame matches the orientation of the constellation every moment. On the other hand, because the ALT-AZ mount does not match this rotation, the orientation of the frame will not match the orientation of the constellation at any moment except at the beginning.

Depending on the coordinates of the object, the latitude of the observer, and the exposure time, this phenomena is either perceptible instantly or not perceptible at all. When it is perceptible, the object will not be static in the frame during the observation, consequently the detector will retrieve a blurred image. This reduction of image quality can be detrimental to the quality of scientific results.

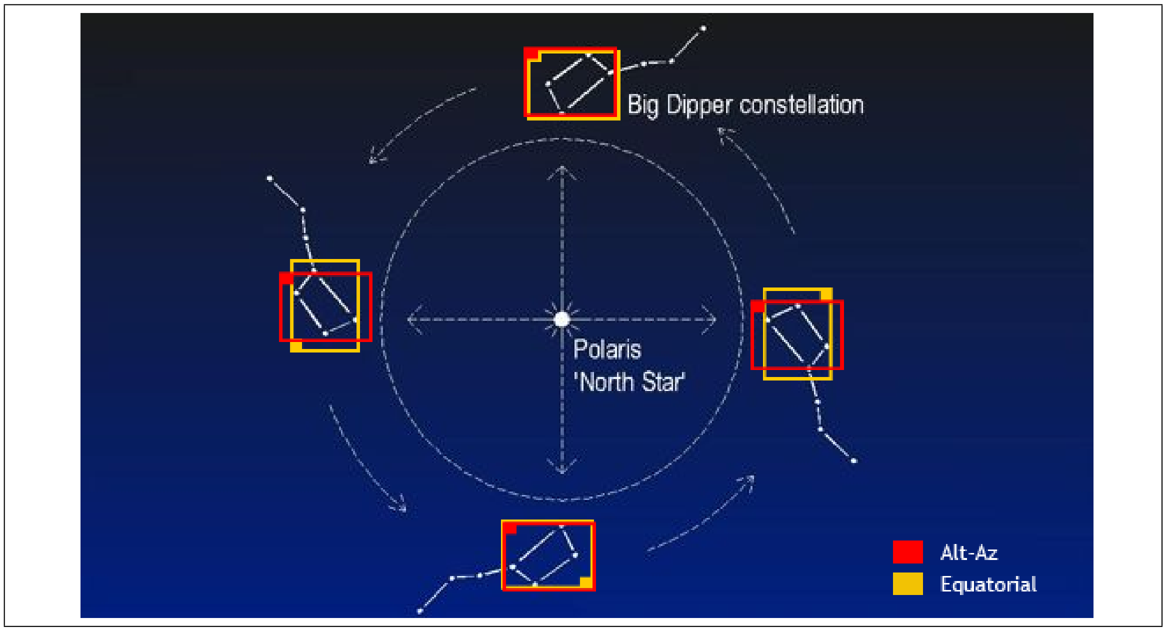

Figure 2.16. Phenomena of field rotation explained. The field of view observed by a telescope over ALT-AZ and Equatorial mounts compared to how they observe the constellation Big Dipper as it revolves around Polaris, the North Pole Star. The corner of the focal plane is marked to perceive the observed field orientation on the telescope.

Nonetheless, the rotation of the field of view over the focal plane of the telescope is not random but, rather, dependent on certain parameters of the observation. This allow the system to compensate the field rotation.

Field Rotators are an interface module between the telescope and the instrument/detector. They can rotate at the exact same rate as the observed field yet opposite in direction, making the focal plane of the system to appear static on the detector. The exact rate can be controlled with a closed loop control system, by tracking various objects simultaneously, or by an open loop, which utilizes a calibrated system and a series of equations that describe the field rotation depending on the ALT-AZ coordinate pair, Earth's rotational velocity, and the observer's geographical latitude. Field Rotation rate is defined by equation 2.6

$$FR_{rate} = W\frac{\cos(\delta)\cos(AZ)}{\cos(ALT)} \tag{2.6}$$

where $W = 4.178 \times 10^{-3}\ ^\circ/second$ is Earth's Rotation angular rate, δ is the observer's latitude, and ALT-AZ is the coordinate pair altitude-azimuth of the object. Because it depends on the current ALT-AZ coordinates of the object, the rate changes as the object moves. In order to obtain the total field rotation of the focal plane while tracking an object in the sky within two instants, it is necessary to know all the coordinate pairs for the path the object is following, acquire the field rotation rate curve for that path, and integrate these values over time.

Figure 2.17 shows the field rotation rate for multiple points in the sky, ranging between -180° and 180° for azimuth and between 0° and 80° for altitude.

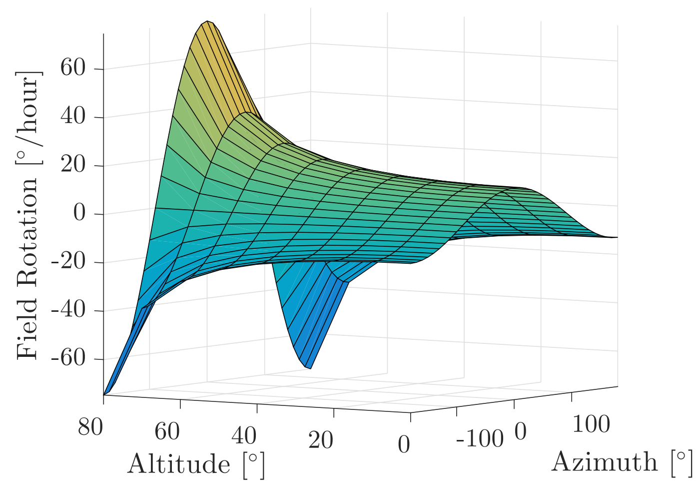

Figure 2.17. Field Rotation Rate for multiple points, where azimuth ranges from -180° and 180°, and altitude from 0° and 80°.

2.3.4. Four-Quadrant Coordinate System Transform

Both coordinate systems are an orthogonal basis that maps the same space (the celestial sphere), meaning that a linear transformation exists to transition from one system to the other.

The equations to go from the equatorial system to the Altitude-Azimuth system are listed below. Equation 2.7 returns the Azimuth and equation 2.8 returns the altitude.

$$\tan(AZ) = \frac{\sin(HA)}{\cos(HA)\sin(\delta) - \tan(DEC)\cos(\delta)} \tag{2.7}$$

$$\sin(ALT) = \sin(\delta)\sin(DEC) + \cos(\delta)\cos(DEC)\cos(HA) \tag{2.8}$$

The equations for the transformation from the ALT-AZ system to the equatorial system are listed below. Equation 2.9 returns the Hour Angle (equivalent to Right Ascension) and equation 2.10 returns the Declination.

$$\tan(HA) = \frac{\sin(AZ)}{\cos(AZ)\sin(\delta) - \tan(ALT)\cos(\delta)} \tag{2.9}$$

$$\sin(DEC) = \sin(\delta)\sin(ALT) + \cos(\delta)\cos(ALT)\cos(AZ) \tag{2.10}$$

Considering that the angles correspond to a four-quadrant area, in order to recover the equivalent four-quadrant coordinate transformation it is necessary to use the function `atan2` from MATLAB or from a similar software. In the interest of obtaining the correct result, equations 2.7 for HA-DEC to ALT-AZ need to be rewritten respectively as equations

$$\sin(AZ) = -\frac{\sin(HA)\cos(DEC)}{\cos(ALT)} \tag{2.11}$$

$$\cos(AZ) = \frac{\sin(DEC) - sin(\delta)\sin(ALT)}{\cos(\delta)cos(ALT)} \tag{2.12}$$

and for ALT-AZ to HA-DEC equations 2.9 and must be rewritten as equations

$$\sin(HA) = -\frac{\sin(AZ)\cos(ALT)}{\cos(DEC)} \tag{2.13}$$

$$\cos(AZ) = \frac{\sin(ALT) - sin(\delta)\sin(DEC)}{\cos(\delta)cos(DEC)} \tag{2.14}$$

With these equations it is possible to obtain the four-quadrant coordinate system transformation, which is useful for the Monte-Carlo simulation presented in the next section.

2.3.5. Monte-Carlo Simulation for critical exposure cases

SOAR 4-meter telescope rests on an ALT-AZ mount, which means that BOMBOLO needs a field rotator to compensate the rotation of the focal plane during the observations. For that reason, the changes on the gravity vector are not only a result of the telescope motion for tracking but a product of the field rotator as well.

A Monte-Carlo simulation is elaborated to generate different starting points of in the sky, with different exposure times (from a few minutes to hours), as well as to retrieve as an output the ending position in ALT-AZ coordinates of the telescope, and the field rotation accumulated. For the purpose of achieving the desired result, the 4-quadrant coordinate system transformation is utilized in addition to the field rotation rate integration. With these three parameters, the new angular orientation of the gravity vector is obtained for both the starting and ending points of observation. These results are indexed and listed to obtain what are considered the most detrimental cases of observation for the mechanical structure. Then, these cases are fed into the Finite Element Analysis to study the behavior of the structure and the three focal planes, shown in section 2.4.4.

The scripts for the implementation of the four-quadrant coordinate transformation, the Field Rotation Rate and absolute difference angles, and the Monte-Carlo simulation can be found in appendix B.

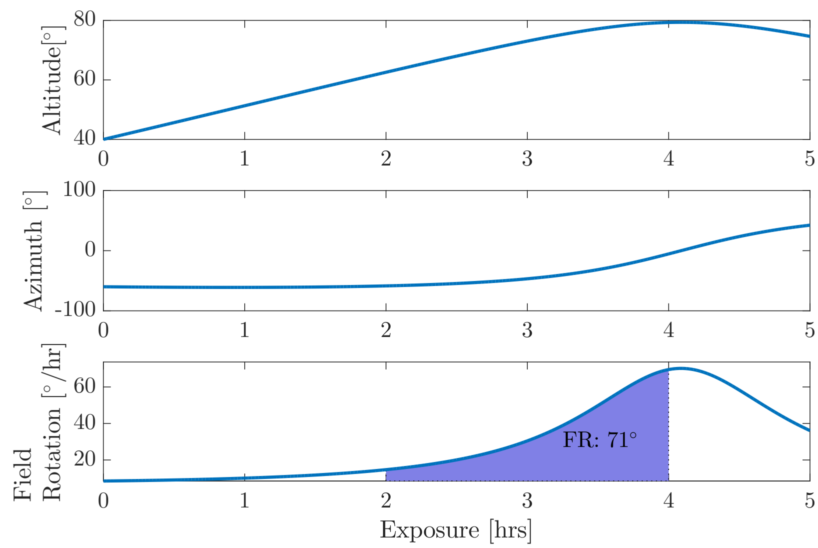

Figure 2.18. Field Rotation example. The object starts at (ALT,AZ) = (40,-60), tracking during 5 hours. The first two plots show how the ALT-AZ coordinate pair change during the tracking, and the third one shows the Field Rotation rate. The area under the curve is the total field rotation between 2 and 4 hours is 71°.

Figure 2.18 shows a case of tracking in ALT-AZ coordinates during a total of 5 hours, for an object located at (40,-60) at the beginning. The first two plots display how the coordinate pair changes during the observation throughout the tracking, while the third shows the Field Rotation rate that the instrument should have in order to compensate the rotation of the field. The integration of this curve retrieves the total field rotation between two points, in this case the plot between the 2 and 4 hours which is 71°.

2.4. BOMBOLO's Mechanical Design

One of the most common materials used for the construction of mechanical structures in astronomical instrumentation is aluminum. It has a low density which makes it lighter for small structures and is easy to be machined. Utilizing this material in mechanical structure also presents a few disadvantages. Aluminum is not as strong as other metals, placing it under a higher probability of suffering deformations. Additionally, it has a low elastic limit, which it is compensated by using bigger pieces with wider cross sections, and the aluminum that has a good metallic composition with low level of impurities and a adequate treatment is very expensive.

With these characteristics and considering BOMBOLO's budget and general concept, it has been proposed to build the small mechanical components with aluminum and the structural parts with ASTM A36 STEEL, based on the following analysis.

Truss Theory establishes that the maximum deformation of an anchored beam with an uniformly distributed load over its length (in this case, its own weight) and is given by equation 2.15

$$\Delta_y^{max} = -\frac{\rho L^4}{8EI} \tag{2.15}$$

where ρ is the material's density, L is the length of the beam, I is the second momentum of inertia of the cross section, and E is the Young module. When considering two identical beams of aluminum and steel, it is important to note that the length and momentum are identical as well. Density and Young module for both materials are listed in table 2.3.

Table 2.3. Material properties comparison between aluminum and steel.

Material	Young Module	Density
Aluminum 6061	73 GPa	2800 kg/mm³
ASTM A36 Steel	200 GPa	7850 kg/mm³

Using equation 2.15 it can be noticed that the steel beam has around 2.33% more deformation compared to the aluminum beam. With these results it is possible to confirm the proposition of materials, all the while focusing on cost reduction.

The objective of BOMBOLO's mechanical structure is not only to serve as housing for the optics, electronics, cryogenics, and other hardware elements, but also to minimize the deformation of the system in order to obtain images with the best quality possible during the exposure. Compared to other structures, it does not attempt to minimize the mechanical failure rate but instead to minimize the optical path changes while observing.

BOMBOLO's optical path is a long optical train of three channels observing different wavelength bands. Its biggest optical component is the Field Lens, with 220mm of diameter. The optical length of the instrument is around 1300mm. Two dichroics are placed after the collimator, followed by the optics for each channel, The following section describe the design of the optical barrels and their mechanical structure are described, including a finite element analysis for these components.

2.4.1. Optical Barrels

The barrels are the structures that contain the optical components and interact directly with them. It requires a very meticulous design with quite strict tolerances. They aspire not only to achieve the highest possible stiffness, but also to keep in high consideration the limitations given by the manufacture process. Four optical systems can be placed into barrels including the Collimator and the three camera focal systems. All of these systems are very light individually, with their weights are listed in appendix C. Distances between the optical elements of each system are relatively small, which is proved in appendix A.

There are many mechanical configurations that a barrel can have, which depend on multiple variables such as weight, diameter, length, and optical power of the system, among others. Each one of these configurations possesses a series of characteristics that improve the contact between the aluminum and the glass of the optics, in order to maintain better distances between components over time and increase the strength of the optical components themselves (Yoder Jr, 2005).

In the case of the collimator, the optical barrel considers three main components: the optical mount or mounting ring, the “spacers”, and the barrel itself.

The optical mount, which is the component in direct contact with the lens, is the one that has the most demanding design requirements and machining tolerances. Usually, it requires that its internal diameter (ID) does not have more than 50μm longer than the lens outer diameter, requirement that arises from three factors. First, if the diameter difference between the elements is too high then the optical element has more freedom to move inside. This causes a higher misalignment in the optical axis with an undesired tip-tilt. Second, the contact surfaces between the lens and the optical mount have a roughness (or imperfections) determined by the machining and polishing processes. Reducing too much the distance between these components can end in a very narrow contact, and even in the impossibility of mounting one component into the other. Third, the machining capabilities given by the manufacturer resulted in 20–40μm, value obtained after several consultations.

The Optical Mount also consider a threaded retaining ring that locks the optical component in place, with a small groove where an O-ring can be placed. This way the optics remains tight without being damaged by the pressure applied by the retaining ring while this is being set.

The second element is the “spacers”, which are cylindrical components with the purpose of maintaining the distances fixed between adjacent optical mountings fixed. The only unavoidable requirements for these elements are a tight axial tolerance, a strict parallelism between the surfaces in contact with the optical mounts, and a lightweight structure.

The last element is the barrel itself. This is the structure that requires the highest degree of stiffness in order to minimize deformations. It contains all the elements mentioned above, placed concentrically. Additionally, it possesses a closing lid that locks all the components inside of it, and is the structure that remains in contact with the supports for maintaining the barrels in place.

A small groove around the optical mount is placed to insert an *elastomer* component, which allows the contact of the mount and the barrel to tighten. There are also a few side perforations in the barrel and the optical mounts in specific places where closed spaces can be produced. This last consideration improves the mounting or un-mounting process of the optics.

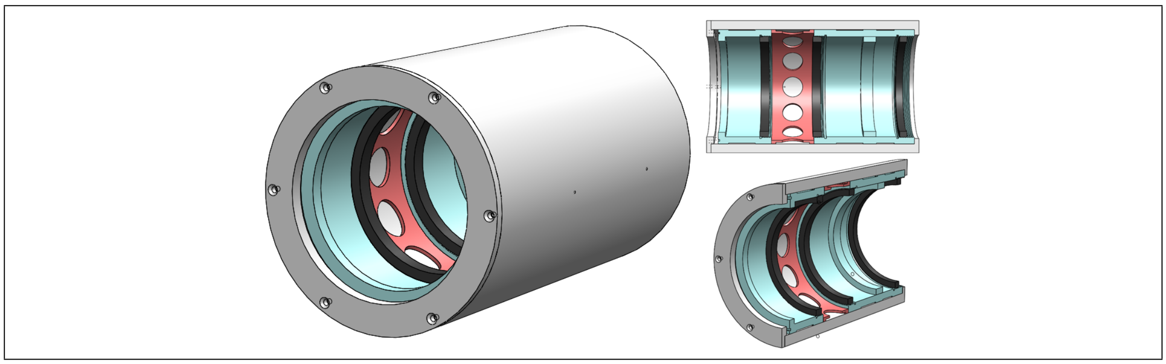

Figure 2.19. Collimator Barrel and a few cross sections. In green are the optical mounts, in red are the spacers, and in gray color is the barrel.

Figure 2.19 shows the barrel for the collimator, with green the optical mounts holding the optics, with black the retaining rings, the spacers in red, and the barrel in gray. The barrel has a length of 238mm and an outer diameter of 148mm.

Since the optics for each channel are smaller and lighter, a simpler configuration for the barrels is used to avoid increasing their weight. The configuration considers only the barrel and spacers, which are located between the optics. These components have the same considerations mentioned above, as shown in figure 2.20. The blue camera barrel has a length of 132.2mm and an outer diameter of 88.1mm, the green camera barrel has a length of 138.7mm and an outer diameter of 100.1mm, and the red camera barrel has a length of 133.4mm and an outer diameter of 100.1mm.

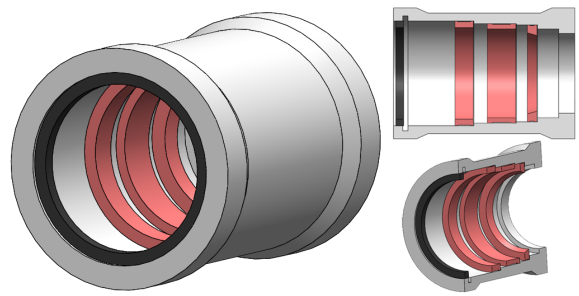

Figure 2.20. Green Camera Barrel and a few cross sections. In green the optical mounts, in red the spacers, and in gray the barrel.

2.4.2. Finite Element Analysis for the Barrels

The collimator barrel is the heaviest barrel because its optical components are the heaviest as well, which is added to the weight of the opto-mechanical elements of the barrel. Nonetheless, the weights of these systems are very light compared to the whole instrument, thus the barrel deformation given its own weight should be very low.

A finite element analysis was implemented in the collimator system. To increase the chances of deformation by its own weight, many "fatal" constraints were considered. First of all, the FEA was implemented only in the external barrel, decreasing its total rigidity, but at the same time including the weight of various excluded components. The weight of other components such as screws and washers were added, and the entire weight sum was multiplied by a factor of 1.2. Also, even though the barrel will be supported by its two sides, the simulation considered the fixed constraints on one side only, similar to a cantilever system. All these considerations would increase the total deformation of the system, and therefore, increase the optical path difference between the light from the input and output of the barrel.

Figure 2.21 shows the results of this FEA, with a 0.38μm as maximum displacement. Two main conclusions can be obtained out of this: first, this deformation is less than 2.6% of a pixel, so it can be considered that the barrel deformation is negligible. Therefore, if there are any optical path changes of the light during the observation these are not result of the barrels weight, but due to the rest of the instrument. Second, because the FEA for the collimator barrel resulted in negligible deformations even for very unfavorable constraints, it was decided that a FEA for the other barrels was unnecessary, considering that the rest of the systems are lighter and shorter.

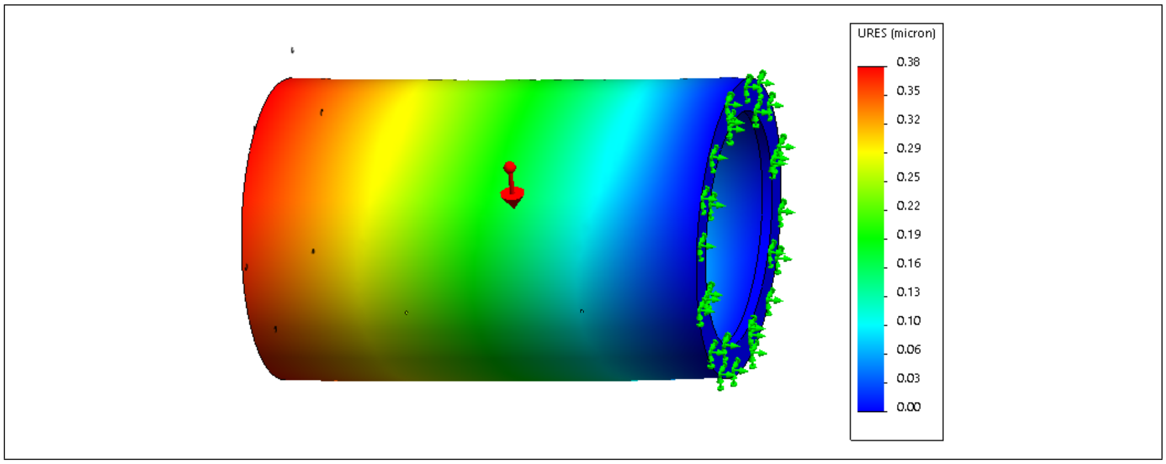

Figure 2.21. Finite Element Analysis of the barrel for a very adverse scenario. Even in this case, the maximum deformation of the barrel is 0.38 μm, which is negligible compared to the total instrument deformation.

2.4.3. Mechanical Structure

There are a few guidelines present in the engineering texts regarding the mechanical design of structures for telescope instruments, mainly because of the diversity of telescopes and the large number of possible optical configurations the instruments can have. The mechanical design covered by said literature is more or less limited to the components that come into a direct contact with optical elements. Therefore, the structure needs to be subject of numerous studies and reviews, and its design must be improved around certain characteristics.

In the case of BOMBOLO, the mechanical structure saw various improvements that can be organized into three design stages. The first stage was the CAD implementation of its conceptual design, which evolved around two aspects: the cost-efficiency of the instrument and its optical design. In this sense, it was decided that ASTM A36 STEEL beams and metallic sheets would be used to design a truss based structure, using the CINTAC catalog as reference for the different beams and sheets available. Figure 2.22 shows this first design and a cross section view of it as well [4].

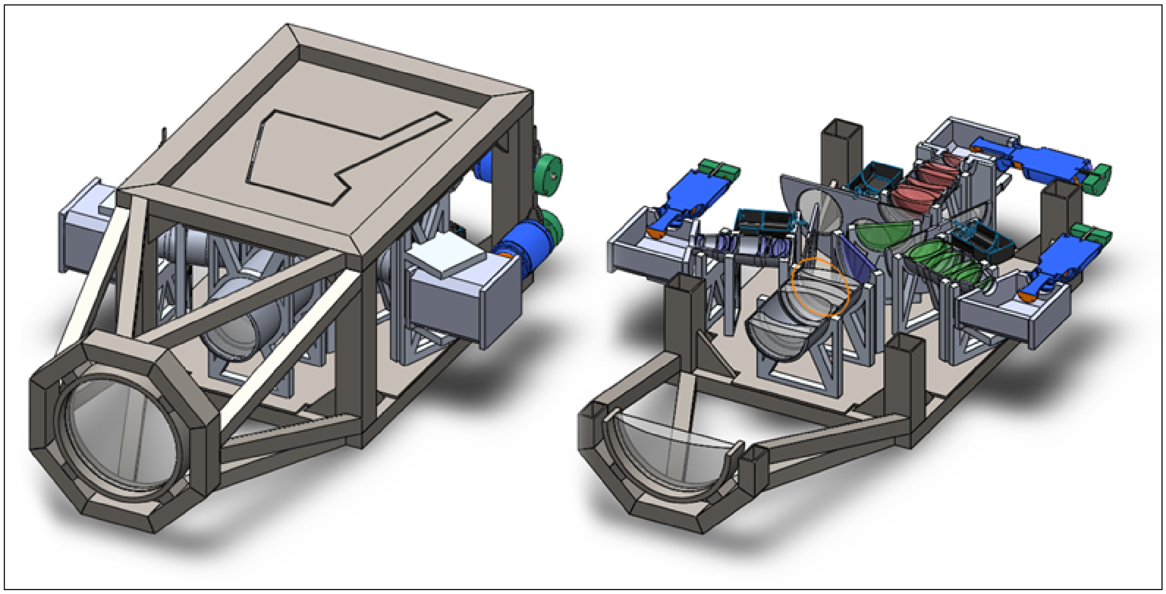

Figure 2.22. First Design of BOMBOLO's mechanical structure with a first approximation of the rest of the components, just as a reference of size and weight.

BOMBOLO's mechanical structure is strongly based on a Serrurier Truss (Kriege & Berry, 1998) configuration, typically used for telescopes. The Serrurier Truss is a design that arose as a solution for the problem of differential flexing between the primary and the secondary mirror of a telescope, which produced significant problems in the light propagation path as well as a loss of image quality. The trusses are designed to suffer a deformation that minimizes the displacements between the optical axis of the optical components. The structure uses pairs of beams revolving around a central pivot cage, where the bottom and top pairs enable the rear and front plates to remain parallel, where the primary and secondary mirrors are held. This configuration acts as a tension-compression

[4] It has to be mentioned that the manufacturer of the optics was going to manufacture the barrels as well, so when the first design of the structure was elaborated the barrels used in the sketches were approximated versions of them. After switching to another optics manufacturer, the task of designing the barrels was adopted as part of this work.

pair. A variation of this is the Dobsonian truss, which uses only one side of the truss. Although it maintains the benefits of parallelism it lacks the advantage of equal displacement between the front and rear planes.

Due to the relatively large distance between the Field Lens and the Collimator, where no other components are present, the Dobsonian configuration allows to hold this distance, in turn assuring parallelism without adding excessive weight. The decision was made to use an octagon to hold the field lens because of the similarity of this configuration to a telescope and its aperture.

The octagon uses beams with a rectangular cross section of 30mm$\times$50mm, with a thickness of 3mm. The outside "diameter"[5] of the octagon is $\sim$163mm. The Serrurier or Dobsonian segment uses beams with a square cross section of 30mm$\times$30mm and thickness of 3mm as well.

The heaviest part of the instrument is located after this segment, which includes the optics for the three arms, the filter wheels, the motors for the filter wheels, the two dichroics, the cameras, the supports, and the electronic and cryogenic components. A simple housing was designed to hold all these systems, using the same rectangular beams as the octagon. The dimensions of the housing are 460mm for the width, 370mm for the height, and 605mm for the length. The total length of the structure is $\sim$1036mm and a total weight slightly over 60kg. As a word of reference, the top sheet has a noticeable weird shape separated from the structure. The goal is to have a similar structure built into the instrument that will function as a hatch to allow easy access to the instrument, not only to change filters in the filter wheels but to adjust the dichroics as well.

A Finite Element Analysis was performed considering this structure for the static case, where the instrument is located in the bent-cassegrain port of the telescope in a horizontal position. The results show a displacement of $\sim$280μm in the focal plane of the red camera. Bearing in mind the size of the pixel of the camera, the displacement is equivalent to $\sim$16 pixels, which is unacceptable as a metric of performance. This was the first point where

[5] Diameter considering the octagon as circumscribed into a circumference.

improvements were implemented in the structure, leading to what is considered the second stage of the design.

Given equation 2.15, it can be observed that the maximum static displacement on the beam can be reduced by decreasing its length or its density or by increasing its Young module of elasticity or its second momentum of inertia. Its density and Young module are properties of the material, while the length is mainly determined by the optical design. Therefore, the second momentum of inertia of the cross section must be increased.

The second moment of inertia is defined as

$$I = \int \int_R r^2 \partial A \tag{2.16}$$

where R is the region of integration and r is the distance from the optical axis to a differential area ∂A. A way to increase this momentum is to increase the area of integration, which can be done by increasing the size and thickness of the cross section of each beam, and increasing the size of the cross section of the whole instrument.

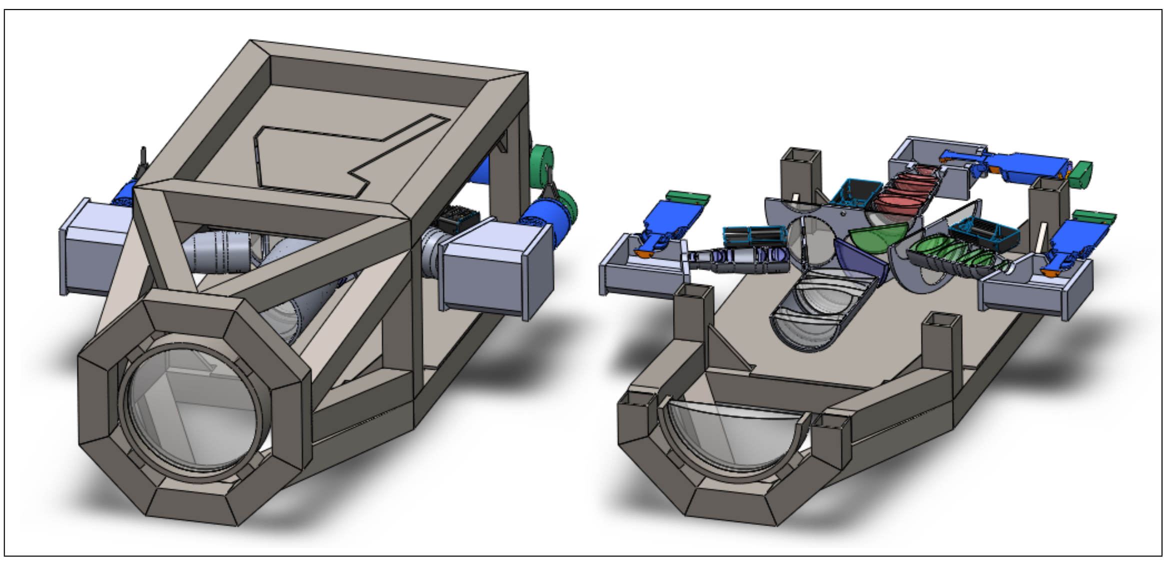

Figure 2.23. Second Design of BOMBOLO's mechanical structure with a first approximation of some of the components.

The implemented changes can be observed in figure 2.23. As previously mentioned, the size and thickness of the beams are larger as well as the instrument structure itself. In this case, all the beams used have a square cross-section of 50mm per side and a thickness of 5mm. The beams of the Serrurier segment have an approximate length of $\sim$390mm, and the main cage has a length of 605mm. The weight of the whole structure is nearly 87kg.

When repeating the FEA static case, the maximum displacement of the red camera focal plane is around $\sim 90\mu$m, which is considerably lower than the previous case but still a significant displacement.

A third and final iteration was elaborated, but due to the relatively small dimensions of the instrument and the large beams used, there was a lack of a good access and working area for future maintenance. The trade-off is that by increasing this "working space" the weight of the instrument and the second momentum of inertia would increase as well. In order to control the displacements, the length of the instrument it has to decrease. The final design of the structure is presented in figures 2.24 and 2.25.

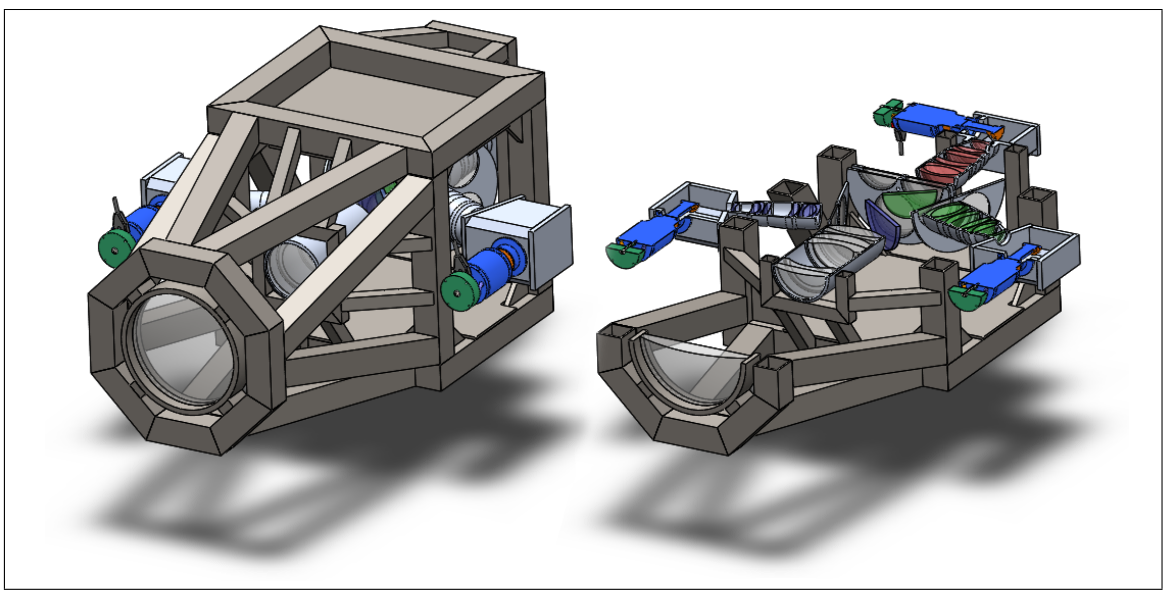

Figure 2.24. Third and final Design of BOMBOLO's mechanical structure with a first approximation of some of the components.

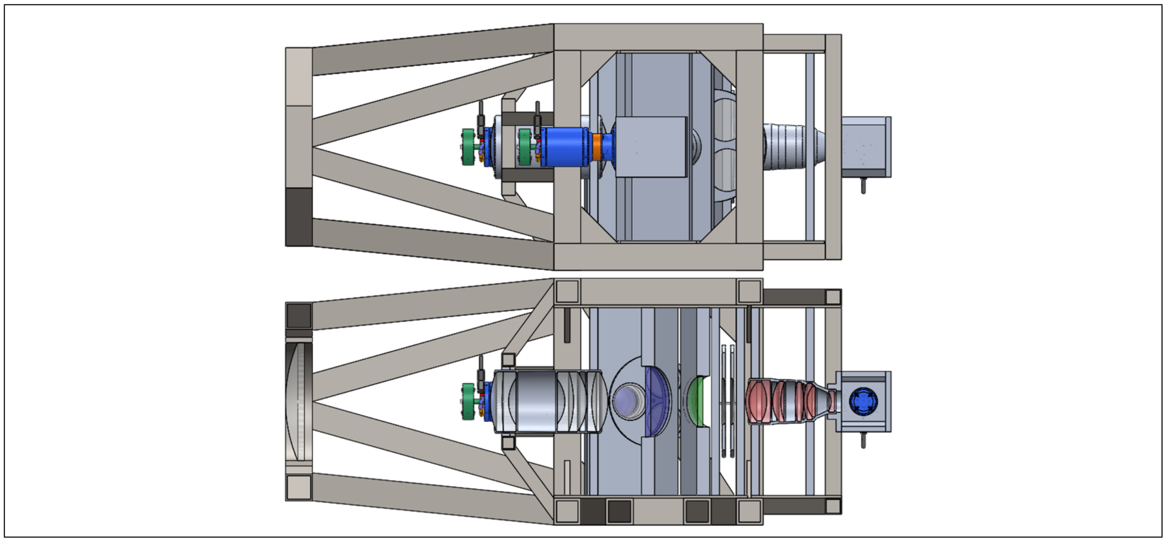

Figure 2.25. Third and final design of BOMBOLO's mechanical. Side view and lateral cross section.

The beams used for the octagon, the Dobsonian segment, and the cage are the same beams used in the second design. In order to reduce the length of the cage, the beams of the Dobsonian segment are longer resulting in a total length of ~470mm. The new dimensions of the cage are 460mm wide, 460mm tall, and 390mm long. Two new sub-structures were added, which are a built-in support frame structure for one side of the collimator. The other one is a secondary cage for the red camera, although smaller and lighter, but with enough strength to reduce deformations at this side. The collimator frame is made of beams with a square cross section of 25mm per side and 2mm thickness, while the red camera cage is made of square beams of 30mm per side and 2.5mm thickness. These design measurements cause the instrument to have a total length of ~1.3m with a structural weight of almost 100kg.

The finite element analysis for this structure is shown in the following section, and a few more detailed blueprints of this last structure can be found in appendix D.

2.4.4. Finite Element Analysis for the Mechanical Structure

For the third design stage of the instrument as well as for the previous designs, a static Finite Element Analysis was performed in order to obtain the vonMises stress and the total displacement given by the deformation. Figure 2.26 shows the results obtained for the vonMises stress, where it can be observed that the maximum stress is around $1.5 \times 10^7 N/m^2$. In the figure, the results saturate the value at $4 \times 10^6 N/m^2$ in order to observe other regions lower than the maximum. This threshold was chosen because only a few points appear over $1 \times 10^7 N/m^2$, while more regions come into sight near $\sim 6 \times 10^6 N/m^2$ concentrated more in the Serrurier part of the structure, in the joints of the beams to the octagon and the main block.

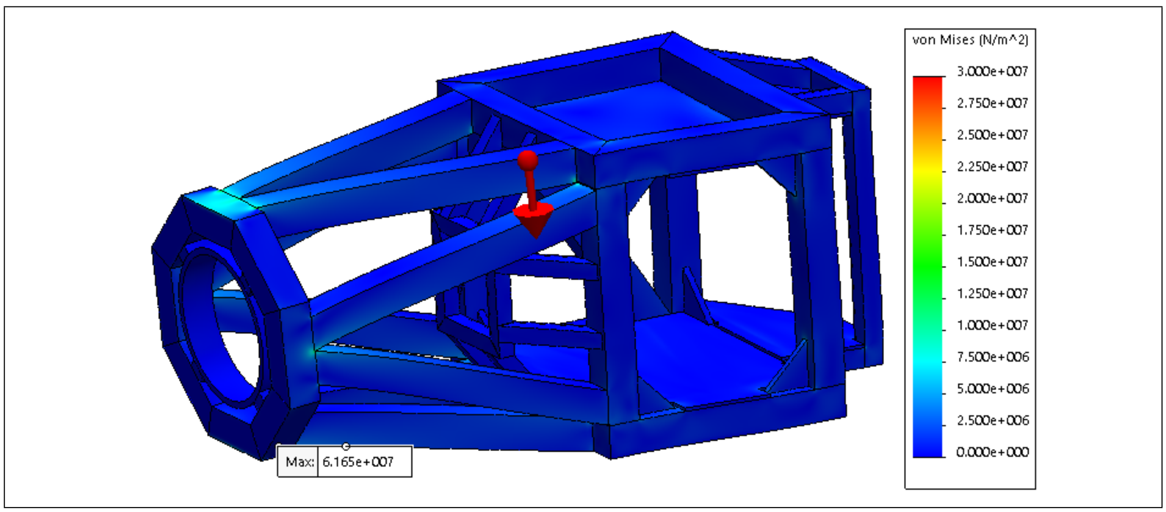

Figure 2.26. vonMises stress results for the third and final structure, for the static FEA case.

For the total deformation and displacements, the structure possesses a maximum deformation of $\sim 38\mu m$, which is equivalent to $\sim 34\mu m$ in the focal plane of the red camera. This is considerably lower than the first design, and it is mostly acceptable as a static deformation for the observations. Figure 2.27 displays the deformation in the structure resulting from the FEA.

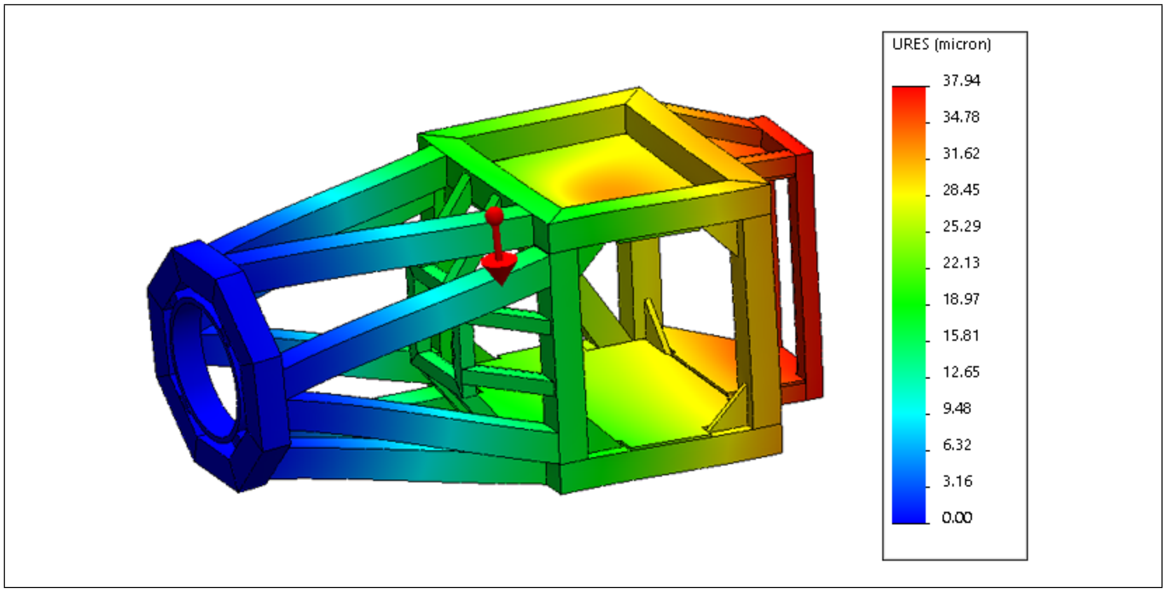

Figure 2.27. Total displacement results for the third and final structure, for the static FEA case.

With the total deformation of the instrument, a curve can be extrapolated of the deformation for each complete optical path, thus obtaining the total displacement of the optical barrels. The tables with the displacements for each optical path can be found in appendix E- These displacements were given to Damien Jones to compute a simulation of the image formed with each displacements included. His comments were as follows:

> The displacements and tilts in the tables have little or no impact on the final BOMBOLO imagery. However, there are a couple of outstanding points for discussion:
>
> • The green camera tip&tilt, with respect to the collimator, will cause an image shift of nearly 0.5 mm because there is an effective angle offset of the camera field. This will be a problem because it will be different for each camera, in linear proportion. If exposures are sufficient to cause differential image shifts between cameras, then this will equate to a loss of resolution.
>
> • There will be an image shift (∼1 pixel) from the collimator tilt, as well, but this will be the same for all the cameras. A matter of more

pertinent concern is the appearance of "keystone" distortion, the seriousness of which will depend on the length of a typical exposure.

The first consideration refers to the fact that if the displacement of the focal plane on each camera is different, then the images on the detectors will be different. Furthermore, if the focal plane displacement changes during the exposure and generates a loss of quality in each image, then the displacements should change differently for each focal plane and the loss of quality should be different as well. If the displacement of each focal plane during the exposure is minimum, the loss of quality can be neglected and the differential displacements between images can be overcome by post-processing the images by cross-correlation.

The second consideration refers to a certain type of image deformation that can be neglected as well if the displacement changes are low enough during the exposure.

Given these comments, the information obtained through the Monte-Carlo simulation was implemented in the simulation for what were considered the worst cases of exposure, and then it was used for a "dynamic" finite element analysis. This simulation analysis is a comparison of the displacements in the three coordinate directions between the initial state, when the exposure starts, and the final state, when the exposure finishes. For this, the initial and final gravity vectors are computed and implemented in two static finite element analysis simulations.

It can be inferred that the worst scenarios correspond to the cases where the gravity vector changes the most. Therefore, where the altitude and the total field rotation components have a larger differential change, alterations in the azimuth do not generate changes in the gravity vector.

There are two main situations where these changes occur. The first situation corresponds to the objects that cross the area that have a similar altitude to the celestial pole but have a lower declination. If celestial objects are considered to be projected onto a plane, it signifies that these objects have the largest radial distance to the pole (as observed in figure 2.10). Therefore, if all objects move in that plane with the same angular velocity, then the "tangential" velocity is higher for the objects mentioned, which produces a higher altitude change for a certain exposure time.

The second situation arises when the total field rotation of the instrument is high. This relates to the points where the field rotation rate is higher, because for a certain window of time these cases integrate the higher field rotation, as can be observed in the example displayed in figure 2.18. For a certain period of time, the maximum integration under the curve is obtained when the period of time is centered in the maximum field rotation. After a review of the results, two exemplary cases emerge with these characteristics, due to an analysis during an exposition of 60 min [6].

The first case is an object traversing through a sector that has an altitude close to the celestial pole (equivalent in magnitude to the observer's latitude) with very low declination. This corresponds to an azimuth angle around $\pm 115°$, which represents the top change in altitude for a given window of time. It is valuable to point out that the worst results for the azimuth angle depends on which bent-cassegrain port the instrument will be placed in. Since the port is located $\sim$45° from the nasmyth port and while the telescope elevates the instrument it suffers a small rotation observed from a gravity vector perspective, and therefore, in one of the azimuth angles this small rotation compensates some of the field rotation, while the other it will appear larger because it is add to the field rotation.

When looking at the results of the Monte-Carlo simulation, the change in altitude is $\sim$10° while the field rotation accumulated is $\sim$15°. For one angle of azimuth the cancellation of field rotation makes the gravity vector almost invariable, and the displacements obtained through the FEA differences are virtually zero (around 1 μm or less). For the other azimuth angle, the displacement in the X direction of the red camera focal plane is $\sim 4\mu$m, $\sim 9\mu$m in the Y direction, and$\sim 1\mu$m in the Z direction, resulting in a total vector displacement of magnitude $\sim 10.5\mu$m.

The second case corresponds to an object located in a region with high altitude, just crossing the Prime Meridian (azimuth 0° or 180°). In this situation the displacements that

[6] Exposure time of 60 min is very rare and unused, considering that usually most of the observations occur around 20 minutes of exposure.)

starts close to 30μm almost fully concentrated in the Y direction changes towards the X direction, considering that the gravity vector changes are given mostly by the rotation of the instrument while compensating the field rotation. For the Z coordinate the displacement also changes about 5μm, starting concentrated in the top side of the instrument, moving to the side (that at the end of the observation is the top side observed from a gravity vector perspective). This represents the most detrimental case of observation, resulting in a vector displacement of $\sim$32μm, similar to the results obtained on the static case.

The results demonstrate that the displacements are similar between the dynamic case and the static case, which is consistent with the gravity vector behavior. Also, the most detrimental scenarios, where the most drastic changes of the gravity vector take place, the displacement changes of the image planes on the detectors can be considered as within the acceptable margins. Therefore, the loss of quality during the observation should be a low concern, because this loss of quality can be overcome in the worst case scenario by utilizing successive shorter exposures.

2.5. BOMBOLO: Technical Summary

A study of the point spread function formed by the instrument was performed to analyze and address the resolution limit of the instrument. The results are summed up in table 2.4.

Table 2.4. Comparison table between the limit of resolution results for the diffraction analysis, aberrations analysis and atmospheric turbulence analysis (seeing).

	350 nm	**450nm**	**700nm**
Diffraction	0.9μm	1.1μm	3μm
Aberrations	30μm	30μm	30μm
Seeing	34μm	32μm	30μm

These results confirm that for most of the cases BOMBOLO's resolution limit is defined by the atmospherical turbulence. Nonetheless, there is a small amount of cases where the resolution limit is defined by the size of the pixel on the detector, since the seeing is smaller than two pixels.

BOMBOLO will be placed in one of the bent-cassegrain ports, located at $\sim$45° from the nasmyth ports. Instruments placed in these ports are more affected more by a changing gravity vector, from the instrument's perspective, compared to the instruments located in the nasmyth ports. When the telescope changes its elevation coordinate while tracking an object, the instrument moves with the telescope. Added to this effect, since the SOAR telescope rests on a ALT-AZ mount, the instrument requires a de-rotator to compensate for the field rotation effect.

Considering these effects, a Monte-Carlo simulation was conducted to identify the worst observational cases, in other words, where the gravity vector changes the most. The results were grouped in two general cases. The first case for objects traversing a sector that has similar altitude to the celestial pole, with an azimuth around $\pm$115° (equivalent to low declination). In this region, the elevation component undergoes the greatest amount of change. The second case groups the cases of objects located in a region with high altitude, just crossing the Prime Meridian (azimuth 0° or 180°). This group of cases gathers the specific characteristic that the accumulated field rotation is the highest among all the observations, and is thus observed as a small change in altitude with a high rotation of the instrument. These two results are later used in the FEA to validate the instrument's mechanical structure.

Two structural systems were designed and evaluated through FEA: the barrels for the optics and the mechanical structure. The FEA for the barrels resulted in displacements lower than 1μm for a highly detrimental case. This signifies that the optical path changes are not produced by the barrels themselves but by the entire instrument.

The instrument's structure considered three design stages, each one improving upon the previous one. The static displacements for the red channel focal plane are around

34μm. This is considering the telescope pointing to the zenith, where the cantilever position of the instrument generates the maximum displacement. This case represents the maximum displacement over the detector.

When analyzing the two cases obtained with the Monte-Carlo simulation, using them to elaborate the "dynamic" FEA, the first case results in a displacement change of $\sim 11\mu$m, while the second results in a displacement change of $\sim 32\mu$m, both during a whole exposure of 60 minutes. This second case is the most detrimental for the observations, because it reduces the image quality. Nonetheless, this quality reduction can be avoided by taking successive shorter exposures, where the displacements are less for each image. Then, by utilizing a cross-correlation post-processing of the images they can be adjusted to be added between each other without accumulating the produced blur effect. These results are summarized in table 2.5.

Table 2.5. Summary of the displacements given the inputs of the Monte Carlo Simulation for the Static Case and the most detrimental Dynamic Cases.

Altitude	**Azimuth**	**Field Rotation**	**Exposure Time**	**Displacement**	**Case**
$90°$	-	$0°$	0 min	$\sim 34\ \mu$m	Static Case
$40°$	$\pm\ 115°$	$\sim 15°$	60 min	$\sim 11\ \mu$m	Dynamic Case #1
$80°$	$\pm\ 20\ °$	$\sim 80°$	60 min	$\sim 32\ \mu$m	Dynamic Case #2

This analysis validates the current design of the structure, which accomplishes the objective of minimizing the loss of image quality generated by the mechanical deformation of the structure. Even though the displacements cannot be avoided completely, the structure has an acceptable performance in most of the detrimental cases, which can be improved by a more methodical observation process.

2.6. Last Comments about the current state of the instrument and Further Work

BOMBOLO is an imager proposed as a visitor instrument for the SOAR observatory, at cerro Pachón. The contribution presented in this chapter describes the design and analysis of its optical and structural components. Nonetheless, other subsystems and components has been designed and elaborated parallel to the ones presented here. Also, other subsystems and tasks need to be completed as well in order to accomplish the objective of building BOMBOLO as a complete instrument.

Some of the required task to achieve the mentioned objective and its current status can be considered:

- **Optical bench for optical testing:** After the validation of the optical design the optical components were acquired. It is necessary to test this optical components in an optical bench to validate experimentally the optical performance of these elements. This would require a telescope optical simulator as well. Once the instrument is fully integrated a second bench is necessary to test the optical performance of the whole instrument.
- **Scientific Cameras:** The development of the scientific cameras has been in charge of Andes Scientific Instruments (ASI), a Chilean company that has proven its capabilities to elaborate cameras with the specifications that BOMBOLO needs. The camera is fully customizable according to BOMBOLO's optical and structural design, as well as to perform in the required ranges of temperature and readout velocity.
- **Acquisition and Control software:** ASI has been developing the software for the image acquisition of the cameras, and has promised the delivery of an API (Application Programming Interface) to be integrated in the elaboration of a complete software to control the whole instrument, including the mentioned scientific cameras, as well as the filter wheels and shutters. Also, the software requires to manage the data transfer from the instrument to the observatory database.

- **Opto-mechanical components and structure manufacture:** The analysis presented here validate the structure as suitable according to the requirement and restrictions mentioned with more detail in previous sections. Hence, the structure and the barrels can be manufactured.
- **Assembly, Integration and Validation:** Once all the subsystems and components of the instrument are elaborated, the instrument has to be assembled, all the electronics, cryogenic and control systems need to be fully integrated, and the performance of the instrument needs to be validated in the laboratory. Parallel to this stage all the documentation has to be elaborated regarding the performed procedures for the assembly. Considering also that the instrument is and will be forever a prototype and not a final stage product, this is the first stage where the troubleshooting and workaround procedures are elaborated, as well as for the maintenance tasks. This stage will be repeated and completed at the observatory, where the instrument will be integrated for the last time before being tested and handed to the observatory for the commissioning.

3. SMART CENTROIDS

AO systems rely on a natural guide star (NGS) to sample the atmosphere. When a sector in the sky does not have the required NGS, an artificial star or laser guide star (LGS) can be used. Usually, LGS has a lower performance compared to a suitable NGS because of angular anisoplanatism and the cone effect. The LGS appears as an elongated object when observed by the SH-WFS. This elongation depends on the thickness of the sodium layer and the distance between the sub-aperture and the laser axis.

The dynamic behavior of the sodium layer and the atmosphere traversed by the LSG produce changes in the shape and position of the elongated object in the WFS. These changes affect the center of gravity (CoG) calculation of the elongated object, resulting in a centroid that is not always the same one that characterizes the slope of the wave-front. This generates an error that is propagated through the AO loop because the DM cannot correctly compensate the phase distortions of the wave-front. Many techniques have been developed and used to improve the centroid values, such as the Constrained Matched-Filter (CMF), which has the best performance but possesses computing limitations.

The implementation of ANN as a new way to calculate the centroid positions has shown promising results, even demonstrating better performance than the CMF in certain cases. In general, ANN has shown better capabilities to cope with the changing conditions of the atmosphere and the sodium layer (Mello et al., 2014), compared to the CMF. The performance of this new technique has been proven through simulation methods, so the natural following step is to prove this technique with experimental data gathered on a laboratory before continuing with data gathered on-sky [1].

As part of this research, two optical benches have been developed in the laboratory to test the performance of ANN with experimental data. With further explanation in the following sections, the second optical bench was built to achieve a better performance than

[1]This chain of procedures is followed because obtaining on-sky data usually is very expensive, mostly because of the nature of this phenomena that requires big telescopes or expensive ways to reproduce data similar on the telescope location.

the first one, also regarding the emulation of certain atmospheric phenomena that the first one was not able to emulate correctly. The second bench will be covered in section 3.3.

3.1. First Laboratory Bench

Different setups can be considered to represent the phenomena of study, each one with its own advantages and disadvantages. For example, to reproduce the laser guide star and its shape, DMs have usually been used. An elliptical laser focuses over the DM, controlling the intensity of the laser in order to emulate the sodium layer density profile. The problem with this setup is that few actuators can be effectively used to control the shape of the LGS, and the dynamic range of the actuators does not produce a high dynamic range for the intensity of the laser; therefore, the emulation of the profile has a low spatial and intensity resolution. Besides, it is complicated and time-expensive to implement the use of a DM. The greatest advantage of this LGS emulation is that the generated star is not two-dimensional as one generated by an screen, but three-dimensional, thus allowing the system to have a perception of depth. This depth perception allows for the projection of different shapes of elongated star in the WFS, depending on the subaperture as the real phenomena.

Even though a setup like the one described would be ideal to reproduce what happens in the sky, to test the proposed technique there is no need to seek out data with all the sub-apertures simultaneously but, rather, a single sub-aperture. This also means that there is no need to look for a three-dimensional extended object but, rather, just the projection of it onto the selected sub-aperture, in turn hardly reducing the complexity in design and implementation of the required bench.

A diagram containing all the modules necessary in the laboratory bench to reproduce these phenomena is shown in figure 3.1. The general concept of this configuration is to form an image of an object simulating the LGS in a detector, distorted by atmospheric turbulence. The components used to implement this configuration are a Samsung S19D3000

Table 3.1. Laser Guide Star Display screen characteristics (Model Samsung S19D300).

Characteristics	Value
Display Size	18.5 inches
Illumination Type	LED
Resolution	1366×768
Pixel Pitch	0.254 μm

desktop monitor for the LGS projection and an AVT [2] MANTA G031-B camera for the image acquisition. The main characteristics of these components are shown in tables 3.1 and 3.2. Regarding the turbulence, a Phase Screen mounted on a rail system, moved by steeper motors and controlled by a microcontroler and a current driver. Each one of these modules is explained with more detail in the following sections.

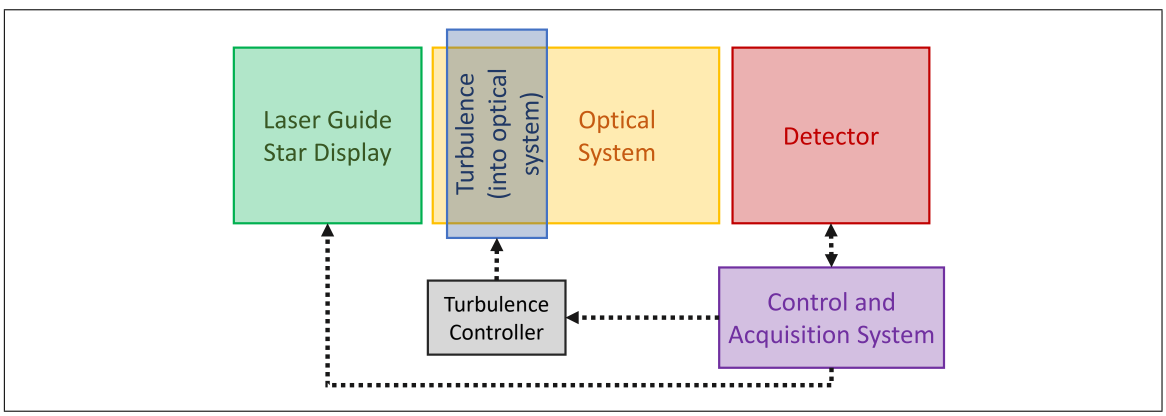

Figure 3.1. Diagram of the experimental bench and its different modules.

3.1.1. First Optical Design

A very simple optical design was implemented using two lenses in a relay configuration. The scheme of this configuration is presented in figure 3.2. The first lens acts as a collimator lens with a focal length of 750mm while the second lens has a focal length of

[2] Allied Vision Technologies

Table 3.2. Detector main characteristics (Model AVT MANTA G031-B)

Characteristics	**Value**
Resolution	656×492
Sensor	Sony ICX618
Pixel Size (pitch)	5.6 μm (square area)
Inteface	Gigabit Ethernet - PoE (optional)

100mm and forms the image of the LGS over the detector. The image formed ends with a $1/7.5$ magnification factor. Placed in between the lenses is a diaphragm, closer to the second lens, working as pupil of the system.

The turbulence, which is produced by a Phase-Screen (PS), can be located in between the LGS and the first lens L1 or between the L1 and the pupil. By locating the pupil in the first position the effects of anisoplanatism and the cone effect can be emulated.

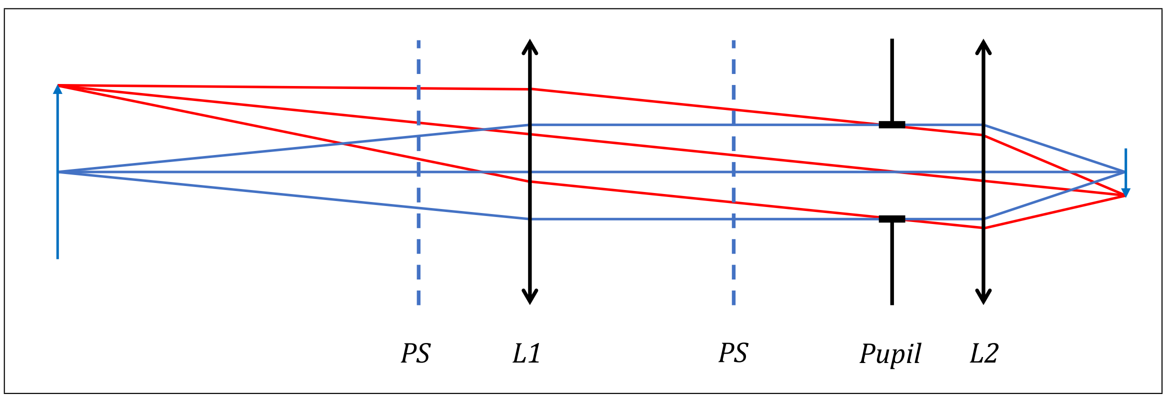

Figure 3.2. Sketch representation of the Optical Design (dimensions are not proportional).

LGS are affected by angular anisoplanatism, which means that different portions of the LGS traverse through different portions of turbulence. The wave-front of these different LGS portions have some similarity between each other, but they are not identical. As observed in figure 3.2, if we consider the arrow in the object plane as the laser guide star and the two proposed positions of the PSF, the tip of the arrow crosses a different portion of the PS than the middle part of the arrow.

LGS travel through the atmosphere as a cone shaped beam, different from Natural Guide Stars (NGS), which travel in a cylindrical shaped beam. Considering the aperture of the telescope as the base for the cone and the cylinder, incoming light from the LGS interacts with less atmosphere than the NGS. Therefore, a LGS based AO loop cannot compensate all the induced atmospheric distortion in the wave-front of the scientific object. This is called the Cone Effect, and it can be described considering the different atmosphere crossed by the LGS and the NGS, and also by the size of the "Meta Pupil" traversed. The Meta Pupil is the projection of the pupil into the different atmospheric layers. As can be observed in the cone effect, the Meta Pupil decreases with the altitude, resulting in a different relationship between the distortion given by a certain layer and the effective pupil.

This optical design is implemented in the optical bench locating the PS in the space between the Objects Plane (LGS) and the first Lens, at different positions.

Locating the PS between the LGS and L1 emulates anisoplanatism and the cone effect. Locating the PS between L1 and L2 emulates only anisoplanatism, which is similar to what is observed when low layers of turbulence are the predominant layers regarding energy distribution. Nonetheless, given the configuration and the real distances of this design, the angular difference between the on-axis and off-axis beams is very small, making the anisoplanatic effect almost negligible.

Table 3.3 shows the specifications for the first optical design for the Smart Centroids laboratory bench, where two commercial optical components were used from THORLABS.

3.1.2. Sodium Layer and Laser Guide Star Generation

Many systems can be used to emulate the LGS in the object plane of the optical system. In this case, a computer screen is used to generate a line of pixels with different intensities, which will represent the different density concentrations of the sodium layer.

Table 3.3. Smart Centroid first design optical specifications.

Component and surface	**Radius of Curvature [mm]**	**Thickness [mm] (to next surface)**	**Glass Material**	**Semi-Diameter [mm]**
LGS	Infinity	750.00		0.50
AC508-750-B	-2,910.00	2.50	SF10	25.40
AC508-750-B	291.07	4.20	N-BAF10	25.40
AC508-750-B	-376.80	200.00		25.40
PUPIL	Infinity	10.00		10.00
AC508-100-B	65.77	13.00	N-LAK22	25.40
AC508-100-B	-55.98	2.00	N-SF6HT	25.40
AC508-100-B	-280.55	91.48		25.40
Detector Plane	Infinity	–		–

In order to generate different laser guide stars, a calibration of the screen is required to determine the different plate scales achievable with the bench and how to relate them to what a common telescope observes. Also, measuring the non-linearity of pixel's brightness is required, thus the intensity of the pixel relates correctly with the density of the sodium layer.

The first set of calibration images are acquired by the detector without the PS in the optical path, and a grid of non-adjacent pixels with a known separation between each pixel in the screen is displayed. The observed separation between pixels of the screen is equivalent to $\sim$6.5 pixels of the detector camera.

The rest of the calibration images are acquired by illuminating only one pixel on the screen and placing the PS into different positions along the optical path. After first obtaining different single exposure images of the PSF and then obtaining an average of them, a retrieval of the "Long Exposure PSF" is possible. The obtained image has shape similar to a Gaussian bell, which has a size of $\sim$11.5 pix at FWHM.

It is desired to have a plate scale similar to 0.5"/pix or as close as possible all the while considering the angular size of the turbulence in observatory sites. A current system in use such as the Canary System (Myers et al., 2008; Morris et al., 2010; Osborn et al., 2014) has a 0.64"/pix plate scale. To achieve a similar plate scale the following relationship is applied:

$$seeing[arcsec] = 11.5[pix] \times 0.5 \left[\frac{arcsec}{pix}\right] \times \frac{1}{N} \tag{3.1}$$

where N is the binning. Different sizes of seggin can be obtained through varying the value of N, and therefore, using the same scaling several plate scales as well. This can be observed in table 3.4

Table 3.4. Different seeings and plate scales obtained after specific binnings.

Binning	**Seeing [arcsec]**	**Plate Scale [arsec/pix]**
5×5	1.15	0.65
6×6	0.96	0.54
7×7	0.82	0.46

By using similar images to obtain the long exposure PSF, the centroid displacement can be characterized as well as the signal-to-noise ratio of the short exposure PSF. As observed in figure 3.3, the SNR ranges between ∼5 and ∼13, a ratio that will increase after the binning process.

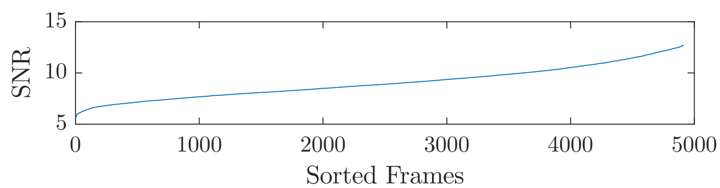

Figure 3.3. First Optical Bench - Images SNR.

Figure 3.4 shows the histograms for the centroid displacement in the X and Y coordinate. As can be observed, the standard deviations of the displacements in each direction, S_x and S_y, are under one pixel. Although considered low, with the SNR values it can be affirmed that the background noise does not overly contaminate the measure. It is relevant to mention that the shape of these histograms is not entirely identical to the expected outcome and the reasoning of which will be explained with the analysis of the second optical bench.

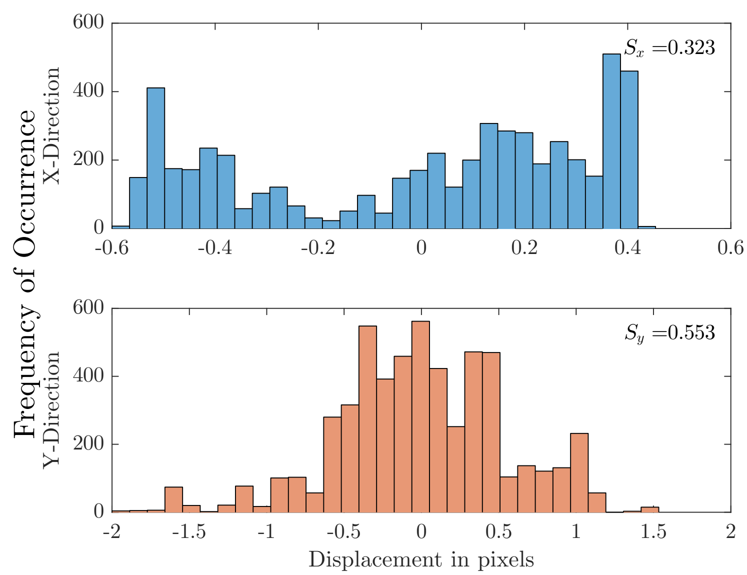

Figure 3.4. First Optical Bench - Centroid Histograms. Top histogram corresponds to the X-Direction displacements, while the bottom to the Y-Direction. S_x and S_y are the standard deviations for each set of data, in pixels.

To characterize the non-linear behavior of the screen, a ramp image containing pixels ranging from 0 to 255 DN[3] is displayed on the screen. This ramp is a grid of non-adjacent pixels where the value of the pixels increase linearly. In figure 3.5, the 0 DN pixel is located at the top right, and the 250 DN is located on the bottom left. The last five pixels at the bottom are the values from 251 to 255.

[3]DN refers to Digital Number, equivalent to “counts”. Here this term is used indistinctly.

Figure 3.5. Screen Ramp observed with the detector.

Figure 3.5 is an average of roughly 300 images with the background subtracted in order to minimize the noise added by the variations of the pixel's intensity on the screen. The illuminated pixels in the image are isolated and the average of the 4 brightest pixels is calculated. This value is stored and tagged according to the DN counts that it represents. It can be observed that the intensity grows non-linearly until the $\sim$100DN on the screen and then it saturates. The first 100 data points are taken and used for a curve fitting, using a three degree polynomial. Figure 3.6 shows the obtained results. The fitted polynomial used is

$$f(x) = 1.291 \times 10^{-4}x^3 + 1.759 \times 10^{-2}x^2 + 1.438x + 6.534 \qquad (3.2)$$

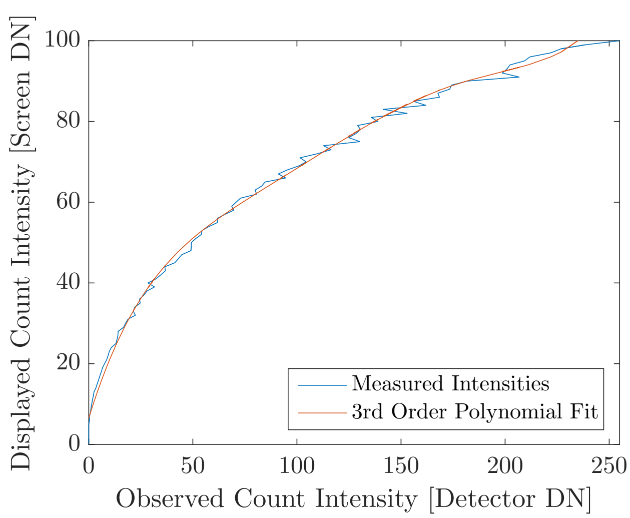

Figure 3.6. Non-linearity polynomial fit calibration.

The fitted polynomial reduces the depth of intensity values from 255 values to 100. Nonetheless, only through the correction of the non-linear effect of the screen can the correct density profile of the sodium layer be displayed on the screen and observed by the detector.

To simulate the sodium profiles, the method described in (Mello et al., 2014) is emulated. This method uses data collected by the LIDAR facility of the LZT (Pfrommer & Hickson, 2010), fitting five Gaussian functions for each profile, each one with three parameters. By taking statistics on each parameter of these Gaussian functions, these parameters can be treated as random variables and used to generate "synthetic" sodium profiles. An example of these synthetic sodium profiles is displayed in figure 3.7.

$$g(x) = ae^{-(x-b)^2/c^2} \tag{3.3}$$

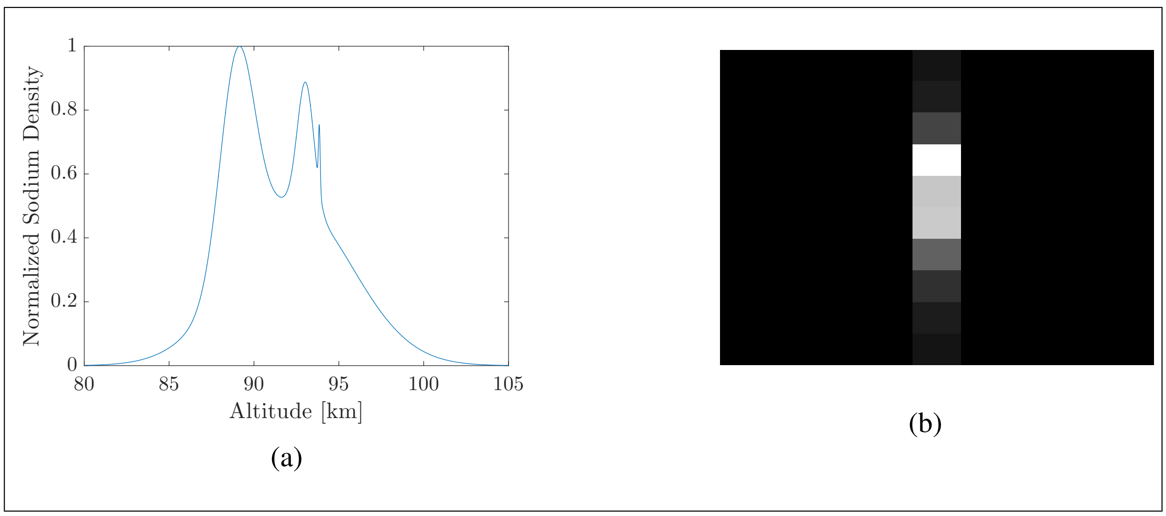

Figure 3.7. (a) Synthetic sodium layer example. (b) Sodium profile sampled in 10 pixels to be displayed on the screen.

The synthetic profile is then sampled to match the desired angular size and sampling according to table 3.4, considering also the size of the pixel on the screen. After re-scaling the intensity with the 3rd order polynomial, it is projected onto the screen and fed into the optical path.

3.1.3. Phase-Screen Control System

The phase screen is an acrylic plate that has received a surface treatment. This treatment produces an optical path difference in the wave-front similar to the optical path difference that is produced by the atmosphere, only scaled down. Because it is a static element and in order to obtain multiple frames with different atmospheres, the PS needs to be moved between frames.

For this to occur, the PS is placed over a cart that moves over a trail using a stepper motor and a threaded rod connected to its rotational axis. The threaded rod is screwed through a threaded hole in the cart, so as the stepper rotates, the rod does it too, and the cart moves. The characteristics of the stepper motor are listed in table 3.5. The threaded rod has an M8 thread, with a nominal pitch of 1.25mm, which can be related to the step of the motor by 1.25mm/200steps, or 6.25μm/step.

Table 3.5. Stepper Motor main characteristics

Characteristics	**Value**
Model	Mercury Motor SM-42
Angular Step	$1.8° \pm 5\%$
Steps per turn	200
Voltage	12 [V]
Current	0.33 [A]

To control the motor, an EASYDRIVER stepper motor driver board is used. An Arduino Uno board is utilized to generate a PWM that commands the driver board when to move the motor and its rotation rate as well as the direction of motion. The Arduino receives the number of steps to move and the rotational direction as instructions from MATLAB via the serial port. Based on these instructions the arduino board generates the PWM and direction signals for the motor.

3.1.4. Control Cycle and Acquisition System

The acquisition process is automated and controlled completely through MATLAB utilizing a desktop computer with remote access. The cycle is composed of the following steps:

- The motor moves and the PS is located in some position of the optical path.
- Three different types of images are then acquired with the CCD
  - (i) Dark Image
  - (ii) Single illuminated pixel Image (also called Spot Image)
  - (iii) A series of successive randomly generated sodium profiles (also called Profile Images or Elongated Spots)
- Repeat the process

Each time the operation performs a cycle it is called an iteration. For each iteration, the Spot Image acquired is unique for the entire set of Profile Images and is used to obtain the real centroid for that position of the phase screen, as if it were the centroid of a natural guide star.

Once the cycle starts again, the system uses the same set of sodium profiles in all the iterations (this is for saving the profiles used without generating excessive data).

3.2. ANN Training, Validation and Results

The ANN training and validation was performed by Amokrane Berdja, PhD. Here it is a summary of the procedure and the obtained results, but a more complete description of the research can be found in (Berdja et al., 2016).

As was described at the Introduction of this document, the training of the ANN aims to calculate the centroids of the elongated laser guide star observed by a SH-WFS, which are affected by the optical turbulence and the sodium layer profile simultaneously. For this case the ANN type is a multilayer feed-forward neural network with nonlinear transfer functions at each node, with supervised back-propagation learning. This means that during the training process the ANN is repeatedly fed with sets of input and output data "pairs". For each set, the network progressively updates the weights to minimize an error merit function, which is based on the difference between the output data presented to it and the output of the ANN itself. If there is a distinctive relationship between the input and output data, the weights will converge.

Two types of architecture were considered. The first one receives the elongated spot images as input and the centroid pair as output. The second architecture receives the elongated spot images and density profile as input (as in figure 3.7b) simultaneously and the centroid pair as output. The first architecture is elaborated to understand if the images contain sufficient information regarding the sodium layer itself in order to isolate it from the effect of the optical turbulence, and then compute the correspondent centroid. The second it used to understand whether the knowledge of the network of the sodium layer profile produces an improvement in the centroid calculation, which in application would mean that a real-time profiling would be needed parallel to the AO system.

Since the list of centroids presents a correlation between one another, according to the phase-screen pattern, and as a result, the same position of the phase screen is used to acquire multiple sodium profiles, the triples of data need to be shuffled randomly.

25000 triples of data were prepared for the ANN process, where 24750 are used for training while the rest are used for the validation process. This proportion might appear odd considering than in general the volume of data used for each process is more comparable between each other[4]. But, considering that the total volume of data is very limited, it was decided arbitrarily the training process had the priority on date usage so the proportion used is actually 99% and 1% for training and validating, respectively.

During the initial stage of the process, it is unknown how many hidden layers and nodes the ANN needs to contain in order to ensure an acceptable performance. It was decided that a single hidden layer was enough to ensure the convergence of the ANN, and after a few tests for several different nodes concluded that 11 nodes for the first architecture

[4]A common rule is the $2/3$ for training and $1/3$ for validating, even though other proportions are used depending on the application and training methods.

and 13 nodes for the second would be optimal. The output centroids obtained through the ANN are expected to be linear to the real centroid. Therefore, a scatter linear regression with dispersion can be elaborated to use the slope as merit figure to diagnose the ANN efficiency. Nonetheless, if the slope is not equal to 1, the slope can be "manipulated" by scaling the output data. However, a more suitable merit figure to understand the performance of the ANN is a correlation coefficient. Table 3.6 displays the resulting values for the merit figures mentioned above, where m_x and m_y represents the slope for the linear regression and r_x and r_y represents the Pearson product-moment correlation coefficients, for the X and Y direction respectively.

Table 3.6. ANN efficiency merit figures. m_x and m_y are the slopes and r_x and r_y are the Pearson product-moment correlation coefficients for the linear regression of the centroids in the X and Y direction respectively.

	Architecture 1	**Architecture 2**
m_x	0.9	0.93
m_y	0.8	0.83
r_x	0.97	0.97
r_y	0.87	0.88

Figure 3.8 is a short sample of the centroids used to validate the ANN performance, where the real centroids are in purple and the centroids computed by the second architecture of ANN are in black.

3.3. Second Laboratory Simulation Bench

As previously mentioned, even though the results obtained with this first setup were adequate and provide proof to support the hypothesis, the optical system does not completely reproduce the desired phenomena of angular anisoplanatism. When the real system is implemented and an elongated spot is displayed in the screen, it can be noticed that the anisoplanatism is almost null. Due to this reasoning, a second bench was designed to

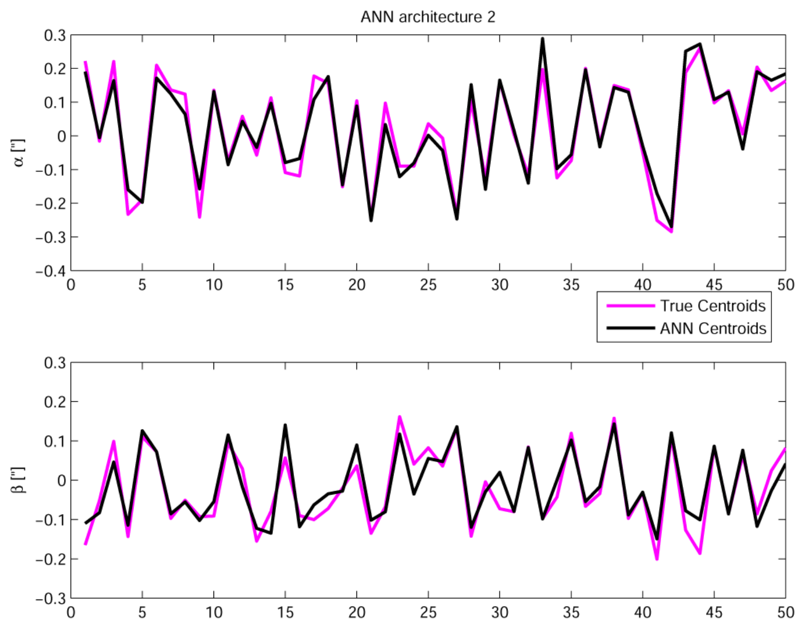

Figure 3.8. a short sample of the centroids used to validate the ANN performance of the second architecture, where the real centroids are in purple and the centroids computed by the second architecture ANN are in black. α and β denote centroids in the horizontal and vertical directions. Figure taken from (Berdja et al., 2016).

obtain data with a higher influence of this phenomena. To implement this second bench, improvements have been required in some of the modules of the first bench.

3.3.1. Second Optical Design

When observing a vertical or horizontal line with the first bench, the separation between pixels was noticeable. This was observed due to the shape of the pixels and distribution on the screen, the size of the pixels and the de-magnification. From a data perspective, the separation between pixels adds a noise with a specific frequency that can affect the ANN training process. However, this noise pattern is eliminated after the binning process. In order to decrease the presence of this pattern a lower magnification is desired.

A lower de-magnification requires higher distances along the bench all the while using the old optical components (a relay of two convex lenses). The original plan was to utilize a concave lens to reduce the distances in the bench, by trading the acquisition of less light. To compensate this last issue, an increase of the exposure time was needed for each image acquired.

The design of this second optical bench was limited by the available optical components in the laboratory. To reproduce the first part of the relay, two concave lenses are used consecutively. To reproduce the desired de-magnification, a second lens that focuses the image would require a distance higher than the length of the bench. To avoid this, a collimator lens is used, followed by a beam splitter acting as a folded mirror. To avoid the aberrations added by the collimator lens, an identical lens is placed in the opposite direction as part of the focusing system. Finally, a focusing lens is placed to form the image of the screen over the camera.

The new optical design is displayed in figure 3.9 as well as the optical characteristics in table 3.7.

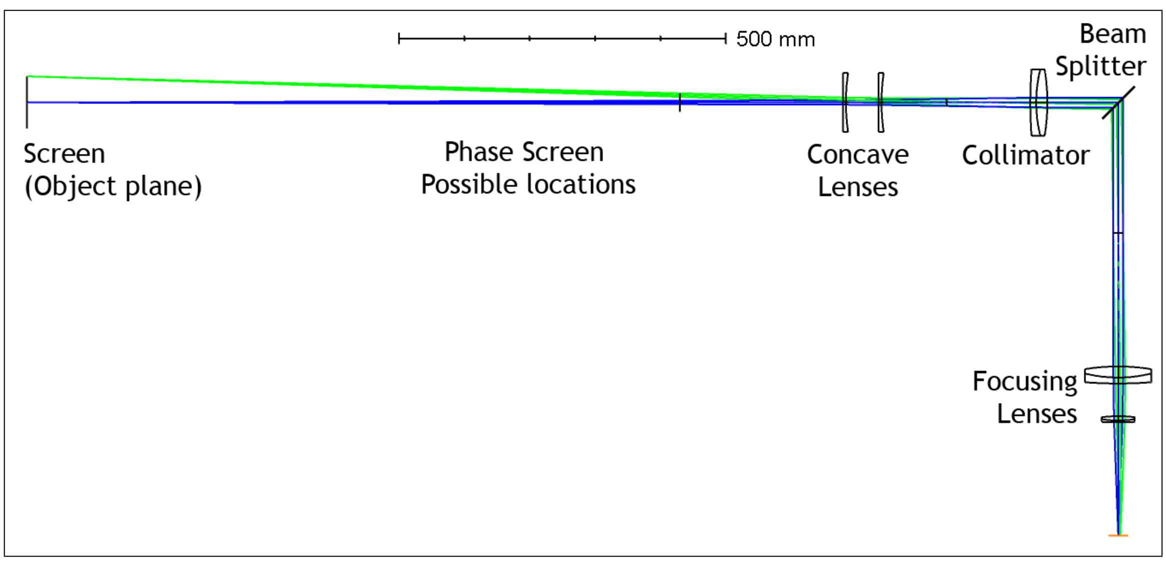

Figure 3.9. Second Optical Bench Layout

This setup has been designed to try to achieve a magnification of 1/15, but because there are multiple lenses and some of them are not thin enough to be represented by

Table 3.7. Smart Centroid second design optical specifications.

Component and surface	Radius of Curvature [mm]	Thickness [mm] (to next surface)	Glass Material	Semi-Diameter [mm]
LGS	Infinity	1,000.00		40.00
Turbulence	Infinity	249.75		14.06
Ross LPCC 388	Infinity	4.50	BK7	45.00
Ross LPCC 388	312.50	50.00		45.00
Ross LPCC 388	Infinity	4.50	BK7	45.00
Ross LPCC 388	312.00	228.00		45.00
Collimator	677.22	9.11	SF2	50.80
Collimator	211.15	17.00	BK7	50.80
Collimator	-309.33	108.50		50.80
MIRROR	Infinity	200.00		35.35
PUPIL	Infinity	204.00		7.50
FOCUS1	309.33	17.00	BK7	50.80
FOCUS1	-211.15	9.11	SF2	50.80
FOCUS1	-677.22	50.00		50.80
AC508-300-B	201.80	6.60	N-LAK22	25.40
AC508-300-B	-161.50	2.60	N-SF6HT	25.40
AC508-300-B	-760.00	173.43		25.40
Detector Focal Plane	Infinity	–		–

paraxial approximations, this value cannot be calculated theoretically. Using ZEMAX, the obtained magnification factor is approximately $\sim$14.3. The PS is located between the screen and the first concave lens, and because the pupil has been set at 15mm in the collimated space, the projection into the PS generates a meta-pupil of approximately 4μm. In figure 3.9, it is possible to observe that for different directions on the screen, the traversed PS can be even completely different, which is in fact observed with anisoplanatism.

Equivalent to the first design, a characterization of the pitch observed by the camera and the long exposure PSF is needed. After displaying a grid of dots evenly separated along in the screen, the average distance between adjacent pixels was calculated as ~3.56 pixels. After averaging images while observing different portions of turbulence, the FWHM of the long exposure PSF was calculated as ~ 7.5 pixels. The same process can be implemented here to obtain the different plate scales.

A picture of the optical setup implemented in the laboratory can be observed in figure 3.10.

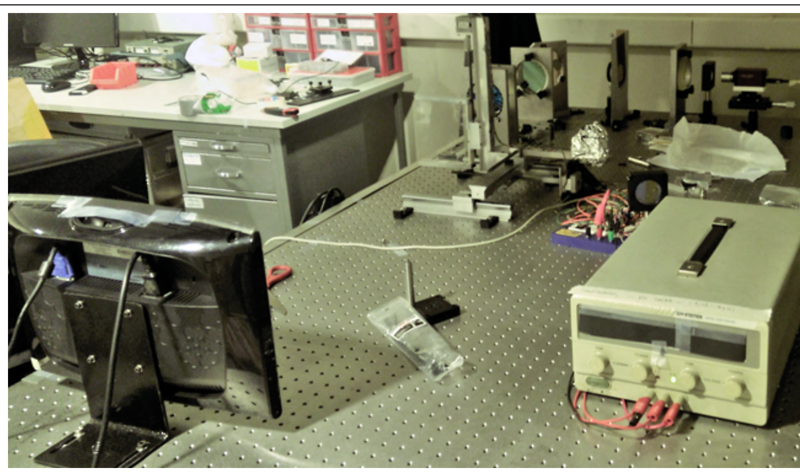

Figure 3.10. Second Optical Bench - In Laboratory Picture.

3.3.2. Modifications to the Phase-Screen Control

The first implementation of the motor control module was elaborated using Arduino libraries for the pin management, thus generating the PWM and the direction signals. Two problems arise when using these libraries: multiple pins cannot be set simultaneously and delay propagation issues.

Arduino functions for pin management implement several ticks from the microcontroller, and the amount of ticks is not constant over time. When MATLAB commands the motor to move multiple steps, these ticks result in longer iterations which ends in a longer cycle as well. This would increase when using multiple motors.

Also, because the required ticks by the functions is not constant, a delay propagation is produced in the PWM, resulting in a wave that is not constant in frequency nor duty cycle. This results in a motor rotation rate that is not constant, producing a sort of “chattering” when the PS is moving.

Another aspect from the first implementation is that the serial communication with MATLAB considered a menu with options that were useful to control the motors using a Serial Monitor but not very useful for automating the cycle. Sorting through the menus resulted in a longer duration of cycle.

All these aspects were improved in the second implementation for the phase-screen control. Arduino libraries were not used for the pin management, but direct port manipulation in the registers of the micro-controller[5]. All pins from a single register can be controlled simultaneously with this method, changing the whole register value to a digital word in 4 ticks of the clock (which remains constant). In this case, each I/O register has 8 pins, so a 8 bits word it is assigned. For this case, because only three motors are used, three PWM can be generated using the same register so they can move simultaneously, with no added delays.

The change is done directly into the port without using extra ticks executing functions, so the delay problems generated in the previous implementation are none or totally negligible, eliminating the chatter effects.

3.4. System Characterization and Limitations

As previously mentioned, using two identical lenses to create and refocus the collimated space nearly cancels out the optical aberrations added by these two components. A similar behavior occurs between the two concave lenses at the entrance of the optical trail

[5] The micro-controller in Arduino Uno board is an Atmega328p model.

and the last biconvex component. The last lens has a relatively small focal distance related to the large curvature of its first surface and the total thickness of the component. This type of optical element usually has a high spherical aberration and a notorious curvature of the focal plane. In this case, most of these aberrations are canceled out with the two convex lenses, given the similar aberrations that are generated by these two lenses but in the opposite direction.

Figure 3.11 shows the Spot Diagram for three different fields of the optical system, located in the optical axis at 0mm on the screen, at 25mm and at 40mm. The black circumference represents the Airy Disk, or limit of resolution by diffraction, which has a diameter around 20μm. Taking this into consideration, it is clear that the aberrations of the optical system are almost null.

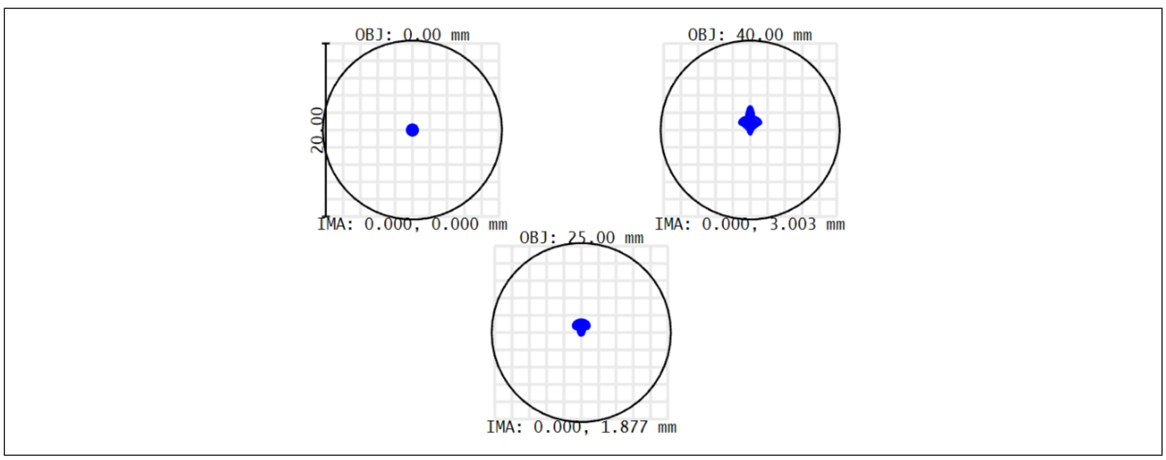

Figure 3.11. Second Optical Bench Spot Diagram.

Using the same grid of dots as the one observed in figure 3.5 to measure the distance between pixels, the system de-magnification in the bench is calculated as 1/12.74 and not 1/14.3 as measured through ZEMAX. This is still acceptable, considering that the pixel size is 5.6μm and the pitch between pixels is 254μm.

As was pointed out before, due to the first two concave lenses the cone of light at the entrance of the optical trail is quite narrow. Therefore, the amount of light entering into the system is very low. In order to overcome this situation, a higher exposure time has to be implemented in the image acquisition. For the first optical bench, the exposure time for the acquired data was around 25ms, while for this new setup it was between 1–3 seconds, which resulted in images with higher background noise due to the integration of dark current.

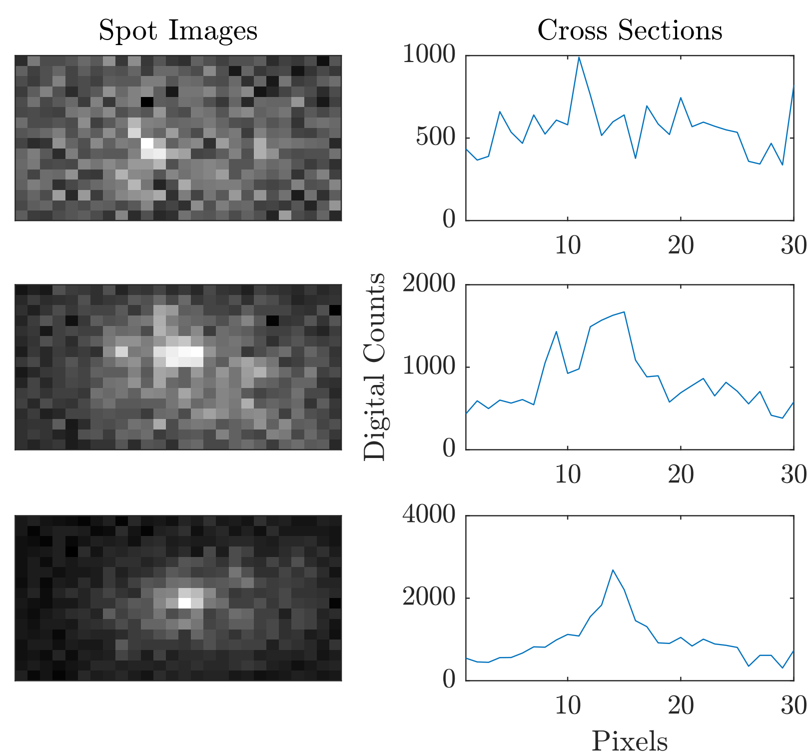

Figure 3.12. Second Optical Design - First Calibration Data. Plots on the right correspond to cross sections of the brightest row in the images of the left side. Top two images represent some of the most common cases, while the bottom images correspond to the highest SNR.

Figure 3.12 shows some examples of the images acquired, where the level of high noise can be observed. Figure 3.13 displays the SNR[6] calculated for the first batch of 460 images used for calibration purposes.

[6]SNR was calculated as the ratio between the average of the 4 brightest pixels around the center of gravity, and the average floor noise.

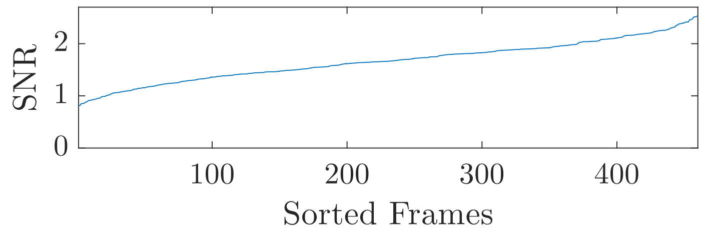

Figure 3.13. Second Optical Design - First Calibration Data Signal to Noise ratio.

Given the low SNR in the data, compared to the data obtained in the first experiment, a post-processing was implemented. For a single position of the PS, successive images are acquired by observing a dark screen, averaged and labeled as DARKS. Also, successive images with a single illuminated pixel are acquired as well, averaged and labeled as SPOTS. Then, the corresponding DARK frame is subtracted from the SPOT frame, and the result is then divided by a MASTER FLAT image obtained and prepared at the beginning of the whole cycle. This MASTER FLAT is the average of successive images with the screen fully illuminated with the turbulence removed from the optical path and normalized so as not to excessively affect the real intensity of the resulting data frames. This process is used to remove major intensity differences in the image field produced by optical vignetting, dirt in the optics, irregular illumination patterns on the screen or its pixels, and the difference in sensitivity in the detector pixels.

After implementing the image processing mentioned above, a second batch of images is taken. The improvement in the SNR can be observed by comparing figures 3.12 and 3.14. However, other aspects of the acquired data have to be studied to ensure the quality needed to train the ANN with am acceptable level of performance.

Statistics on the second batch of data are taken to characterize the centroid displacements. This must be done for all types of calibration images, even the DARK frames. It was not mentioned before, but the screen is not capable of achieving a true black state, equivalent to emitting no light when 0 counts are selected from the computer. The screen

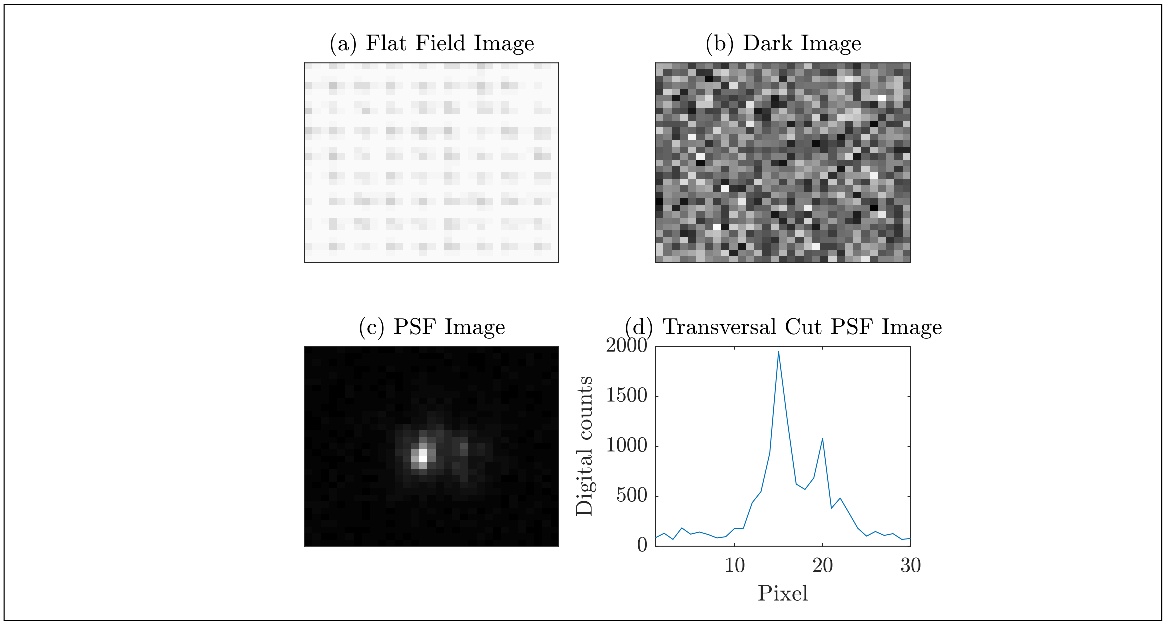

Figure 3.14. Second Optical Design - Second Calibration Data. Top left image correspond to the MASTERFLAT, top right to a Dark frame, and bottom images corresponds to a single SPOT frame and its horizontal cross section in the row that contains the maximum.

has a minimum bias level that generates a dim background light, which is enough to generate a considerable amount of electrons observed by the detector. As a result, for each position of the turbulence the DARK frame contains information regarding the turbulence. Nonetheless, because of the other noisy factors in the image acquisition, such as the dark current, this information cannot be independently discriminated.

Far beyond signifies that all the centroid measurements can be polluted by the background noise generated by the screen. This generates an uncertainty error in the measurements that would propagate through the ANN training, resulting in a lower performance.

Theoretically, this uncertainty can be removed by subtracting each DARK frame from the respective SPOT frame, if these uncertainties only add each other in quadrature or orthogonally between each other [7].

[7] This assumption is fairly reasonable, but needs to be proven in the future. This proof is not elaborated here because it exists as a parallel task to the current work covered.

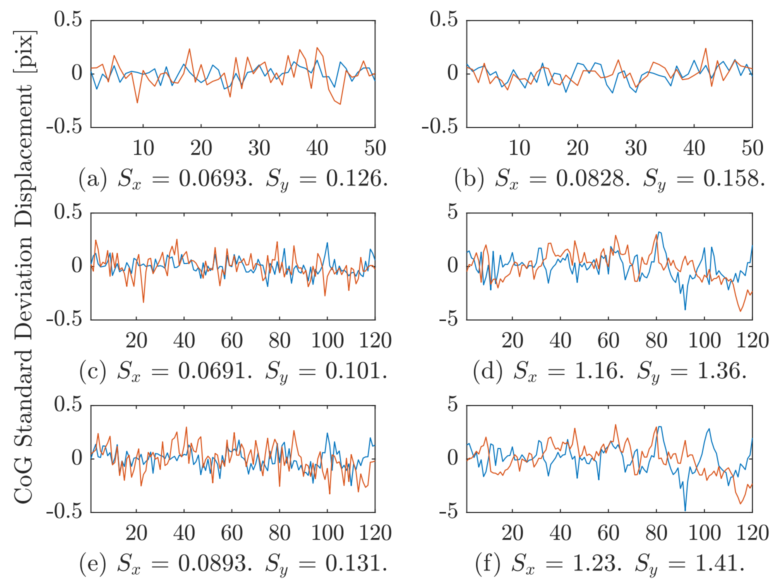

Figure 3.15. Second Optical Design - Second Calibration Data Statistics. Center of Gravity (CoG) displacements for (a)DARK frame, (b) Single illuminated pixel frame with static turbulence, (c) Raw data for a single illuminated pixel but a different turbulence position for each frame, (d) Same raw data of (c) but with a threshold of 30% of the spot maximum value, (e) Same raw data of (c) with the background subtracted and divided with a master flat, (f) Same raw data of (c) with (d) and (e) procedures applied simultaneously. For each plot, the blue curve represents the data in the X direction and the red curve the Y direction.

Figure 3.15 displays the results for the data taken. For each plot, the blue curve represents the centroid displacements in the X direction, while the red curve represents the displacements in the Y direction. Parameters S_x and S_y are the standard deviation of the centroid displacements in each direction. The top two plots, (a) and (b), are the "static measurements"; (a) represents the centroid displacement measurement for the DARK frames, where no illumination is present except by the background light, while (b) considers a single illuminated pixel in the screen and the turbulence located in a static position. The frames with a single illuminated pixel present more displacement than the dark frames, most likely as a result of two factors. The first one, and most likely of lesser importance, is the Photon Shot Noise (Janesick, 2007). This noise is related to the uncertainty principle of light and its quantum nature. In the case of a high flux of photons source such a LED light, its behavior can be modeled as a Poisson process of parameter λ equivalent to the flux of light. The second factor, and probably the most relevant, deals with the fluctuations on light emission that the illuminated pixel possesses. If this flux is not constant and stable throughout all the traversable solid angle, small amounts of light will interact more or less with certain parts of the PS, which will result in variations of intensity in the *speckles* formed, and therefore, in the centroid measured. The standard deviation in both types of frames are similar in magnitude, which is to be expected considering that they both represent static cases.

Plots (c), (d), (e) and (f) correspond to the measurement of centroids for a single illuminated pixel but with PS moving. Plot (c) represents the measurement of the centroid for the raw data acquired, while plot (e) is the measure for the post-processed data (i.e. data subtracted and divided by the MASTERFLAT. Plots (d) and (f) are the same as (c) and (e) respectively but with a threshold applied. This threshold only considers the pixels that are at least a 30% of the peak of the spot.

A few things can be highlighted while observing these graphs:

- In all the cases the Y displacement is higher than the X (by comparing each S_x and S_y values). This effect is probably produced by the shape of the pixel, which is rectangular with a longer vertical side.
- The standard deviation for the raw data ($S_x = 0.0693$ and $S_y = 0.126$) is fairly similar to the DARK frames($S_x = 0.0691$ and $S_y = 0.101$) and the frames with static turbulence ($S_x = 0.0828$ and $S_y = 0.0788$). This means that when considering the full frame of raw data (images of 80×80 pixels), the displacement of the measured centroid cannot be distinguished from the uncertainty propagation by the background noise. If this data were to be used to train the ANN, the training process would be more difficult because the ANN would have to learn to cope with the background noise. Therefore, if the ANN is successfully trained its performance may produce a rather low result.

- The curves with and without the background ((c) and (e), (d) and (f)) are not entirely identical in shape, which in turn increases the relevancy of the background noise as one of the most detrimental characteristics of these images.
- Comparing plots (d) with (c) and (f) with (e), and each respective standard deviation, it is possible to notice that using a threshold increases the center of gravity displacement by more than 10 times. This process can be a little “controversial”. From one perspective, it makes sense to consider that taking the brightest parts of the image results in a fair representation of the real centroid of the image, and therefore, of the wave-front slope, in turn eliminating the background noise that propagates an uncertainty that cannot be neglected. Taking into account a geometrical analogy, if we consider the center of gravity between a heavy body and a very light body, small changes of the mass in the lightest one will be less perceptible overall because of the inertia that adds the heaviest one. Eliminating the heaviest body provides an increase in the sensitivity with which the center of gravity displacements are measured. Nonetheless, this argument is entirely based on the premise that the background noise does not return significant information about the slope.
- Considering the last observation, the threshold value has to be studied with more detail in order to understand what value should be put on the trade-off between noise rejection and tail of the “bell” and an increase in the slope accuracy calculation. In general, it is usually considered that the tail of the spots in a SH-WFS possesses an adequate amount of information regarding the sub-aperture slope. In some slope calculations, only the intensity on the borders of the sub-aperture is used rather than the complete image (Hardy, 1998). Arbitrarily in this situation a threshold of 30% has been established, but a different threshold value could produce better results; however, improper study can lead to an uncertainty propagation, which has the potential to decrease the accuracy of the measured slope.

Figure 3.16 displays the histograms for the cases mentioned in the previous paragraphs: X and Y displacements for the Raw Data and for the Post-Processed data. These

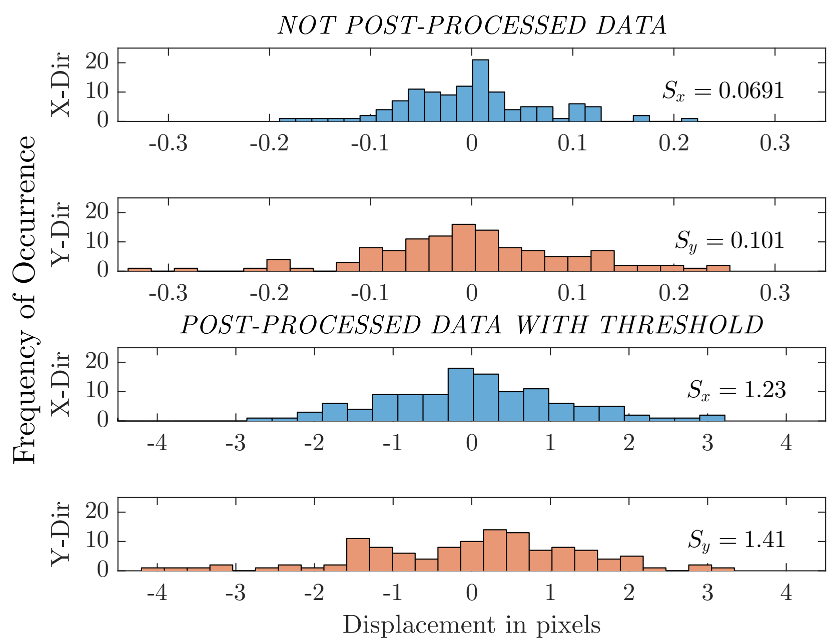

Figure 3.16. Second Optical Design - Second Calibration Data. Histograms of the centroid displacements in X and Y direction for the raw data against “the post-processed”.

histograms demonstrate another anomaly present in the optical bench. Given the statistics of Kolmogorov for the turbulence and the statistics that the manufacturer of the PS attempts to replicate, it would be expected to observe a normal distribution in the histogram with statistical parameters related to the PS/Turbulence parameters (such as r_0). However, roughly two normal distributions can be observed in some of the plots. Even though this issue has not been fully addressed with more detailed experimentation, this phenomenon has been associated with the mechanical structure that supports the phase screen. When the rods rotate, a small oscillation can be observed in the mechanical structure, which is transmitted to the PS orientation. This results in a small tip-tilt in the acrylic plate. The tip-tilt has a continuous and possibly periodic oscillation that has the potential to scatter the data into two different Gaussian curves.

The final analysis of the acquired data corresponds to a “stripes” pattern, barely observable with the high contrast between the spot maximum and the background, as well

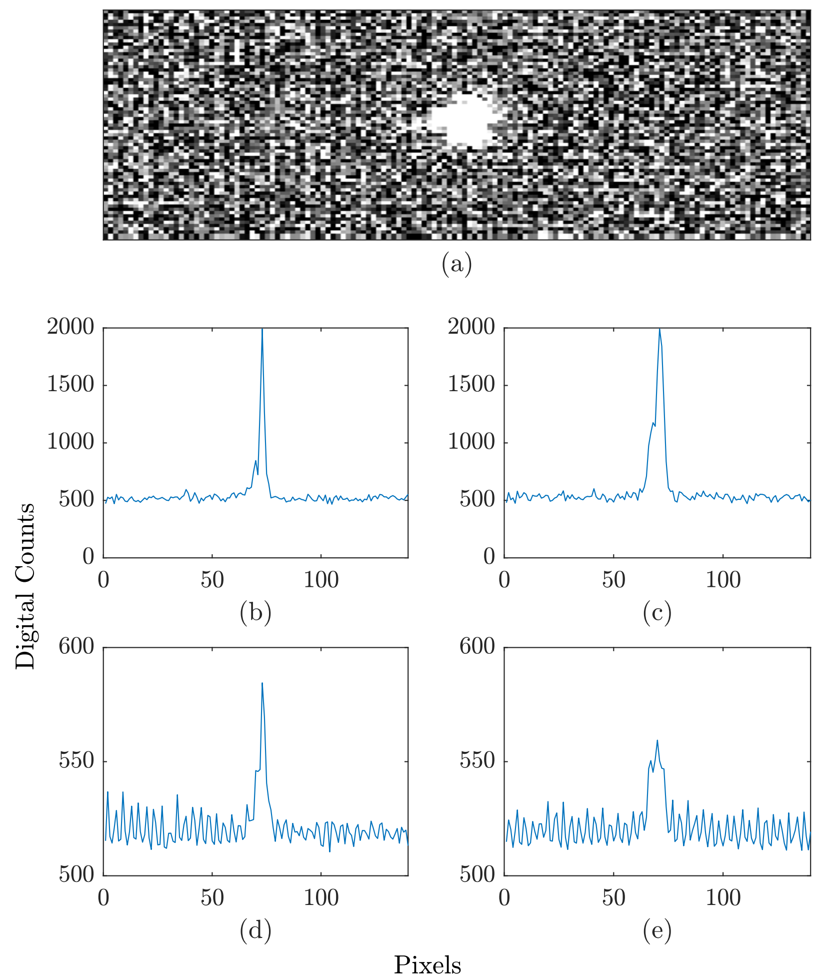

Figure 3.17. Second Optical Design - Second Calibration Data. Analysis in the striped pattern present in the images. (a) Shows an image with a range of counts between 500 and 550 DN to see the pattern. (b) and (c) show a cross section of the image crossing the maximum in X and Y direction. Plots (d) and (e) are the vertical and horizontal mean respectively of the image, where the noisy pattern can be observed with more detail.

as with the present background noise. Figure 3.17 displays one of these cases: In (a) the chosen image displays with a range of counts between 500 and 550 DN, in order to observe part of the pattern. In (b) and (c), a side view of the image can be observed, and in (d) and (e), a sum of all the columns and all the rows produces features associated with the stripes pattern. When adding uncorrelated noise, the resulting noise decreases overall. However, in this case the noise increases as a result of the existing correlation in the stripes pattern. This occurs in both directions. In the noisy pattern, the distance observed between successive peaks or successive valleys goes between 3 and 4 pixels, which correlates with the distance between adjacent screen pixels in the screen ($\sim$3.56 pix) measured at the beginning of the second optical design section.

3.5. Comments about the problems, Possible Solutions and Further Work

The second bench completely fulfills the necessary requirements to reproduce more realistic phenomena for the acquisition of images with a SH WFS using laser guide stars. Nonetheless, the quality of the data retrieved is very low compared to the first laboratory bench.

The statistical behavior observed in the centroid displacement, although not ideal, is not detrimental. The effects of having centroid displacements without the statistical behavior of a Gaussian distribution, as in the presented data, would result an ANN that is less favorable for central displacement cases. Therefore, the validation of the ANN should be lower when facing such cases. However, because the problem appears to arise from a mechanical source, it can be repaired without severe delays and a low investment of time and monetary resources.

The other effects observed are a result of the technical limitations mainly produced by the Monitor Screen and the Phase-Screen. These two components represent the bottleneck preventing advancements towards a better version of this experiment.

Even though the monitor possesses a grid of pixels with an average pitch of 254μm, the physical structure of the pixel has smaller details. To remove these artifacts through a binning process, like in the first bench, a more aggressive sampling is required. This can be achieved by either changing the monitor for a monochromatic one that has a smoother transition between pixels or by slightly tweaking the optical design, although this method is not entirely recommended considering the optical advantages of the current one. Utilizing a different monitor with a higher contrast, brightness and some sort of true zero value may be a fair consideration as well.

Other methods that reproduce the elongated guide star can be revisited as well as some chemical companies might be able to place a fluorescent ink inside a test tube with statistics similar to the sodium layer profile. Current testing is being conducted in Durham University for Dragon (González-Gutiérrez et al., 2017).

In regards to the turbulence, it is mandatory to perform a characterization of the PS in order to identify if the statistical problems are related to the PS structure or another source. It is also necessary to understand if the PS fulfills a statistical Kolmogorov behavior and to obtain its real atmospheric turbulence parameters, such as r_0. Although the likelihood of acquiring a new PS is fairly low due to how expensive they are, a new one with a smaller r_0 (from equations 1.8 and 2.3) and a more suitable inertial range for the pupil could generate a wider long exposure PSF, which is the result of a more dynamic centroid displacement.

A review of these points is a key element in the training process of the ANN in the current state of the experiment, in order to minimize any uncertainties that could potentially propagate within the ANN.

3.6. Smart Centroids: Technical Summary

Two optical benches were designed and implemented in a laboratory to acquire the desired data, including the optical design, and the control and acquisition systems for each respective design. The first bench was capable of reproducing some atmospheric effects, such as the anisoplanatic effect, but that in practicality were negligible. The second design fulfilled the turbulence requirements and presented a significant variety of atmospheric conditions. Nonetheless, after a characterization using calibration data from both benches, the first design presented data more suitable for the ANN training process.

In regards to the first bench, the acquired data presented a distinguishable centroid displacement given by the PS from the background noise. The X component presented a standard deviation around 0.32 pixels and for the Y component showed results around 0.55 pixels. Also, the SNR from the data ranged between 5 and 13. In the case of the second bench, the centroid displacement presented a standard deviation around 0.1 pixels or below, which was indistinguishable compared to the uncertainty given by the background noise of the data. Only through the use of a threshold could the displacements present a standard deviation over 1 pixel, which in turn conditioned the relationship between the measured centroid and the real slope of the wave-front. It is crucial to mention that the SNR in this case maintained a range almost entirely between 1 and 2. Additionally, after a more detailed analysis of the data, a ripple pattern on the images was observed as a result of the pixel shape on the screen and the small dark separation between adjacent pixels. With these results, a consideration was made regarding the data acquired with the second bench, thus relating its inadequacies for the ANN training, regardless of its improved representation of real phenomena.

Only the data collected from the first bench was used for the ANN training. Two ANN were trained, each with a different architecture. The first one only considered the image observed by the SH-WFS as input and the centroid as output. The second one considered the SH-WFS spot image and the sodium layer profile as well, both as inputs, and the centroid as output. As a merit figure, Pearson product-moment correlation was calculated between the data retrieved by the trained ANN and the real centroids. The coefficients obtained were $r_x = 0.97$ and $r_y = 0.87$ for the X and Y coordinate respectively for the first architecture. For the second architecture, the coefficients resulted $r_x = 0.97$ and $r_x = 0.88$.

The difference in the correlation values between architectures helps to understand the impact of a known profile in real time and its effect on the performance of the network. In this case, there is a small improvement in the performance of the network but this perceived improvement would require an evaluation of cost versus efficiency.

4. CONCLUSIONS

The scientific progress of Astronomy is almost fully dependent on overcoming demanding technical challenges, and the next generation of extremely large telescopes is a clear example of said challenges. Even though many of these problems will require the development of sophisticated technologies and innovative techniques, many of them will also be based on how current problems are solved by the large telescopes that are currently in operation.

This is the case for wide field of view astronomical observations, which require an observation of large regions in the sky with the highest resolution available. This thesis presented two works aiming to fulfill two problems in this area. The first one was part of the development of BOMBOLO, an instrument for wide field of view observations in small scales of time. The second involved the experimental testing of a novel technique using artificial neural networks for the centroid calculation of Laser Guide Stars in Shack-Hartmann wave-front sensors, used in Multi-Object Adaptive Optics.

The first work considered the design of the mechanical structure and opto-mechanical barrels, with the objective that these elements would minimize the optical path difference and the loss of image quality produced by the deformation of the instrument due to a dynamic gravity vector. The design resulted in a structure with mechanical displacements smaller than $\sim 35\mu$m on the camera planes. These values confirm that the mechanical structure and barrels fulfill both the requirements and the hypothesis of this work.

The second work considered the design and implementation of two optical benches, used for the experimental validation of centroid calculation of Laser Guide Stars in Shack-Hartmann wave-front sensors using ANNs. These two optical benches were designed to represent different atmospheric situations, but only one of them was capable of generate the required data for the training and validation process. For this bench, two ANNs were trained. The obtained correlation coefficients between the real data and the output of the ANNs were over 0.97 and 0.87, for the X and Y directions respectively. The hypothesis for this work is not completely fulfilled, considering that the technique was not experimentally proven in all the atmospheric situations. More work is required in order to evaluate this hypothesis in its entirety.

A more detailed technical summary regarding the methodologies and results of these works can be found at the end of each chapter.

These works faced a few issues and came with their own set of challenges regarding the wide field of view astronomical observations, they have also highlighted particular and general aspects where further research would result in significant improvements in this area. For instance, to ensure the best image quality for BOMBOLO, more studies concerning other possible sources of optical path displacements are pending, which is the case with the cryogenic systems. Instruments looking for budget efficiency, as is the case with BOMBOLO, require a deeper understanding of the instrument behavior. For the development of new techniques, such as Smart Centroids, it is fundamental to reproduce the phenomena at an equivalent standard that the technique is aiming to perform. Smart Centroids is a promising technique with great potential, but it still needs a more complete reproduction of the phenomena in order to ensure its capabilities in all scenarios. If this is implemented correctly and a good performance in the artificial neural networks is achieved, the results can lead to the development of future AO systems based on this technique, which is relevant for the next generation of extremely large telescopes.

Many additional problems are continuously arising around the wide field of view astronomical observations, each one with its own difficulties and setbacks. A particularly serious issue involves the restrictive capability of locating the scientific object spectrum in the focal plane of the instruments to simultaneously observe distant objects. Additional examples involve the ability to address a correct model of turbulence for a telescope with apertures larger than the outer scale of the turbulence or the new incoming challenges of wide field of view for multi-messenger astronomy. The solutions for these challenges, among others, will define how the wide field of view astronomical observations will operate in the next couple of decades.

REFERENCES

Angeloni, R., Guzmán, D., Puzia, T., & Infante, L. (2014). Bombolo: a multi-band, wide-field, near uv/optical imager for the soar 4m telescope. In *Revista mexicana de astronomia y astrofisica conference series* (Vol. 44, pp. 206–207).

Assémat, F., Gendron, E., & Hammer, F. (2007). The falcon concept: multi-object adaptive optics and atmospheric tomography for integral field spectroscopy–principles and performance on an 8-m telescope. *Monthly Notices of the Royal Astronomical Society*, *376*(1), 287–312.

Berdja, A., Garcés, E., & Guzmán, C. D. (2016). Experimental results on using artificial neural networks for accurate centroiding in shack-hartmann wavefront sensors with elongated spots. In *Society of photo-optical instrumentation engineers (spie) conference series* (Vol. 9909).

Bruch, A. (1992). Flickering in cataclysmic variables-its properties and origins. *Astronomy and Astrophysics*, *266*, 237–265.

Dhillon, V., Marsh, T., Stevenson, M., Atkinson, D., Kerry, P., Peacocke, P., ... others (2007). Ultracam: an ultrafast, triple-beam ccd camera for high-speed astrophysics. *Monthly Notices of the Royal Astronomical Society*, *378*(3), 825–840.

Fried, D. L. (1965). Statistics of a geometric representation of wavefront distortion. *JOSA*, *55*(11), 1427–1435.

Garcés, E., Guzmán, D., Jones, D., Angeloni, R., & Puzia, T. (2016). Update on bombolo: a 3-arm, wide-field, near-uv/optical imager for the 4-meter soar telescope. In *Spie astronomical telescopes+ instrumentation* (pp. 99084B–99084B).

Gilles, L., & Ellerbroek, B. (2008). Constrained matched filtering for extended dynamic range and improved noise rejection for shack-hartmann wavefront sensing. *Optics letters*, *33*(10), 1159–1161.

González-Gutiérrez, C., Santos, J. D., Martínez-Zarzuela, M., Basden, A. G., Osborn, J., Díaz-Pernas, F. J., & De Cos Juez, F. J. (2017). Comparative study of neural network frameworks for the next generation of adaptive optics systems. *Sensors*, *17*(6), 1263.

Guzmán, D., Angeloni, R., Puzia, T., Jones, D., Jordán, A., Anguita, T., … Garcés, E. (2014). Bombolo: A 3-arms optical imager for soar observatory. In *Proc. of spie vol* (Vol. 9147, pp. 91475V–1).

Guzmán, D., De Cos Juez, F. J., Myers, R., Guesalaga, A., & Lasheras, F. S. (2010). Modeling a mems deformable mirror using non-parametric estimation techniques. *Optics express*, *18*(20), 21356–21369.

Hardy, J. W. (1998). *Adaptive optics for astronomical telescopes* (Vol. 16). Oxford University Press on Demand.

Hecht, E. (1998). Hecht optics. *Addison Wesley*, *997*.

Janesick, J. R. (2007). *Photon transfer*. Orlando, FL: SPIE press San Jose.

Kriege, D., & Berry, R. (1998). The dobsonian telescope. a practical manual for building large aperture telescopes. *The Dobsonian telescope. A practical manual for building large aperture telescopes., by Kriege, D.; Berry, R.. Willmann-Bell, Richmond, VA (USA), 1998, XVII+ 475 p., ISBN 0-943396-55-7,*.

Meeus, J. H. (1991). *Astronomical algorithms*. Willmann-Bell, Incorporated.

Mello, A., Kanaan, A., Guzman, D., & Guesalaga, A. (2014). Artificial neural networks for centroiding elongated spots in shack–hartmann wavefront sensors. *Monthly Notices of the Royal Astronomical Society*, 2781–2790.

Morris, T., Hubert, Z., Myers, R., Gendron, E., Longmore, A., Rousset, G., ... others (2010). Canary: The ngs/lgs moao demonstrator for eagle. In *1st ao4elt conference-adaptive optics for extremely large telescopes* (p. 08003).

Myers, R. M., Hubert, Z., Morris, T. J., Gendron, E., Dipper, N. A., Kellerer, A., ... others (2008). Canary: the on-sky ngs/lgs moao demonstrator for eagle. In *Proc. spie* (Vol. 7015, p. 70150E).

Noll, R. (1976). Zernike polinomials and atmospheric turbulence. *Journal of the Optical Society of America*, *66*(3), 207-211.

Osborn, J., De Cos Juez, F. J., Guzman, D., Butterley, T., Myers, R., Guesalaga, A., & Laine, J. (2012). Using artificial neural networks for open-loop tomography. *Optics express*, *20*(3), 2420–2434.

Osborn, J., Guzman, D., De Cos Juez, F. J., Basden, A., Morris, T., Gendron, E., ... others (2014). Open-loop tomography with artificial neural networks on canary: on-sky results. *Monthly Notices of the Royal Astronomical Society*, *441*(3), 2508–2514.

Parsons, S., Marsh, T., Copperwheat, C., Dhillon, V., Littlefair, S., Hickman, R., ... others (2010). Orbital period variations in eclipsing post-common-envelope binaries. *Monthly Notices of the Royal Astronomical Society*, *407*(4), 2362–2382.

Pfrommer, T., & Hickson, P. (2010). High-resolution lidar observations of mesospheric sodium and implications for adaptive optics. *JOSA A*, *27*(11), A97–A105.

Phelan, D., Ryan, O., & Shearer, A. (2007). *High time resolution astrophysics* (Vol. 351). Springer Science & Business Media.

Roddier, F. (1999). *Adaptive optics in astronomy* (1st ed.). Cambridge, UK: Cambridge University Press.

Sarazin, M., & Tokovinin, A. (2002). The statistics of isoplanatic angle and adaptive optics time constant derived from dimm data. In *European southern observatory conference and workshop proceedings* (Vol. 58, p. 321).

Tokovinin, A., Baumont, S., & Vasquez, J. (2003). Statistics of turbulence profile at cerro tololo. *Monthly Notices of the Royal Astronomical Society*, *340*(1), 52–58.

Tokovinin, A., & Travouillon, T. (2006). Model of optical turbulence profile at cerro pachón. *Monthly Notices of the Royal Astronomical Society*, *365*(4), 1235–1242.

van Dam, M. A., Conan, R., Bouchez, A. H., & Espeland, B. (2011). Aberrations induced by side-projected laser guide stars in laser tomography adaptive optics systems. In *Second international conference on adaptive optics for extremely large telescopes, id* (Vol. 67, p. 67).

Vincent, F. (2003). *Positional astronomy.* `http://star-www.st-and.ac.uk/~fv/webnotes/index.html`. (Accessed: 2015-05)

Wizinowich, P. L., Le Mignant, D., Bouchez, A. H., Campbell, R. D., Chin, J. C., Contos, A. R., . . . others (2006). The wm keck observatory laser guide star adaptive optics system: overview. *Publications of the Astronomical Society of the Pacific*, *118*(840), 297.

Yoder Jr, P. R. (2005). *Opto-mechanical systems design*. CRC press.

APPENDIX

A. FIRST APPENDIX: BOMBOLO OPTICAL SPECIFICATIONS

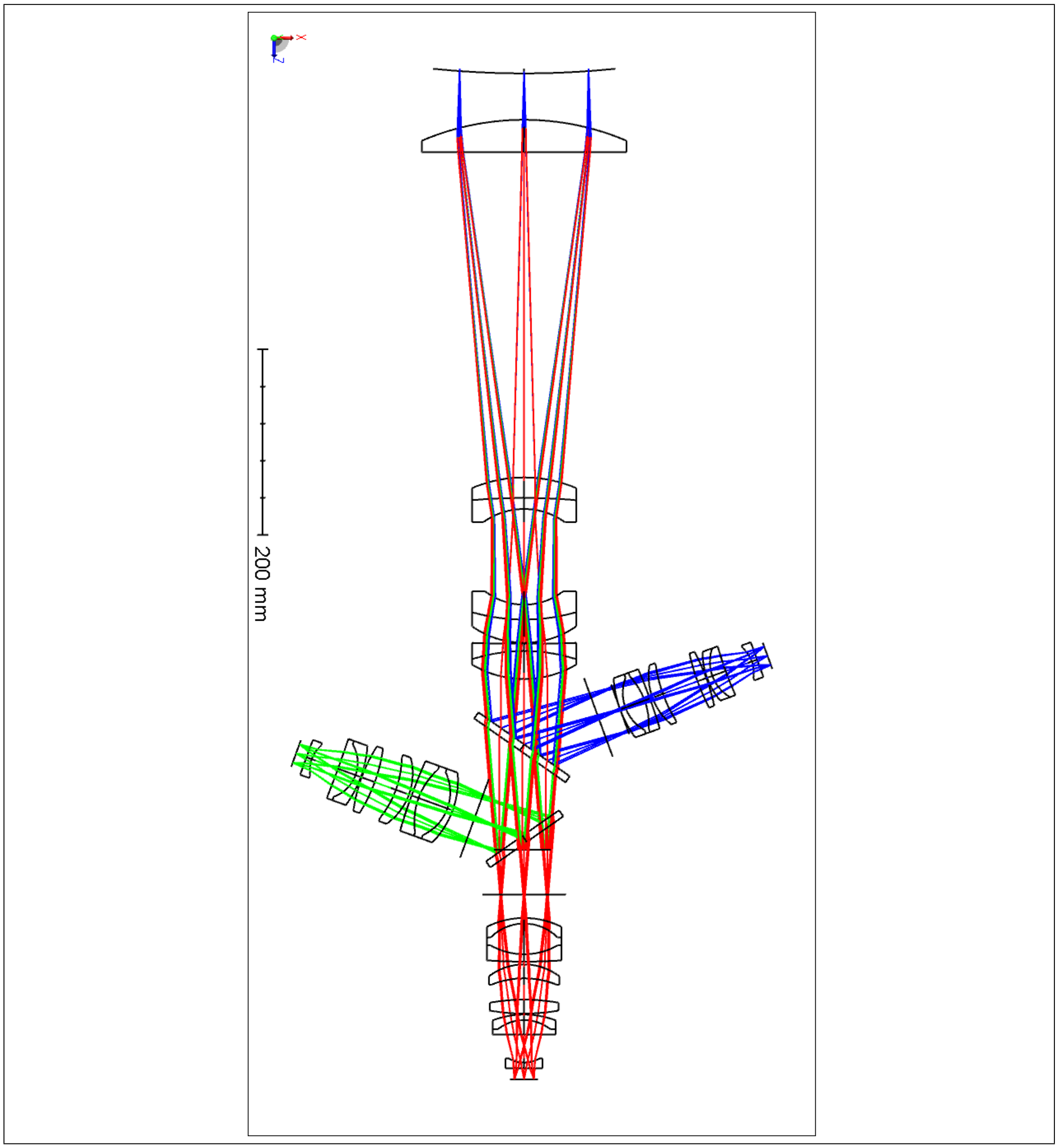

Figure A.1. Zemax image of BOMBOLO's complete optical design. The figure includes the ray tracing, where each color represents the respective channel (blue, green and red).

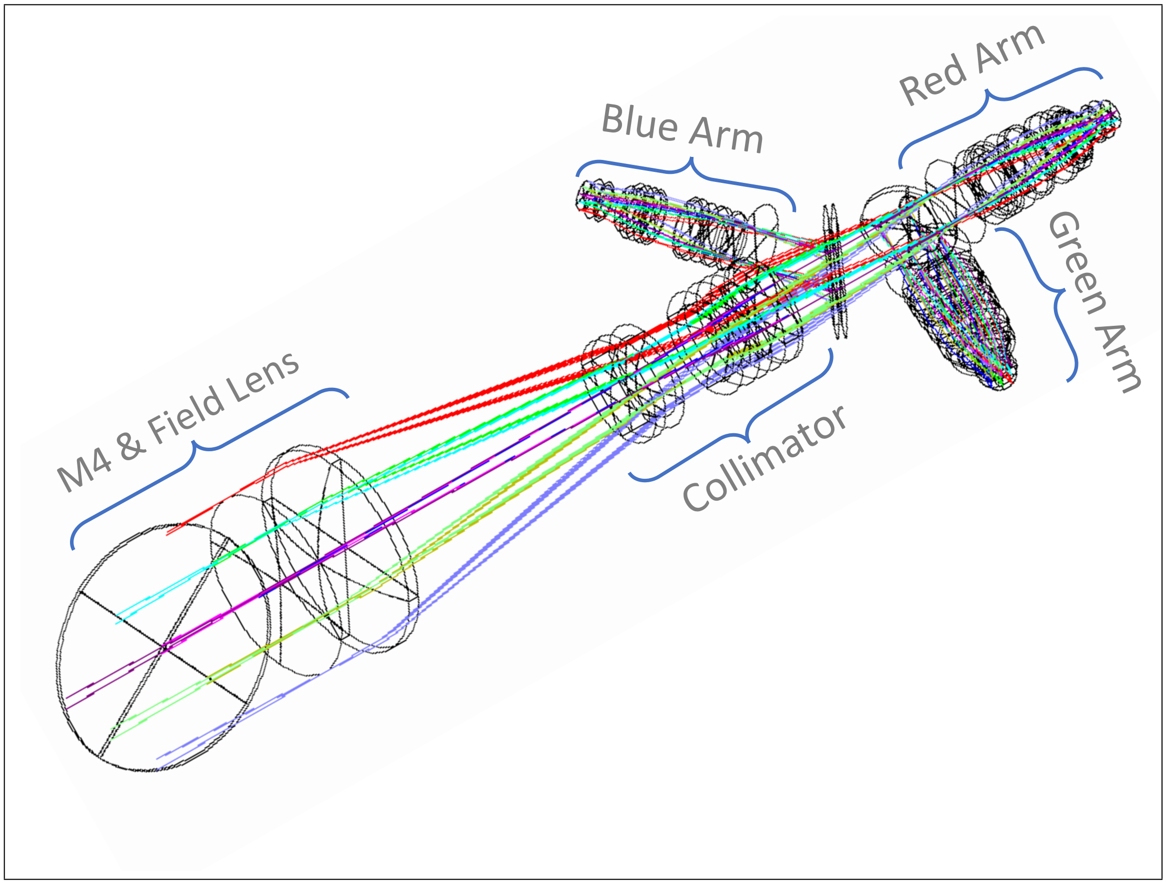

Figure A.2. Isometric view of BOMBOLO's optical design.

Table A.1. Collimator Optical Specifications for each component.

Component and surface	**Radius of Curvature [mm]**	**Thickness [mm] (to next surface)**	**Glass material (between surfaces)**	**Semi-Diameter [mm]**
FL s1	279.98	35.00	SILICA	110.00
FL s2	Infinity	350.35		110.00
CL1 s1	142.95	22.00	SILICA	56.00
CL1 s2	628.98	12.00	CAF2	56.00
CL1 s3	75.07	103.08		44.00
CL2 s1	-68.15	16.00	SILICA	42.00
CL2 s2	-200.71	25.00	CAF2	56.00
CL2 s3	-97.64	1.00		56.00
CL3 s1	-1,815.60	8.00	BAL35Y	56.00
CL3 s2	184.79	30.00	CAF2	56.00
CL3 s3	-109.04	–		56.00

Table A.2. Blue Camera Optical Specifications for each component.

Component and surface	Radius of Curvature [mm]	Thickness [mm] (to next surface)	Glass Material	Semi-Diameter [mm]
CM1 s1	-120.65	-6.00	SILICA	34.00
CM1 s2	-46.23	-22.00	CAF2	30.00
CM1 s3	76.07	-6.00	BAL35Y	30.00
CM1 s4	602.31	-3.01		34.00
CM2 s1	-68.80	-12.00	CAF2	34.00
CM2 s2	-153.44	-39.57		31.00
CM3 s1	-230.86	-10.00	CAF2	31.00
CM3 s2	230.86	-1.00		31.00
CM4 s1	-82.63	-6.00	BAL35Y	28.00
CM4 s2	-44.20	-15.22	CAF2	28.00
CM4 s3	-342.46	-30.00		25.00
CM5 s1	35.33	-6.00	SILICA	17.00
CM5 s2	Infinity	-		20.00

Table A.3. Green Camera Optical Specifications for each component.

Component and surface	**Radius of Curvature [mm]**	**Thickness [mm] (to next surface)**	**Glass Material**	**Semi-Diameter [mm]**
CM1 s1	-94.51	-6.00	BAL35Y	40.00
CM1 s2	-50.44	-33.00	CAF2	36.00
CM1 s3	75.67	-8.00	BAL35Y	36.00
CM1 s4	593.79	-3.00		40.00
CM2 s1	-66.24	-15.00	S-FPL51	38.00
CM2 s2	-104.37	-24.19		34.00
CM3 s1	-172.69	-15.00	CAF2	37.00
CM3 s2	172.69	-1.00		37.00
CM4 s1	-123.14	-6.00	BAL35Y	34.00
CM4 s2	-38.81	-20.15	S-FPL51	30.00
CM4 s3	-1,097.52	-30.00		27.00
CM5 s1	35.23	-6.00	SILICA	17.00
CM5 s2	Infinity	–		20.00

Table A.4. Red Camera Optical Specifications for each component.

Component and surface	Radius of Curvature [mm]	Thickness [mm] (to next surface)	Glass Material	Semi-Diameter [mm]
CM1 s1	89.21	6.00	BAL35Y	40.00
CM1 s2	50.83	33.00	CAF2	36.00
CM1 s3	-72.90	8.00	BAL35Y	36.00
CM1 s4	-593.79	3.00		40.00
CM2 s1	62.23	15.00	S-FPL51	38.00
CM2 s2	93.55	23.00		35.00
CM3 s1	210.64	15.00	CAF2	37.00
CM3 s2	-210.64	1.00		37.00
CM4 s1	93.93	6.00	BAL35Y	34.00
CM4 s2	45.44	15.70	CAF2	28.00
CM4 s3	Infinity	30.00		26.00
CM5 s1	-33.66	6.00	SILICA	17.00
CM5 s2	Infinity	–		20.00

B. SECOND APPENDIX: BOMBOLO - FIELD ROTATION MONTE CARLO SIMUALTION CODE

Listing 1. Field Rotation Monte-Carlo simulation code

```

clear
clc
close all

%% Change of Gravity Vector and quantification of the Field Rotation
%  This code is a sort of MonteCarlo simulation to characterize the change
%  of the gravity vector and the field rotation for the instrument BOMBOLO.
%  The code use a 4-quadrant coordinate system transformation from
%  equatorial to horizontal (alt-az) and viceversa. Also considers that the
%  images taken by the instrument has always the celestial North-pole in
%  the vertical axis of the CCD's.
%  In this simulation we consider the Right Ascension Angle and Hour Angle
%  as equivalent, because they have a linear relation.

%% STAGE I
%  This are the starting points for the simulation, and the exposure times
%  that defines change in the hour angle
alt_0 = [40:20:80];
az_0  = [-6:3:6]*10;
expTime = [1:6]/6; % 10 min to 1 horas
lat = -(30+14/60+26.6/3600); % Cerro Pachon Latitude 30deg 14m 26.6s

```

```
m = length(alt_0);
n = length(az_0);
p = length(expTime);
v_rot=360/(23+59/60+ 4.0909/3600); % Rotation velocity of earth in deg/hour

%% STAGE II
%  Measure of the field rotation offset
%  We want to the images to have the celestial north always upwards in the
%  images. In order to achieve this, we can consider the exposure always
%  starting with te hour angle 0. Then we can calculate the amount of field
%  rotation from here to the starting point selected from STAGE I, but as
%  if the Earth was rotating contrary to the direction of regular rotation.
%  With this, we can calculate the Field offset needed so when the
%  telescope is actually crossing hour angle 0, the image will have north
%  upwards.

fila = 1; % Auxiliar counter variable for saving the data
data = zeros(m*n*p,10); % The data to save (explained later)


for i = 1:m % i for altitud
    for j = 1:n % j for azimuth

        % First, we choose a starting poing and we got his 'RA-DEC'
        % equivalent positions in the sky. In this case, for simplicity we
        % consider the Hour Angle equivalent to the Right Ascension because
```

```
        % of his linear relationship
        [dec_0,H_0]=alt2eq(alt_0(i),az_0(j),lat);
        dH = abs((H_0-0)/1000);
        % We also calculate the exposure time (or rotational time) needed
        % from the 0 hour angle to, so we can integrate the field rotation
        % later
        expTime_0 = abs(H_0/v_rot);
        dt0 = expTime_0/1000;

        % With this we now generate the space of hour angles, in order to
        % "sample" the trajectory in alt-az coordinates. First, we need the
        % hour angle samples

        if(H_0<0)
            H_sp0 = [H_0:dH:0];
            do_rot = 1;
        elseif (H_0>0)
            H_sp0 = [0:dH:H_0];
            do_rot = 1;
        else
            H_sp0 = 0;
            do_rot = 0;
        end

        % The transformation of coordinate functions demand that the
        % vector inputs needs the same length

        dec_0 = ones(size(H_sp0))*dec_0(1);


        % Now, we proceed to calculate the field rotation offset
```

```
        [alt_v,az_v] = eq2alt(dec_0,H_sp0,lat);
        if do_rot==1
            FR0 = fldrot(alt_v,az_v,lat); % deg/hr
            rot_0 = dt0*sum(FR0(:));
        else
            rot_0=0;
        end

        %% STAGE III
        % Now that we have all the field rotation offset, we procced to
        % measure the field rotation given by the earth rotation during the
        % exposure time

        for k = 1:p
            % We calculate the final hour angle from a starting point using
            % the exposure time. Then, as in the previous stage, we need to
            % "sample" the trajectory that the telescope follows in the sky
            % in alt-az coordinates.

            H2 = H_0 + expTime(k)*v_rot;
            dH2=(H2-H_0)/1000;
            H_v=[H_0:dH2:H2];
            % We turn dec_0 in a vector with the lenght of H_v
            dec_1 = ones(size(H_v))*dec_0(1);

            % We turn all this points to the alt-az system
            [alt_v2,az_v2] = eq2alt(dec_1,H_v,lat);

            % The field rotation is calculated and integrated to measure
```

```
        % the whole rotation
        FR1 = fldrot(alt_v2,az_v2,lat); % deg/hr
        dt=expTime(k)/length(FR1(:));
        t=0:dt:expTime(k);
        % La integral es rot = Suma ( FR1_i * dt_i) = dt*Suma(FR1_i)
        rot_2 = dt*sum(FR1(:));

        % Now the total rotation is
        rot = rot_2-rot_0;

        %% STAGE IV
        % Now we need to store the information of interest.
        % 1. When at least one of the points in the trajectory returns
        %    a altitud angle below a minimun, the data is not
        %    considered as valid. In case you think that this make the
        %    lost of data, you are wrong. The valid points for this
        %    cases are considered in othe exposure times.
        % 2. We need a way to characterize the changes of gravity as
        %    seen from the instrument. For this, two angles play the
        %    important roles: The delta in altitud, ant the delta in
        %    field rotation.
        % 3. We need just the altitud and the field rotation, but in
        %    order to identify the relevant cases, we will save the
        %    next data:
        %    - Starting point (alt-az)
        %    - Final Point (alt-az)
```

```
                %    — Exposure Time
                %    — Absolute Difference of altitud
                %    — Field Rotation Offset
                %    — Field Rotation Final
                %    — Field rotation difference

                alt_thres = 30;
                alt_neg = sum((alt_v<=alt_thres));

                if (alt_neg==0)
                    data(fila,:)=[alt_0(i),az_0(j),...
                        alt_v2(length(alt_v2)),az_v2(length(az_v2)), ...
                        expTime(k),...
                        rot_0, rot_2,...
                        rot,...
                        (alt_v2(length(alt_v2))—alt_0(i)),...
                        1];
                    data(fila,10)=abs(data(fila,9)*data(fila,7));
                    fila=fila+1;
                end
            end
        end
    end
```

Listing 2. Altitude to Equatorial change of coordinate system code.

```
function [dec, H] = alt2eq(alt, Az, lat)
% Esta funcion retorna los angulos de declinacion (dec:= elevacion
    desde el
% horizonte ecuatorial) y el angulo de Hora (H:= angulo equivalente
    a la
% ascension recta H = Local Sideral Time — RA)
% Funcion basada en las ecuaciones de wikipedia.
% alt y Az deben ser elementos del mismo largo
```

```

% Recomendaciones:
% - An equation which finds the sine, followed by the arcsin function,
%   is recommended when calculating latitude/declination/altitude.
% - Use of an equation which finds the tangent, followed by the second
%   arctangent function (ATN2 or ATAN2), is recommended when calculating
%   longitude/right ascension/azimuth.

% sin(dec) = sin(lat)*sin(alt) - cos(lat)*cos(alt)*cos(Az)
% cos(dec)*sin(H) = cos(alt)*sin(Az)
% cos(dec)*cos(H) = sin(a)*cos(lat)+cos(alt)*cos(Az)4*sin(lat)

% Obs: Para el caso de la funcion asin(dec) si funciona porque dec cubre
% una ventana maxima de 180deg en la esfera completa.

alt = alt*pi/180;
Az  = Az*pi/180;
lat = lat*pi/180;

sin_dec = sin(lat)*sin(alt) - cos(lat)*cos(alt).*cos(Az);
dec = asin(sin_dec);
cos_dec = cos(dec);

Y = cos(alt).*sin(Az)/cos_dec;
X = (sin(alt).*cos(lat)+cos(alt).*cos(Az).*sin(lat))./cos_dec;

H = atan2(Y,X)*180/pi;
dec = dec*180/pi;
```

Listing 3. Equatorial to Altitude change of coordinate system code.

```
function [alt, Az] = eq2alt(dec, H, lat)
% Esta funcion retorna los angulos de altitud (alt:= elevacion desde el
% horizonte terrestre) y el angulo de azimut (Az:= angulo entre el sur
% celeste, ascendiendo hacia el oeste).
% Funcion basada en las ecuaciones de wikipedia.
% dec y H deben ser elementos del mismo largo

% Recomendaciones:
% - An equation which finds the sine, followed by the arcsin function,
%   is recommended when calculating latitude/declination/altitude.
% - Use of an equation which finds the tangent, followed by the second
%   arctangent function (ATN2 or ATAN2), is recommended when calculating
%   longitude/right ascension/azimuth.

% sin(alt) = sin(lat)*sin(dec)+cos(lat)*cos(dec)*cos(H)
% cos(alt)*sin(Az) = cos(dec)*sin(H)
% cos(alt)*cos(Az) = cos(dec)*cos(H)*sin(lat)-sin(dec)*cos(lat);

% Obs: Para el caso de la funcion asin(alt) si funciona porque alt cubre
% una ventana maxima de 180deg en la esfera completa.

dec = dec*pi/180;
H   = H*pi/180;
lat = lat*pi/180;

sin_alt = sin(lat)*sin(dec)+cos(lat)*cos(dec).*cos(H);
alt = asin(sin_alt);
```

```
cos_alt = cos(alt);

Y = cos(dec).*sin(H)/cos_alt;
X = (sin(lat)*cos(dec).*cos(H)-cos(lat)*sin(dec))./cos_alt;

Az = atan2(Y,X)*180/pi;
alt = alt*180/pi;
```

Listing 4. Field Rotation rate code

```
function FR = fldrot(alt,az,lat)
% Valor de la rotacion de campo para un field de-rotator en funcion
    de las
% coordenadas alt-az en grados/hora

% lat = (30+14/60+26.6/60)*pi/180; % Cerro Pachon Latitude 30deg 14'
     26.6''

SD = 23+59/60+ 4.0909/3600; % Duracion dia sideral en horas
K = 360/SD * cos(lat*pi/180); % Constante del observador deg/hora
FR = K * cos(az*pi/180)./cos(alt*pi/180); % Tasa de rotacion de
    campo [deg/hour]

end
```

C. THIRD APPENDIX: BOMBOLO - COMPONENT WEIGHT TABLES

Table C.1. Table of weights for the collimator.

	Collimator		
Type	**Component**	**Component Weight**	**System Weight**
Optics	FL	1940 gr	1940 gr
	CL1	1023 gr	3111 gr
	CL2	1128 gr	
	CL3	960 gr	
	Dichroic #1	300 gr	500 gr
	Dichroic #2	200 gr	
Mechanics	Barrel	4530 gr	8530 gr
	Supports	4000 gr	

Table C.2. Table of weights for the three arm cameras.

		Blue Arm		Green Arm		Red Arm	
Type	**Component**	**Component and System Weight**					
Optics	**CM1**	314 gr	672 gr	643 gr	1270 gr	648 gr	1227 gr
	CM2	108 gr		226 gr		210 gr	
	CM3	78 gr		132 gr		152 gr	
	CM4	147 gr		244 gr		192 gr	
	CM5	25 gr		25 gr		25 gr	
Mechanics	**Barrel**	850 gr	5850 gr	1080 gr	6080 gr	1070 gr	6070 gr
	Supports	5000 gr		5000 gr		5000 gr	
Electronics	**Camera**	7000 gr	7000 gr	7000 gr	7000 gr	7000 gr	7000 gr

Table C.3. Table of weights for the three filter wheels.

		Filter Wheel	
Type	**Component**	**Quantity**	**System Weight**
Optics	**Blue Filters**	3	120 gr
	Green Filters	4	160 gr
	Red Filters	5	200 gr
Mechanics	**Wheel**	3	900 gr
	Supports	3	3000 gr
Electronics	**Smart Motor**	4	5200 gr

Table C.4. Table of weights for the other components.

Other Components and Systems	
Component	**Component /System Weight**
Screws, fasteners, washers, and similars	15000 gr
Plastic Covers	8000 gr
Cables, wraps and connectors	5000 gr

D. FOURTH APPENDIX: BOMBOLO - SIMPLIFIED BLUE PRINT OF THE MECHANICAL STRUCTURE

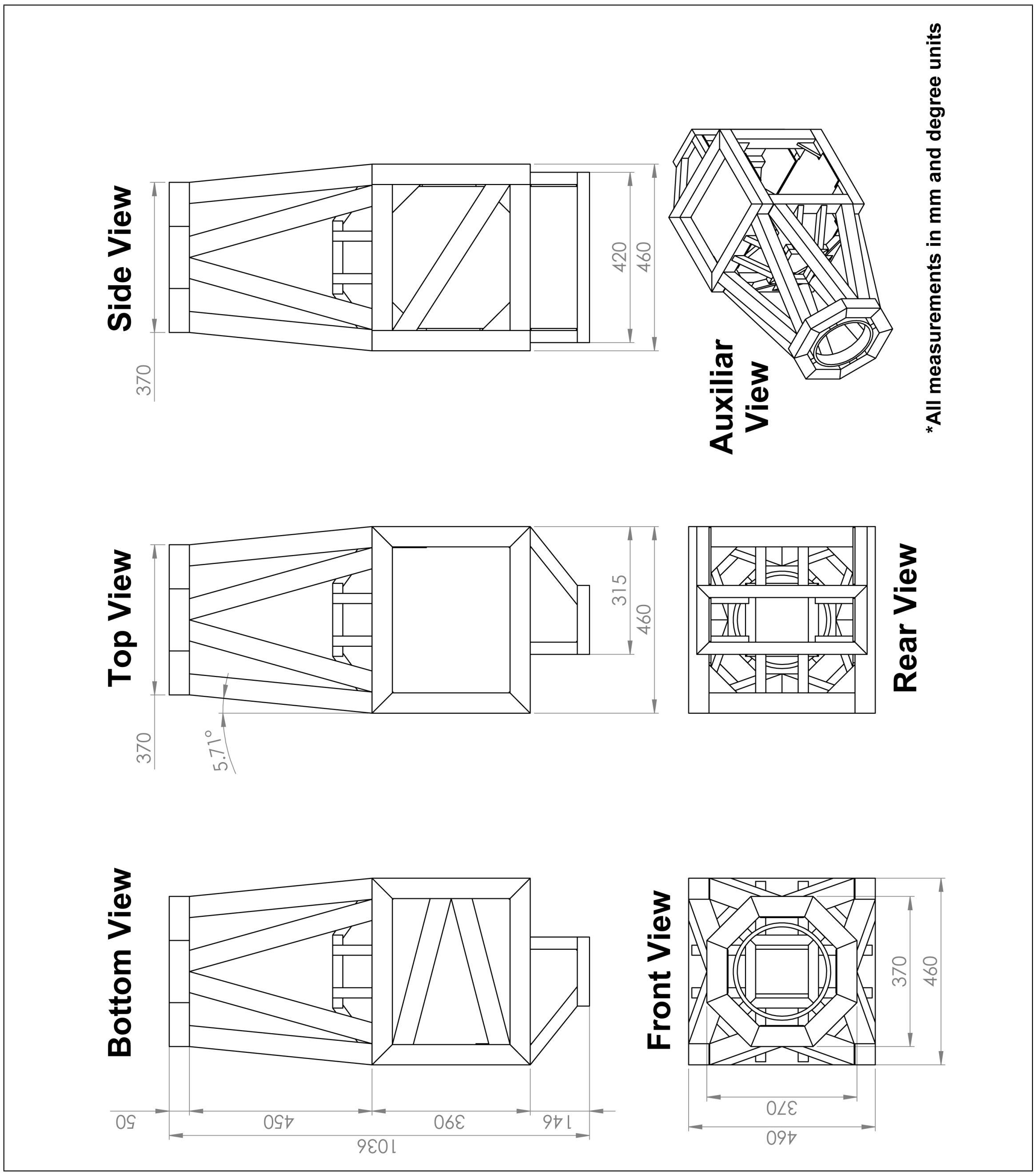

Figure D.1. Simplified Blue Print of the Structure

E. FIFTH APPENDIX: BOMBOLO - FEA DISPLACEMENTS

Table E.1. BOMBOLO's Finite Element Analysis Displacements for the collimator optical system.

Surface	DispX (um)	DispY (um)	DispZ (um)	DispTot (um)	Tip (deg)	Tilt (deg)
CL0 s1	0.000	0.000	0.000	0.000	0.000	0.000
CL0 s2	-6.516	-7.546	0.009	9.970	0.236	1.248
CL1 s1	-12.635	-10.032	0.353	16.137	0.825	1.361
CL1 s2	-13.041	-10.283	0.391	16.612	0.862	1.368
CL1 s3	-13.262	-10.425	0.412	16.874	0.883	1.372
CL2 s1	-15.238	-11.806	0.624	19.286	1.061	1.406
CL2 s2	-15.542	-12.038	0.660	19.670	1.088	1.411
CL2 s3	-16.021	-12.414	0.719	20.281	1.131	1.419
CL3 s1	-16.040	-12.429	0.721	20.305	1.132	1.420
CL3 s2	-16.194	-12.552	0.740	20.503	1.146	1.422
CL3 s3	-16.773	-13.028	0.815	21.254	1.197	1.432
Dich1 s1	-18.141	-14.218	1.002	23.070	1.316	1.455
Dich1 s2	-18.333	-14.393	1.030	23.331	1.333	1.458
Dich2 s1	-20.078	-16.061	1.295	25.744	1.481	1.486
Dich2 s2	-20.275	-16.258	1.327	26.022	1.498	1.489

Table E.2. BOMBOLO's Finite Element Analysis Displacements for the blue arm optical system.

Surface	DispX (um)	DispY (um)	DispZ (um)	DispTot (um)	Tip (deg)	Tilt (deg)
BCM1 s1	2.926	-13.578	-17.596	22.418	-0.878	1.323
BCM1 s2	2.820	-13.510	-17.541	22.320	-0.792	1.268
BCM1 s3	2.473	-13.321	-17.372	22.031	-0.475	1.065
BCM1 s4	2.388	-13.287	-17.335	21.971	-0.389	1.010
BCM2 s1	2.348	-13.271	-17.318	21.944	-0.346	0.982
BCM2 s2	2.198	-13.229	-17.260	21.857	-0.173	0.872
BCM3 s1	1.826	-13.290	-17.180	21.797	0.400	0.504
BCM3 s2	1.764	-13.355	-17.188	21.838	0.544	0.412
BCM4 s1	1.759	-13.362	-17.190	21.843	0.558	0.403
BCM4 s2	1.729	-13.411	-17.200	21.878	0.645	0.347
BCM4 s3	1.674	-13.558	-17.241	21.997	0.853	0.214
BCM5 s1	1.643	-13.991	-17.399	22.387	1.284	-0.063
BCM5 s2	1.650	-14.099	-17.442	22.489	1.371	-0.118
CCD	1.678	-14.335	-17.541	22.716	1.543	-0.229

Table E.3. BOMBOLO's Finite Element Analysis Displacements for the green arm optical system.

Surface	DispX (um)	DispY (um)	DispZ (um)	DispTot (um)	Tip (deg)	Tilt (deg)
GCM1 s1	8.058	-16.038	18.524	25.794	0.842	0.440
GCM1 s2	8.015	-16.102	18.613	25.883	0.716	0.633
GCM1 s3	7.495	-16.266	18.978	26.095	0.023	1.690
GCM1 s4	7.299	-16.260	19.035	26.077	-0.145	1.946
GCM2 s1	7.218	-16.252	19.054	26.063	-0.208	2.042
GCM2 s2	6.754	-16.179	19.121	25.942	-0.523	2.523
GCM3 s1	5.647	-15.876	19.135	25.497	-1.102	3.404
GCM3 s2	4.907	-15.620	19.083	25.144	-1.417	3.883
GCM4 s1	4.854	-15.600	19.078	25.118	-1.438	3.915
GCM4 s2	4.528	-15.479	19.045	24.956	-1.564	4.107
GCM4 s3	3.590	-15.107	18.922	24.477	-1.897	4.613
GCM5 s1	1.518	-14.209	18.563	23.426	-2.525	5.567
GCM5 s2	1.057	-13.999	18.471	23.200	-2.651	5.758
CCD	0.088	-13.548	18.266	22.742	-2.903	6.138

Table E.4. BOMBOLO's Finite Element Analysis Displacements for the red arm optical system.

Surface	DispX (um)	DispY (um)	DispZ (um)	DispTot (um)	Tip (deg)	Tilt (deg)
RCM1 s1	-21.901	-17.953	1.598	28.364	1.634	1.515
RCM1 s2	-22.024	-18.086	1.620	28.545	1.644	1.517
RCM1 s3	-22.704	-18.833	1.740	29.550	1.700	1.528
RCM1 s4	-22.869	-19.018	1.771	29.796	1.714	1.531
RCM2 s1	-22.931	-19.088	1.781	29.889	1.719	1.532
RCM2 s2	-23.243	-19.439	1.838	30.356	1.744	1.536
RCM3 s1	-23.810	-20.089	1.943	31.213	1.790	1.545
RCM3 s2	-24.123	-20.455	2.002	31.692	1.816	1.550
RCM4 s1	-24.144	-20.479	2.007	31.724	1.818	1.550
RCM4 s2	-24.271	-20.627	2.030	31.917	1.828	1.552
RCM4 s3	-24.587	-21.003	2.091	32.404	1.853	1.557
RCM5 s1	-25.221	-21.765	2.215	33.388	1.904	1.567
RCM5 s2	-25.349	-21.920	2.240	33.587	1.914	1.569
CCD	-25.604	-22.233	2.291	33.987	1.935	1.573

F. SIXTH APPENDIX: BOMBOLO - FEA DIFFERENTIAL DISPLACEMENTS

F.1. FEA Results for the Azimuth case

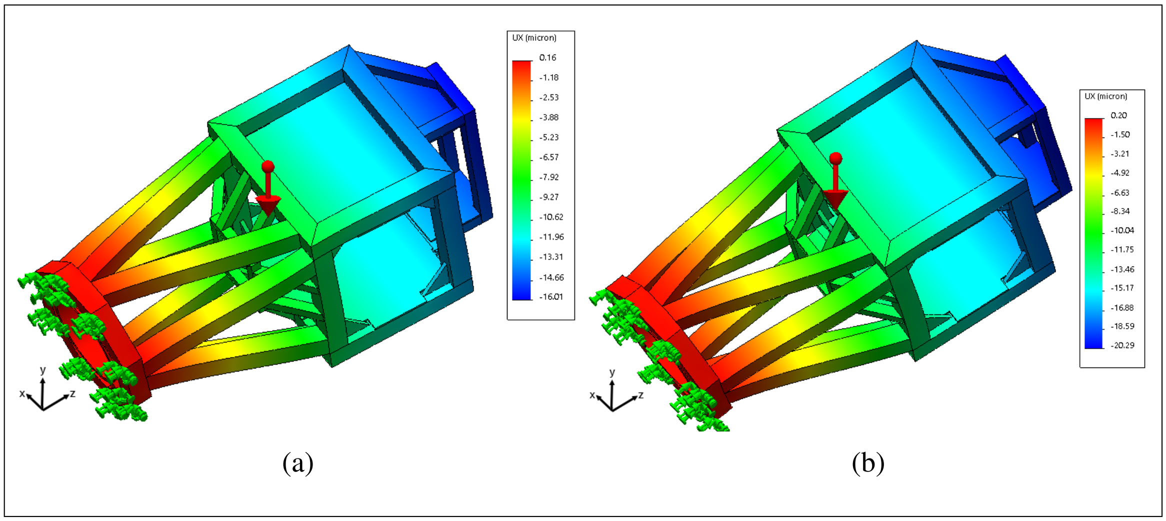

Figure F.1. FEA Differential Displacement in X for the azimuth case. (a) FEA Static for the starting point in X. (b) FEA Static for the ending point in X.

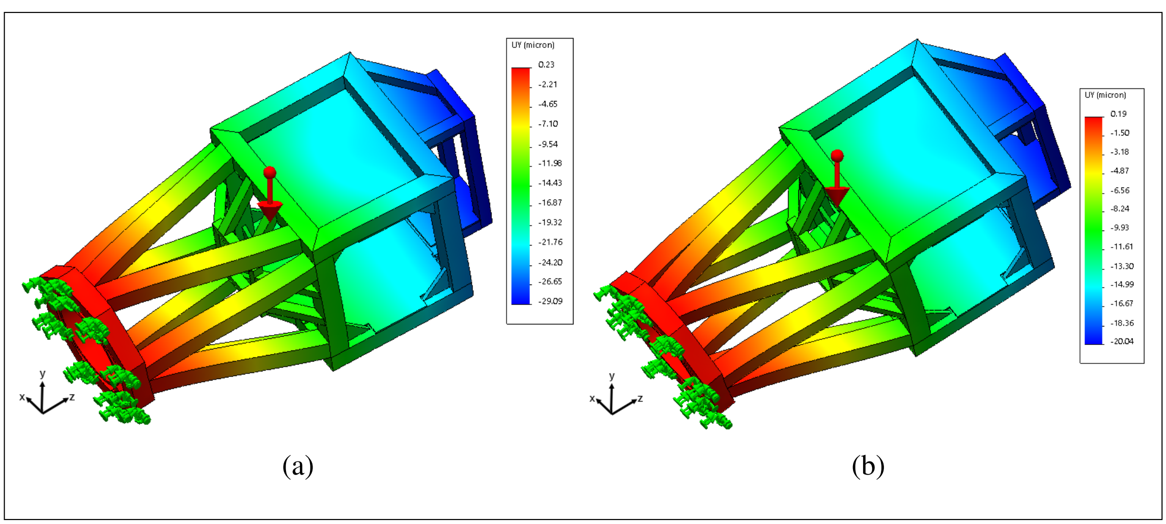

Figure F.2. FEA Differential Displacement in Y for the azimuth case. (a) FEA Static for the starting point in Y. (b) FEA Static for the ending point in Y.

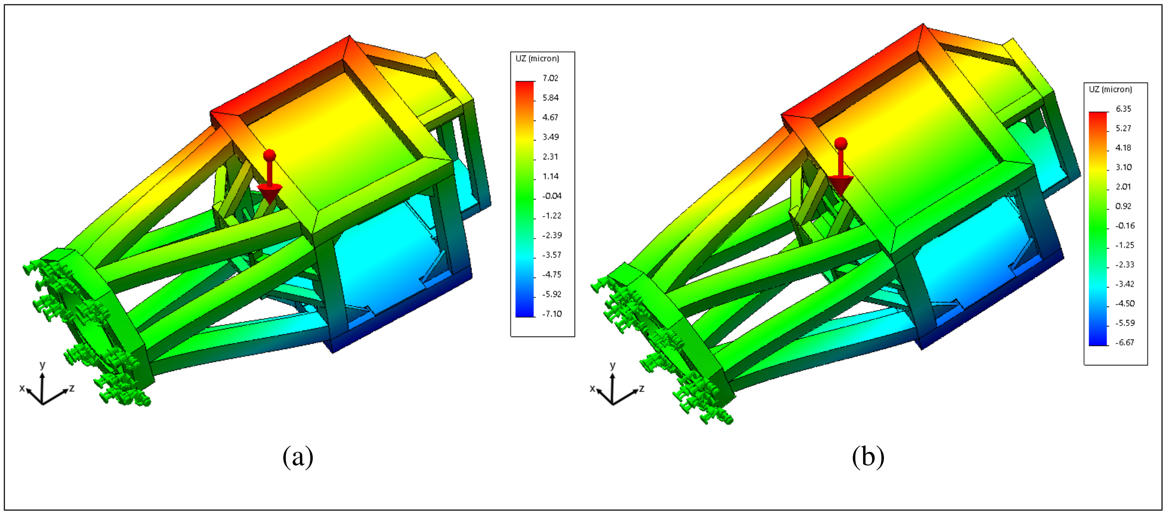

Figure F.3. FEA Differential Displacement in Z for the azimuth case. (a) FEA Static for the starting point in Z. (b) FEA Static for the ending point in Z.

F.2. FEA Results for the Altitude case

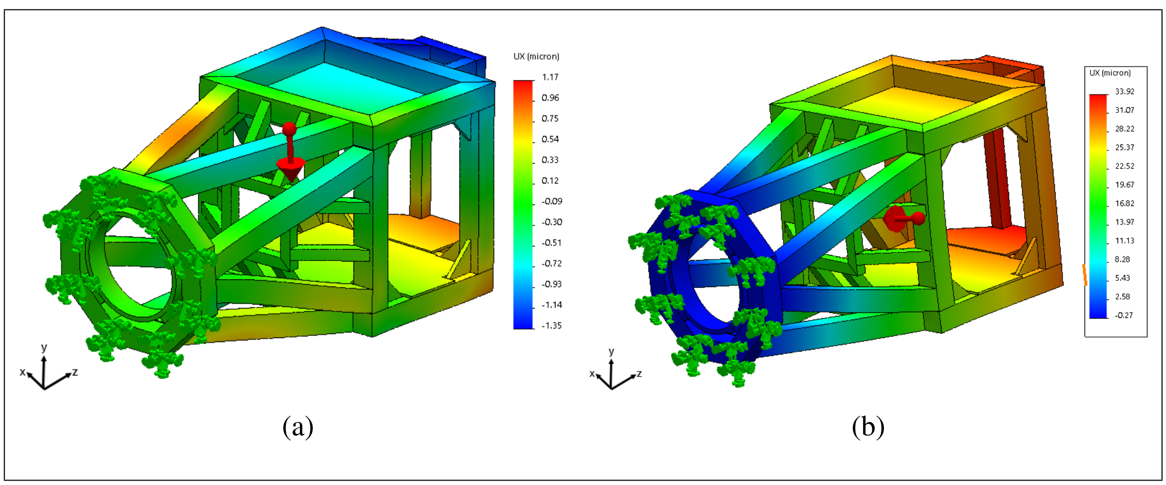

Figure F.4. FEA Differential Displacement in X for the Altitude case. (a) FEA Static for the starting point in X. (b) FEA Static for the ending point in X.

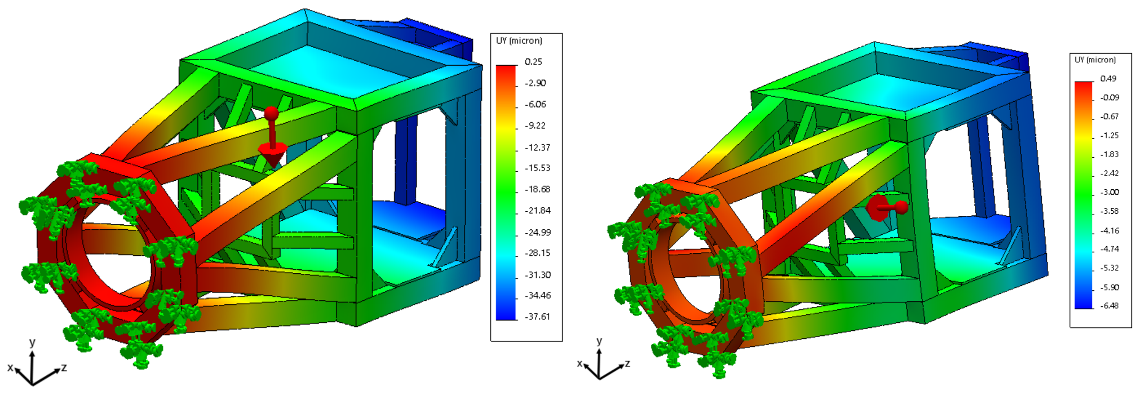

(a) (b)

Figure F.5. FEA Differential Displacement in Y for the Altitude case. (a) FEA Static for the starting point in Y. (b) FEA Static for the ending point in Y.

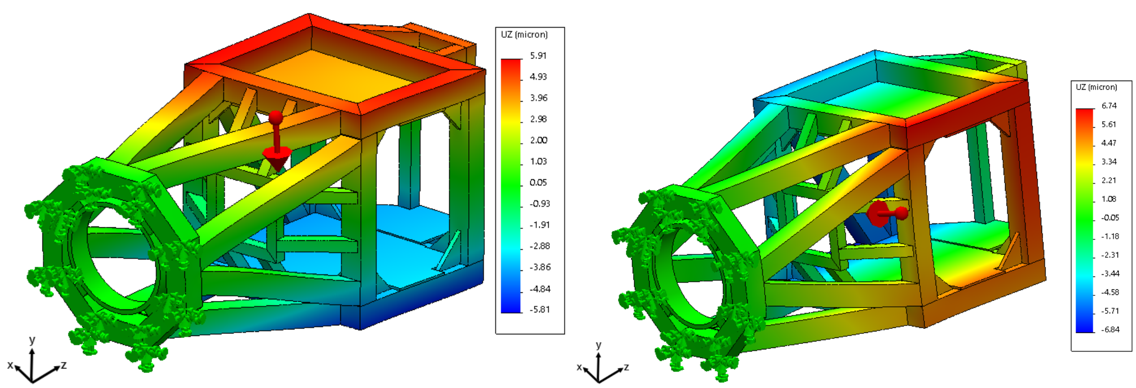

(a) (b)

Figure F.6. FEA Differential Displacement in Z for the Altitude case. (a) FEA Static for the starting point in Z. (b) FEA Static for the ending point in Z.